National Aeronautics and
Space Administration

HLS-UG-001

BASELINE RELEASE

EFFECTIVE DATE: JANUARY 04, 2021

HUMAN LANDING SYSTEM

LUNAR THERMAL ANALYSIS GUIDEBOOK

Publicly Available: Release to Public Websites Requires Approval of Chief, Office of Primary Responsibility, and approval via the Scientific and Technical Information (STI) process, if applicable

REVISION AND HISTORY PAGE

Revision No.	Change No.	Description	Effective Date
-	HLS-C0064	Baseline Release (Reference HCB.07.01.2020)	01/04/2021

TABLE OF CONTENTS

SECTION **PAGE**

1.0 INTRODUCTION 10
1.1 PURPOSE 10
1.2 SCOPE 10
1.3 CHANGE AUTHORITY/RESPONSIBILITY 10
2.0 DOCUMENTS 10
2.1 APPLICABLE DOCUMENTS 10
3.0 THE EARTH'S MOON 11
3.1 PHYSICAL CHARACTERISTICS 12
3.2 ORBIT 13
4.0 LUNAR SPACE THERMAL ENVIRONMENTS 16
4.1 SOLAR CONSTANT 16
4.2 ALBEDO 16
4.3 LUNAR LONG-WAVE RADIANCE 16
4.3.1 Analytical Expressions 16
4.3.2 Latitude/Longitude Tables of Lunar Surface Flux and/or Temperature 18
4.4 SOLAR ECLIPSE DURATIONS 20
4.4.1 Low Lunar Orbit 20
4.4.2 Near-Rectilinear Halo Orbit 21
5.0 LUNAR SURFACE THERMAL ENVIRONMENTS 21
5.1 SURFACE FEATURES 21
5.1.1 Crater Size Distribution/Topography 22
5.1.2 Boulders/Rocks 22
5.1.3 LRO Diviner Digital Surface Data 23
5.2 SURFACE TEMPERATURE 23
5.2.1 LRO Diviner Digital Temperature Data Maps 23
5.2.2 Analytical Expressions (Steady State Approximation) 25
5.3 SUBSURFACE TEMPERATURE 26
5.3.1 Apollo and Derived LRO Measurements 27
5.4 GROUND HEAT FLOW 28
6.0 THERMO-PHYSICAL PROPERTIES OF LUNAR REGOLITH 29

6.1 BULK THERMAL CONDUCTIVITY 29
6.2 SPECIFIC HEAT 32
6.3 BULK DENSITY 32
6.4 THERMAL DIFFUSIVITY 33
7.0 OPTICAL PROPERTIES OF LUNAR REGOLITH 36
7.1 SOLAR ABSORPTIVITY/ALBEDO 37
7.2 INFRARED EMITTANCE 43
7.3 LIGHT SCATTER/SPECULARITY OF LUNAR REGOLITH 43
8.0 LUNAR ORBIT MODELING GUIDELINES/APPROACHES 44
8.1 NEAR RECTILINEAR HALO ORBIT (NRHO) 44
8.1.1 Description 44
8.1.2 Modeling Approach 45
8.2 LOW LUNAR ORBIT (LLO) 47
8.2.1 Description 47
8.2.2 Modeling Approach 47
8.3 DESCENT/ASCENT 48
8.3.1 Description 48
8.3.2 Modeling Approach 48
9.0 LUNAR SURFACE MODELING GUIDELINES/APPROACHES 55
9.1 MODELING THE GROUND-PLANE SOLAR ENVIRONMENT 56
9.1.1 Traditional Orbit Definition 58
9.1.2 Orbit Vector List 59
9.1.3 Solar Elevation Angle 64
9.2 SUBSURFACE MODELING 68
9.2.1 Approach 68
9.2.2 Boundary Conditions 69
9.2.3 Discretization 70
9.2.4 Initial Conditions Cyclic Steady State 70
9.3 SELECTING TERRAIN SIZE 74
9.3.1 Sizing Ground Plane 74
9.3.2 Shadowing by Terrain Features 85
9.4 SIMPLIFIED TERRAIN MODELING 88
9.4.1 Far Field Boundary Conditions and Lunar Curvature 88

9.4.2 Simplified Flat Plane Comparison to DSNE 89
9.4.3 Far Field Terrain Modeling 93
9.5 DETAILED TERRAIN MODELING 95
9.5.1 Accessing, importing and utilizing LRO digital Lunar Surface Data 95
9.6 MODELING EXAMPLE 104
9.6.1 Comparison to LRO Diviner Temperature Data 104
10.0 ACCOUNTING FOR LUNAR DUST IMPACTS 105
11.0 SPECIAL CONSIDERATIONS FOR PSRS 109
11.1 EARTH SHINE 109
11.2 LUNAR SURFACE TEMPERATURE FOR COLD CASE ANALYSIS 112
12.0 REFERENCES 112
APPENDIX A ACRONYMS AND ABBREVIATIONS AND GLOSSARY OF TERMS 118
APPENDIX B OPEN WORK 122
APPENDIX C EXAMPLE MODELS/CASE STUDIES 123
APPENDIX D DERIVATIONS 124
APPENDIX E ASCENT/DESCENT ATTITUDE COMPUTER CODE 125
APPENDIX F OTHER COMPUTER CODE 129
APPENDIX G LIGHT SCATTERING OF LUNAR REGOLITH 142

APPENDIXES

APPENDIX A ACRONYMS AND ABBREVIATIONS AND GLOSSARY OF TERMS 118
APPENDIX B OPEN WORK 122
APPENDIX C EXAMPLE MODELS/CASE STUDIES 123
APPENDIX D DERIVATIONS 124
APPENDIX E ASCENT/DESCENT ATTITUDE COMPUTER CODE 125
APPENDIX F OTHER COMPUTER CODE 129
APPENDIX G LIGHT SCATTERING OF LUNAR REGOLITH 142

LIST OF TABLES

TABLE 3.1-1: AVERAGE CHEMICAL COMPOSITION OF LUNAR SURFACE REGOLITH [1] 13

TABLE 3.2-1: LUNAR ORBIT PARAMETERS [1] 14

TABLE 4.3.1-1 LUNAR LONG-WAVE RADIANCE ALBEDO AND EMISSIVITY EQUATION INPUTS 18

TABLE 4.3.2-1 HOT CASE LUNAR RADIANCE, COMBINED VALUES 19

TABLE 4.4.2.2-1 DURATION IN LUNAR SHADOW FOR GATEWAY NRHO 21

TABLE 6.1-1: WATSON'S EQUATION FOR RETURNED APOLLO SAMPLES 30

TABLE 6.1-2: COEFFICIENTS FOR BULK K OF CRUSHED BASALT 31

TABLE 7.1-1 APOLLO DIRECTIONAL REFLECTANCE 40

TABLE 8.1.2.2-1: ORBITAL PARAMETERS FOR KEPLERIAN NRHO APPROXIMATION WITH BOUNDING ENVIRONMENTS 47

TABLE 9.2.4-1 DEPTH VS. DENSITIES IN EXAMPLE MODEL 71

TABLE 9.2.4-2 COMPARISON OF MAXIMUM AND MINIMUM SURFACE AND SUBSURFACE TEMPERATURES FOR A 1 M^2 SECTION AT -85.393N LATITUDE UP TO 100 YEARS FOR CASE 2. 73

TABLE 9.3.2-1: ESTIMATED SHADOWING FROM SURFACE FEATURES AT POINT PH ON TO POINT P. 87

TABLE A1-1 ACRONYMS AND ABBREVIATIONS 118

TABLE B1-1 TO BE DETERMINED ITEMS 122

TABLE B2-1 FORWARD WORK ITEMS 122

LIST OF FIGURES

FIGURE 3.0-1: LUNAR SURFACE TEMPERATURES 11

FIGURE 3.1-1: NEAR AND FAR SIDES OF THE MOON 12

FIGURE 3.2-2: LUNAR ORBITAL PERIOD..... 14

FIGURE 3.2-3: SEASONAL VARIATION ON THE MOON..... 15

FIGURE 3.2-4: DIVINER MAXIMUM BOLOMETRIC TEMPERATURES OF THE SOUTH POLE (85°-90°S) SPLIT INTO SEASONS..... 15

FIGURE 4.3.2-1: COORDINATING SUBSOLAR POINTS FOR SOLAR AND PLANETSHINE USING A PLANETARY COODINATE SYSTEM..... 19

FIGURE 5.2.2-2: LUNAR SURFACE TEMPERATURES FROM APOLLO 17 MEASUREMENTS COMPARED TO THOSE CALCULATED WITH THE STEADY STATE APPROXIMATION (USING 100K AT NIGHT). 26

FIGURE 5.3.1-1: LUNAR SUBSURFACE TEMPERATURES (LEFT) AND MAXIMUM MONTHLY CHANGES IN TEMPERATURE VS DEPTH (RIGHT) FROM LANGSETH'S "IN-SITU MEASUREMENTS OF LUNAR HEAT FLOW"..... 27

FIGURE 6.4-1: THERMAL DIFFUSIVITY OF LUNAR REGOLITH..... 34

FIGURE 6.4-2: THERMAL DIFFUSIVITY OF LUNAR REGOLITH VERSUS DEPTH AND TEMPERATURE 35

FIGURE 7.0-2: SOLAR, LUNAR AND THERMAL RADIATOR IRRADIANCE 37

FIGURE 7.1-1: ALBEDO DEFINITIONS..... 38

FIGURE 7.1-2: SCHEMATIC OF INTEGRATING SPHERE FOR APOLLO MEASUREMENTS 39

FIGURE 7.1-3: REFLECTIVITY OF APOLLO SAMPLES..... 40

FIGURE 7.1-4: LUNAR SOLAR ABSORPTANCE VERSUS LATITUDE FROM APOLLO MEASUREMENTS 41

FIGURE 7.1-5: DIRECTIONAL ALBEDO FITS FROM VARIOUS LUNAR SURFACE MODELS 42

FIGURE 7.1-6: LUNAR SOLAR ABSORPTANCE VERSUS INCIDENCE ANGLE FROM LUNAR SURFACE MODELS 43

FIGURE 8.1.2.2-1: COMPARISON OF NRHO AND KEPLERIAN PERILUNE TRUE ANOMALY..... 46

FIGURE 8.1.2.2-2: COMPARISON OF NRHO AND KEPLERIAN ORBITAL RADII NEAR MOON 46

FIGURE 8.3.2-1: IMAGE OF THERMAL DESKTOP ORBIT INTERFACE..... 50

FIGURE 8.3.2-2: IMAGES OF LANDER ORIENTATION DURING DESCENT..... 50

FIGURE 8.3.2-3: DEPICTION OF HOW THE X-AXIS ROTATION CAN BE DETERMINED..... 51

FIGURE 8.3.2-4: TRAJECTORY OF LANDER WITH THE Z-AXIS FACING THE VELOCITY VECTOR AND THE X-AXIS POINTING AWAY FROM THE CENTER OF THE PLANET. 52

FIGURE 8.3.2-5: EXPRESSION FOR 2-ARGUMENT ARCTANGENT IN TERMS OF STANDARD ARCTANGENT FUNCTION. 53

FIGURE 8.3.2-6: EXAMPLE OF OF SYMBOL ARRAY IN THERMAL DESKTOP 54

FIGURE 8.3.2-7: IMAGES OF THERMAL DESKTOP ORBIT INTERFACE SHOWING 54

FIGURE 8.3.2-8: IMAGE OF FINAL LANDER ORIENTATION DURING DESCENT. 55

FIGURE 9.1-1: CONTROL TAB IN CASE SET MANAGER>CASE> RADIATION TASKS> RADIATION ANALYSIS DATA DIALOG BOX. 57

FIGURE 9.1.1-1: HEATING RATE CASE MANAGER > TERRESTRIAL > LAT/LONG INPUT TAB 58

FIGURE 9.1.2-1: HEATING RATE CASE MANAGER > TRAJECTORY > VECTOR INPUT TAB 59

FIGURE 9.1.2-2: DIURNAL LUNAR SURFACE TEMPERATURES AT 0E AND 85N FOR DIFFERENT SOLAR DECLINATION ANGLES PREDICTED BY A FLAT PLANE SURFACE MODEL IN THERMAL DESKTOP. 60

FIGURE 9.1.2-3: HORIZONS TARGET BODY 61

FIGURE 9.1.2-4: HORIZONS TABLE SETTINGS 62

FIGURE 9.1.2-6: COORDINATE DEFINITION FOR SUN VECTOR 64

FIGURE 9.1.3-1: SOLAR ELEVATION ANGLE VARIATION OVER CALENDAR YEAR 65

FIGURE 9.1.3-2: SOLAR OCCULTATION BASED ON HEIGHT AND DIAMETER 66

FIGURE 9.1.3-3: SOLAR OCCULTATION BASED ELEVATION AND ANGULAR DIAMETER 67

FIGURE 9.2.1-1: THIN SELL DIALOGUE BOX 69

FIGURE 9.2.4-1: PREDICTED LUNAR SURFACE AND SUBSURFACE TEMPERATURES FOR A 1 M^2 SECTION AT -85.393N LATITUDE REACHING CYCLIC STEADY STATE. (TOP) CASE 1: ALL LAYERS START AT 298K. (BOTTOM) CASE 2: LAYER 1 STARTS AT 298K AND LAYERS 2 - 9 START AT 150K. 72

FIGURE 9.3.1.1-1: CONFIGURATION FACTOR ($F1\text{-}2,3$) FOR THE GROUND PLANE TO THE EXTERNAL SURFACE OF A CYLINDER, OF HEIGHT H, RADIUS $R2$, AND DISPLACED A DISTANCE L FROM THE GROUND PLANE, AS A FUNCTION OF NORMALIZE GROUND PLANE RADIUS ($R1/R2$) AND ASPECT RATIO ($AR = H/2R2$). LOCATION OF 5% DELTA FROM $R1/R2 \rightarrow \infty$ ASYMPTOTIC CONFIGURATION FACTOR VALUE INDICATED AS RED DATA POINTS. 76

FIGURE 9.3.1.2-1: CONFIGURATION FACTOR ($F2,3\text{-}1$) FOR THE EXTERNAL SURFACE OF A CYLINDER, OF HEIGHT H, RADIUS $R2$, AND DISPLACED A DISTANCE L FROM THE GROUND PLANE, TO THE GROUND PLANE

AS A FUNCTION OF NORMALIZE GROUND PLANE RADIUS ($R1/R2$) AND ASPECT RATIO ($AR = H/2R2$). LOCATION OF 5% DELTA FROM $R1/R2 \rightarrow \infty$ ASYMPTOTIC CONFIGURATION FACTOR VALUE INDICATED AS RED DATA POINTS. 77

FIGURE 9.3.1.3-1: CONFIGURATION FACTOR ($F1\text{-}2$) FOR THE EXTERNAL SURFACE OF A CYLINDER, OF HEIGHT H, TO THE ANNULAR SURFACE OF THE GROUND PLANE AS A FUNCTION OF NORMALIZE GROUND PLANE RADIUS ($R2/R1$) AND ASPECT RATIO ($AR = H/2R1$). LOCATION OF 5% DELTA FROM $R2/R1 \rightarrow \infty$ ASYMPTOTIC CONFIGURATION FACTOR VALUE INDICATED AS RED DATA POINTS 79

FIGURE 9.3.1.4-1: CONFIGURATION FACTOR ($F2\text{-}1$) FOR THE ANNULAR SURFACE OF THE GROUND PLANE TO THE EXTERNAL SURFACE OF A CYLINDER, OF HEIGHT H, AS A FUNCTION OF NORMALIZE GROUND PLANE RADIUS ($R2/R1$) AND ASPECT RATIO ($AR = H/2R2$). LOCATION OF 5% DELTA FROM $R2/R1 \rightarrow \infty$ ASYMPTOTIC CONFIGURATION FACTOR VALUE INDICATED AS RED DATA POINTS. 80

FIGURE 9.3.1.5-1: CONFIGURATION FACTOR ($F1\text{-}2$) FOR THE EXTERNAL SURFACE OF A SPHERE, AT A DISTANCE H ABOVE THE SURFACE OF THE GROUND PLANE, TO THE GROUND PLANE AS A FUNCTION OF NORMALIZE GROUND PLANE RADIUS ($R2/H$). LOCATION OF 5% DELTA FROM $R2/H \rightarrow \infty$ ASYMPTOTIC CONFIGURATION FACTOR VALUE INDICATED AS RED DATA POINTS. 82

FIGURE 9.3.1.7-1: CONFIGURATION FACTOR ($F1\text{-}2$) FOR THE EXTERNAL SURFACE OF A HEMISPHERICAL DOME, OF RADIUS $R1$, TO THE ANNULAR GROUND PLANE AS A FUNCTION OF NORMALIZE GROUND PLANE RADIUS ($R2/R1$). LOCATION OF 5% DELTA FROM $R2/R1 \rightarrow \infty$ ASYMPTOTIC CONFIGURATION FACTOR VALUE INDICATED AS RED DATA POINTS. 84

FIGURE 9.3.1.8-1: CONFIGURATION FACTOR ($F2\text{-}1$) FOR THE ANNULAR GROUND PLANE TO THE EXTERNAL SURFACE OF A HEMISPHERICAL DOME, OF RADIUS $R1$, AS A FUNCTION OF NORMALIZE GROUND PLANE RADIUS ($R2/R1$). LOCATION OF 5% DEVIATION FROM $R2/R1 \rightarrow \infty$ ASYMPTOTIC CONFIGURATION FACTOR VALUE INDICATED AS RED DATA POINTS. 85

FIGURE 9.3.2-1: LENGTH OF SHADOW DUE TO A BOULDER..... 86

FIGURE 9.3.2-2: SHADOW LENGTH, L, FROM A LARGE OBJECT OF HEIGHT H ON A PERFECTLY SPHERICAL MOON, GIVEN A SOLAR ELEVATION ANGLE A AT POINT P. THE SCALE IS ADJUSTED FOR VISIBILITY. 86

FIGURE 9.4.1-1: NORMALIZED ALTITUDE AS A FUNCTION OF THE NORMALIZED DIFFERENCE BETWEEN $F1\text{-}2$ AND $F1\text{-}\infty$. 89

FIGURE 9.4.2-1: SIMPLE FLAT PLATE FOR SIMPLE ANALYSIS 90

FIGURE 9.4.2-2: COMPARING AND ADJUSTING THERMAL DESKTOP SIMPLE FLAT PLATE TEMPERATURE TO DSNE DATA 91

FIGURE 9.4.2-3: IMAGE FROM QUICKMAPS FOR SUMMER MAX TEMPERATURE AT LUNAR SOUTH POLE 92

FIGURE 9.4.3-1: LUNA 27 FAR-FIELD BOUNDARY 93

FIGURE 9.4.3-2: FAR FIELD BOUNDARY PROJECTION 94

FIGURE 9.4.3-3: TWO DIMENSIONAL LUNAR TOPOLOGY PROJECTION WITH SUPER-IMPOSED SUN TRACKS 94

FIGURE 9.5.1-1: QUICKMAP WEBSITE WINDOWS SEEN WHEN SELECTING AND DOWNLOADING .STL FILES 96

FIGURE 9.5.1-2: EXAMPLE DEM -85N TO THE SOUTH POLE (LEFT) AND POINT CLOUD GENERATED WITH THE ABOVE PROCESS (RIGHT). SOURCE: 'LDEM_85S_40M_FLOAT.IMG' (HTTP://IMBRIUM.MIT.EDU/BROWSE/LOLA_GDR/POLAR/SOUTH_POLE/) 98

FIGURE 10.0-1: EFFECT OF SIMULANT DUST ON AZ-93 SOLAR ABSORPTIVITY FROM GAIER, ET AL.,[3] 106

FIGURE 10.0-2: EFFECT OF SIMULANT DUST ON AG-FEP SOLAR ABSORPTIVITY FROM GAIER, ET AL.,[3] 106

FIGURE 10.0-3: EFFECT OF SIMULANT DUST ON AZ-93 EMISSIVITY FROM GAIER, ET AL.,[3] 107

FIGURE 10.0-4: EFFECT OF SIMULANT DUST ON AG-FEP EMISSIVITY FROM GAIER, ET AL.,[3] 107

FIGURE 10.0-5: EFFECT OF SIMULANT DUST ON AG-FEP AND AZ-93 A/ E FROM GAIER, ET AL.,[3] 107

FIGURE 10.0-6: EFFECT OF VARYING SIMULANT DUST ON AG-FEP AND AZ-93 A/ E FROM GAIER, ET AL.,[4] WITH ANNOTATIONS IN RED. 108

FIGURE 11.1-1: YEARLY VARIATION IN SOLAR ELEVATION ANGLE FOR LOCATION ON THE LUNAR SURFACE (85°N LATITUDE) 110

FIGURE 11.1-2: ILLUMINATED FRACTION OF THE EARTH'S DISK FOR OBSERVER ON LUNAR SURFACE (85°N LATITUDE) 110

FIGURE 11.1-3: SURFACE INCLINATION AND SOLAR ELEVATION ANGLE 111

FIGURE 11.1-4: TYPICAL EARTHSHINE FOR LUNAR LOCATION (85°N, TILT=15°) 111

FIGURE G-1: BIDIRECTIONAL REFLECTANCE 142

FIGURE G-2: SPECTRAL RADIANCE 142

FIGURE G-3: HAPKE/SATO EQUATIONS 143

FIGURE G-4: PHASE FUNCTION PARAMETERS 143

FIGURE G-5: HAPKE PARAMETER MAPS OF THE MOON 144

FIGURE G-6: DIRECTIONAL ALBEDO 145

FIGURE G-7: DIRECTIONAL HEMISPHERICAL ALBEDO 146

1.0 INTRODUCTION

This guidebook describes methodologies for performing lunar thermal analyses in support of the Human Landing System (HLS) Program. This guidebook was compiled by the HLS Lunar Thermal Environments Task Team (L-TETT). This team is comprised of members from Marshall Space Flight Center (MSFC) Natural Environments team and members of the thermal discipline from across NASA, including MSFC, Johnson Space Center (JSC), Glenn Research Center (GRC), and Jet Propulsion Laboratory (JPL).

1.1 PURPOSE

The purpose of the Human Landing System (HLS) Lunar Thermal Analysis Guidebook (L-TAG) is to provide guidance to experienced thermal engineering personnel on how to conduct worst-case hot and cold lunar thermal analyses for the design of HLS hardware in both lunar orbit and lunar surface environments. The HLS L-TAG will include pointers to the Cross-Program Design Specification for Natural Environments (DSNE), SLS-SPEC-159, and best practices/approaches for interpreting and complying with the DSNE lunar thermal environments in the analysis of HLS spacecraft, vehicles and systems. The HLS L-TAG is a reference document that is available to all HLS thermal analysts. In the event of a conflict with the descriptions provided herein, the DSNE takes precedence. This document represents the best available information at the time of publication and will undergo updates as the HLS program evolves. Feedback from the user community is encouraged to support further refinement of the Guidebook. The HLS L-TETT may be reached at msfc-ltett@mail.nasa.gov.

1.2 SCOPE

The baseline version of this document is in support of the HLS Program. Future revisions may expand the scope to include additional lunar programs/missions.

1.3 CHANGE AUTHORITY/RESPONSIBILITY

Proposed changes to this document shall be submitted via a Change Request (CR) to the appropriate HLS Control Board for consideration and disposition. All such requests will adhere to the HLS Configuration and Data Management Plan, documented in HLS-PLAN-004.The appropriate NASA Office of Primary Responsibility (OPR) identified for this document is MSFC EV34, Thermal Analysis and Control Branch.

2.0 DOCUMENTS

2.1 APPLICABLE DOCUMENTS

The following documents include specifications, models, standards, guidelines, handbooks, and other special publications. The documents listed in this paragraph are applicable to the extent specified herein.

SLS-SPEC-159 DSNE is the required design specification called-out in Gateway, Human Landing Systems, and Exploration EVA system requirements. DSNE contains the environments against

which the hardware must be verified. This guidebook contains supplemental information which will aid hardware designers in performing thermal analyses.

Document Number	Document Revision	Document Title
SLS-SPEC-159	Revision G	Cross-Program Design Specification for Natural Environments (DSNE)

3.0 THE EARTH'S MOON

The lunar environment presents many thermal design challenges for exploration, both on the surface of the Moon and in orbit. Due to the rotational period of the Moon, the thermo-physical properties of lunar regolith and the absence of an atmosphere, the Moon's surface thermal environment is much more severe than that of the Earth in both magnitude and variation. Surface temperatures on the Sun-lit side of the Moon can exceed 390 K (242°F) at the equator while dark side temperatures may plunge below 90 K (-298°F) as shown in Figure 3.0-1: Lunar Surface Temperatures. The performance of conventional spacecraft thermal control systems may be compromised or even rendered non-functional in such environments. Spacecraft in low lunar orbits passing directly above or near the lunar sub-solar point (i.e. Sun directly overhead) must account for the impacts of infrared flux emitted from the surface upon thermal radiators. Dust contamination of external thermal control surfaces as well as particulate introduction into crew spaces is a significant concern. Lunar Rover Vehicle (LRV) battery overheating was an issue on both Apollo 16 and 17 due to lunar dust accumulation on the LRV radiator.

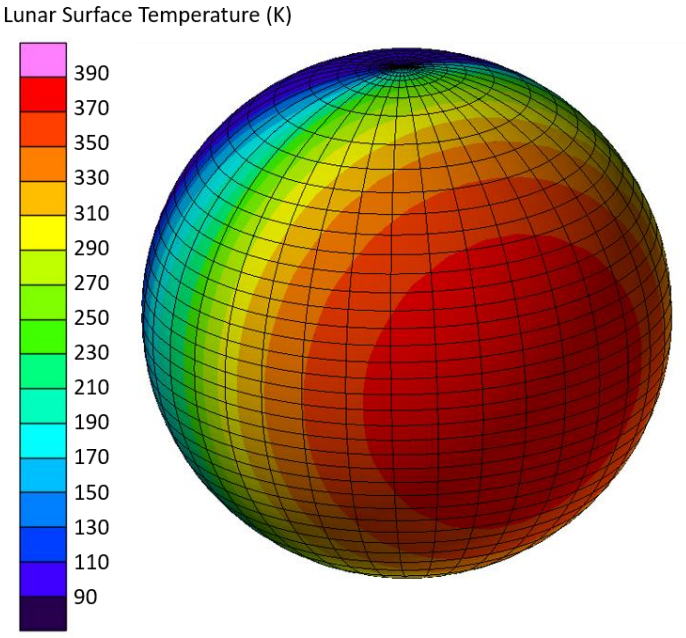

FIGURE 3.0-1: LUNAR SURFACE TEMPERATURES

The Apollo missions were constrained by the lunar thermal environment in both duration and landing time of day. Because of the thermal environment, waste heat rejection was accomplished via water evaporation or sublimation from on-board water stores. The Apollo LEM (Lunar Excursion Module) onboard water supply of 415 pounds was distributed between multiple tanks in the descent and ascent stages. Since the cooling water was consumed for drinking as well, this further imposed limits on mission duration. And perhaps the most difficult thermal challenge for sustained lunar exploration is surviving the long night without sunlight or a naturally occurring heat source. Advanced thermal storage, switches and isolation as well as variable heat rejection radiator technology are all areas of active research to mitigate the consequences of the lunar night.

3.1 PHYSICAL CHARACTERISTICS

As observed from the Earth, the Moon's surface is characterized by large dark regions known as maria. The lighter surfaces on the lunar surface are referred to as highlands. Owing to a greater iron oxide composition, the maria are not as reflective as the lunar highlands and were so named by ancient astronomers who mistakenly interpreted the maria as oceans. The near side of the Moon has more maria than the far side of the Moon (Figure 3.1-1).

FIGURE 3.1-1: **NEAR AND FAR SIDES OF THE MOON**

The lunar surface is characterized by a layer of regolith of variable thickness depending upon location as described in DSNE 3.4.2.1. Composition of the regolith is presented in Table 3.1-1. Lunar regolith is a thermal insulator with a low thermal diffusivity. Because of the low regolith thermal conductivity, diurnally induced phenomena at the surface are generally not felt thermally beyond 1 meter in depth (see 5.3.1). This guidebook includes considerations for modeling the lunar surface based upon observed thermo-physical properties.

TABLE 3.1-1: AVERAGE CHEMICAL COMPOSITION OF LUNAR SURFACE REGOLITH [1]

	Maria (wt%)	Highlands (wt%)
SiO_2	45.4%	45.5%
Al_2O_3	14.9%	24.0%
CaO	11.8%	15.9%
FeO	14.1%	5.9%
MgO	9.2%	7.5%
TiO_2	3.9%	0.6%
Na_2O	0.6%	0.6%

The atmosphere of the Moon is virtually non-existent with a mean pressure of 3×10^{-15} bar [2].

3.2 ORBIT

The orbital relationship between the Earth, Moon and Sun is illustrated in Figure 3.2-1. Like many planetary satellites in the Solar System, the Moon is tidally locked to its partner so that the rotational period is the same as its orbital period about the Earth and, aside from small deviations due to libration, one side of the Moon always faces the Earth. The Moon's axis of rotation is tilted 1.542° relative to the ecliptic plane while the lunar orbit plane is inclined 5.145° relative to the ecliptic plane. The lunar obliquity (inclination to the orbit plane) is the sum of the two angles (6.68°).

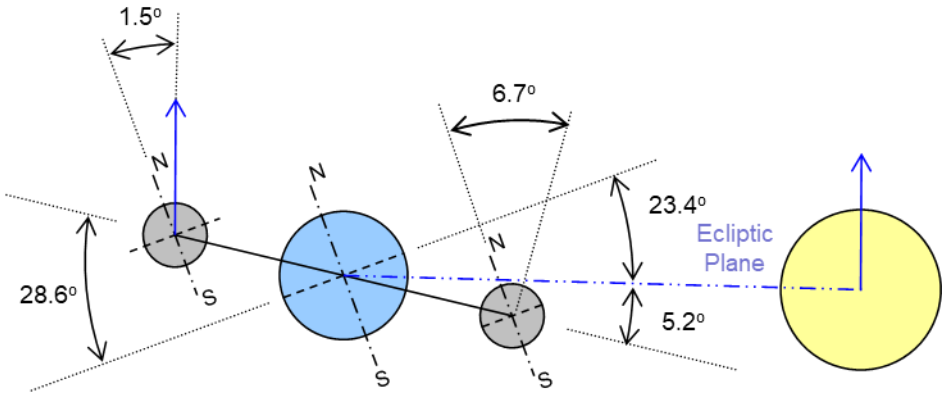

Figure 3.2-1: Lunar Orbit

The lunar orbit is slightly eccentric (~0.055) with a mean distance from the Earth of 384,403 km. Precession of the lunar orbit completes one revolution in 18.6 years (or about 19° per year). Because of precession, the lunar orbit may be flipped about the ecliptic plane with an inclination ranging between 18.28° and 28.58° (as shown in Table 3.2-1) over the 18.6 year period.

TABLE 3.2-1: LUNAR ORBIT PARAMETERS [1]

Parameter	Value
Semi-major axis (km)	384400
Perigee (km)	363300
Apogee (km)	405500
Sidereal rotation period (days)	27.322
Synodic period (days)	29.530
Inclination to ecliptic (deg)	5.145
Inclination to Earth equator (deg)	18.28 - 28.58
Lunar Obliquity to Ecliptic (deg)	1.542
Orbit eccentricity	0.0549
Obliquity to orbit (deg)	6.68

The rotational (and orbital) period of the Moon can be characterized relative to both a fixed point in space (Sidereal) and to the Sun (Synodic). The Sidereal period is on the order of 27.3 days while the Synodic period is on the order of 29.5 days (Figure 3.2-2). The Synodic period of 29.5 days represents sunrise to sunrise for a reference point on the surface of the Moon (as well as a New Moon to New Moon as viewed from the Earth). For an asset on the lunar surface, the Sun angle is periodic over the Synodic period and would be more pertinent for thermal assessments.

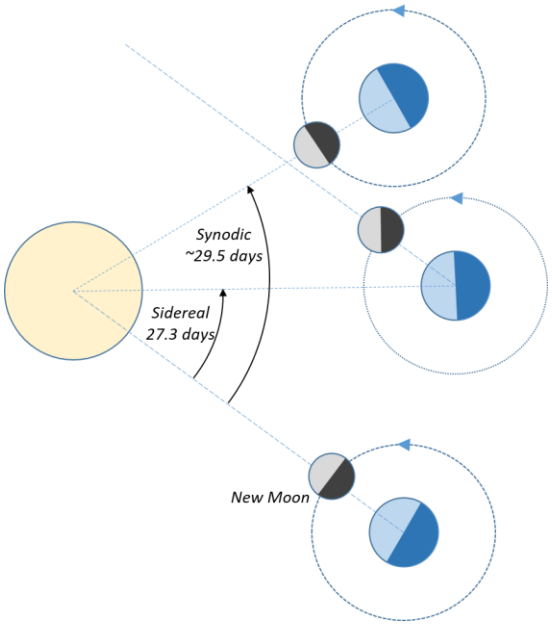

FIGURE 3.2-2: LUNAR ORBITAL PERIOD

The Moon's small obliquity relative to the ecliptic plane results in a mild seasonal variation that is especially significant at the poles. At the poles, regions of nearly continuous sunlight might exist at sufficient altitude while regions of perpetual shade (no direct solar insolation) may exist in

craters as illustrated in Figure 3.2-3. The maximum Sun elevation angle at the poles is related to the Moon's obliquity relative to the ecliptic plane. Nearly constant illumination is desirable for avoiding the long lunar night while portions of perpetually shadowed lunar craters may contain frozen water. The seasonal variation at the lunar South Pole is evident from bolometric temperature measurements made by the Diviner Lunar Radiometer Experiment of the Lunar Reconnaissance Orbiter (LRO) as shown in Figure 3.2-4 [3].

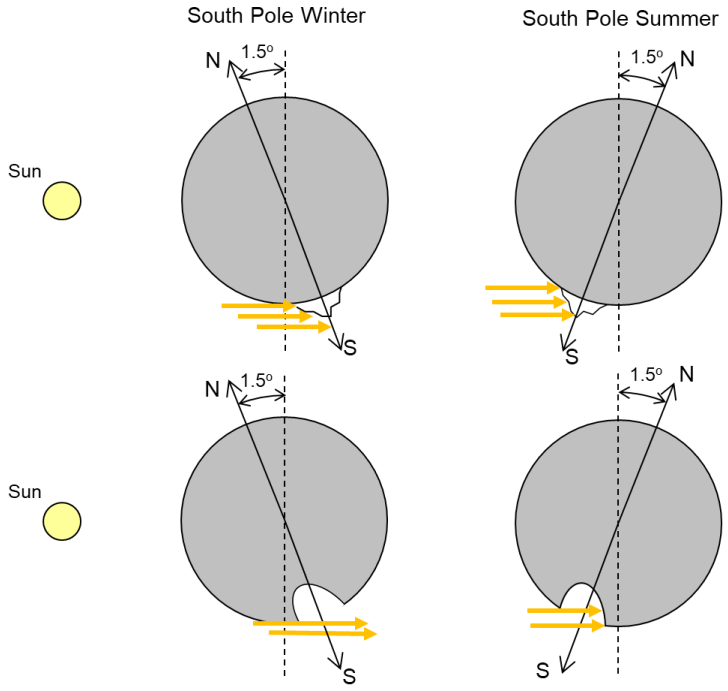

FIGURE 3.2-3: SEASONAL VARIATION ON THE MOON

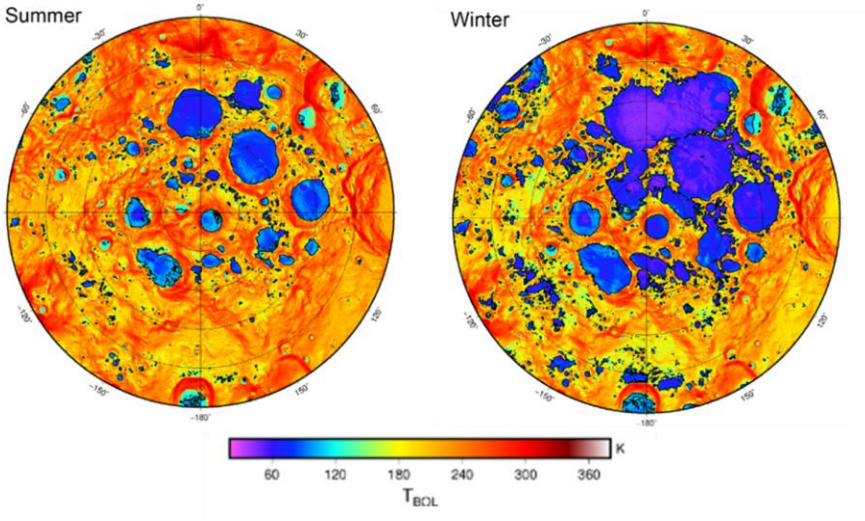

FIGURE 3.2-4: DIVINER MAXIMUM BOLOMETRIC TEMPERATURES OF THE SOUTH POLE (85°-90°S) SPLIT INTO SEASONS

[1] Stuart Ross Taylor, "Lunar Science: a Post-Apollo View", *Lunar Science Institute*, Pergamon Press, New York, p. 64. ISBN 978-0080182742, 1975.
http://articles.adsabs.harvard.edu//full/1975lspa.book.....T/0000001,004.html

[2] Planetary Fact Sheet, NSSDCA-NASA,
https://nssdc.gsfc.nasa.gov/planetary/factsheet/moonfact.html

[3] J. P. Williams, et al, "Seasonal Variations in South Polar Temperatures on the Moon", 50th Lunar and Planetary Science Conference 2019, LPI Contribution #2132, 2019.

4.0 LUNAR SPACE THERMAL ENVIRONMENTS

DSNE section 3.3.9.1 defines the extreme environments for thermal analysis in cis-lunar space. Information in section 4.0 is sufficient for modeling lunar orbiting spacecraft. Guidance for lunar surface vehicle analysis is provided in greater detail in section 5.0.

4.1 SOLAR CONSTANT

DSNE section 3.3.9.1.1 defines the mean Solar Constant value at 1 Astronomical Unit (AU) distance from the Sun and the maximum and minimum values account for variation in the distance of the Earth from the Sun in addition to the distance from the Moon to the Earth. The variation in these values is greater than the solar flux range provided in DSNE 3.3.9.2 for near Earth phases. The values given in DSNE do not include a ±5 W/m^2 measurement uncertainty which should be accounted for when producing enveloping environments.

4.2 ALBEDO

DSNE section 3.3.9.1.2 defines maximum, minimum, and average lunar albedo values for the near and far side of the Moon. These values are used to determine the amount of solar energy returned from the lunar surface to an orbiting spacecraft and also part of the calculations defining lunar surface long-wave radiance. For high altitude orbits, such as Near Rectilinear Halo Orbit (NRHO), the spatially averaged values may be more appropriate.

4.3 LUNAR LONG-WAVE RADIANCE

The lunar normal long-wave radiance for use in thermal analysis is specified in DSNE 3.3.9.1.3. Given the slow rotation of the Moon, effects of the lunar surface thermal capacitance are neglected. Lunar long-wave radiance is defined as a function of temperature and emissivity of the surface or a function of albedo, solar flux and solar incidence angle in thermal balance as indicated by analysis of the Clementine mission Long-Wave Infrared Camera (LWIR). Minimum values are given for unilluminated lunar surfaces. This environment can be included in analysis models as analytical expressions or as Latitude/Longitude tables.

4.3.1 Analytical Expressions

The analytical expressions provided in DSNE 3.3.9.1.3 approximate the lunar surface temperature using solar incidence angle. Using the equation as given in DSNE for the entire lunar surface will result in a lunar surface temperature of 0 K when the incidence angle approaches 90°

which then jumps to the given surface temperature for the unilluminated side of the Moon. The equations provided in this section account for this discontinuity (as suggested by DSNE).

It is possible to use these equations and orbital parameters to develop a time or true anomaly varying lunar surface radiance as if coming from a single point on the surface nadir to the spacecraft. This might be sufficient for low altitudes, but as orbital altitude increases the whole view factor from spacecraft to planet needs to be integrated.

When integrating the spacecraft to planet view factor it is useful to define the planetary radiance gradient in terms of the planetary or subsolar coordinate system. If using planetary latitudes and longitudes it is necessary to include the tilt of the Moon's axis of rotation (1.54°) from the solar ecliptic when accounting for location of the lunar subsolar point. The Subsolar Coordinate equation is adapted to the convention in Thermal Desktop (TD) orienting the planet +Z axis to the Sun and +X axis in the equatorial plane. This varies from the Planetary Coordinate system convention which defines the +Z axis through the north pole and the +X axis through the prime meridian.

For Planetary Coordinate System:

If ($-90° \le (Long_{planetary} - Long_{subsolar}) \le 90°$) Then

$$Q_{IR} = \left(cos\left(Long_{planetary} - Long_{subsolar}\right) \cdot \left(Lat_{planetary} - Lat_{subsolar}\right)\right) \cdot \left((1\text{-a}) \cdot S_0 - \sigma \cdot \varepsilon \cdot T_{Dark}^{\ 4}\right) + \sigma \cdot \varepsilon \cdot T_{Dark}^{\ 4}$$

Else

$$Q_{IR} = \sigma \cdot \varepsilon \cdot T_{Dark}^{\ 4}$$

For Subsolar Coordinate System:

If ($Lat_{SS} \ge 0°$) Then

$$Q_{IR} = \sin(Lat_{SS}) \cdot \left((1 - a) \cdot S_0 - \sigma \cdot \varepsilon \cdot T_{Dark}^{\ 4}\right) + \sigma \cdot \varepsilon \cdot T_{Dark}^{\ 4}$$

Else

$$Q_{IR} = \sigma \cdot \varepsilon \cdot T_{Dark}^{\ 4}$$

Where:

Q_{IR}	Planetshine from a point on the lunar surface
σ	Stefan-Boltzmann Constant
a	Lunar surface albedo
ε	Lunar Surface Emissivity
S_0	Solar Flux
T_{dark}	unilluminated lunar surface temperature
$Long_{planetary}$	degrees longitude (Planet Coordinate System)
$Lat_{planetary}$	degrees latitude (Planet Coordinate System)
$Long_{subsolar}$	degrees longitude of lunar subsolar point (Planet Coordinate System)
$Lat_{subsolar}$	degrees latitude of lunar subsolar point (Planet Coordinate System)
Lat_{SS}	degrees latitude from subsolar point (Subsolar Coordinate System)

Example inputs for the above equations are listed below in Table 4.3.1-1. These values are taken from DSNE section 3.3.9.1 and do not supersede any updates therein. Because lunar longwave

radiance varies inversely with lunar albedo, it is recommended to conduct multiple analysis cases to check for vehicle and component sensitivities in the different wavelength bands. It is not recommended to maximize or minimize both albedo and long-wave radiance in single analysis as this condition does not occur.

TABLE 4.3.1-1 LUNAR LONG-WAVE RADIANCE ALBEDO AND EMISSIVITY EQUATION INPUTS

Cold Case							
Solar	Min Albedo		Combined Cold		Min OLR		Unilluminated Surface
(W/m2)	Albedo	Emissivity	Albedo	Emissivity	Albedo	Emissivity	Temperature (K)
1310	0.07	0.95	0.15	0.95	0.2	0.95	80
Hot Case							
Solar	Max Albedo		Combined Hot		Max OLR		Unilluminated Surface
(W/m2)	Albedo	Emissivity	Albedo	Emissivity	Albedo	Emissivity	Temperature (K)
1426	0.2	0.98	0.12	0.98	0.07	0.98	120

4.3.2 Latitude/Longitude Tables of Lunar Surface Flux and/or Temperature

Lunar long-wave radiance is also referred to Outgoing Long-wave Radiation (OLR) and Planetshine. This environment can be included as Latitude/Longitude tables in analysis tools which calculate view factors from the spacecraft to the planet and integrate the lunar surface long-wave radiance. These can be generated with grids of measured surface temperature data or approximated using the equations provided in section 4.3.1. Analysts are cautioned to ensure that the lunar subsolar latitudes and longitudes are consistent for solar flux and lunar long-wave radiance calculations. Using the subsolar coordinate system option provided by Thermal Desktop resolves this potential discrepancy by keeping a solar inertial planetary coordinate system independent of the orbit defined planetary prime meridian. The Subsolar Coordinate System is defined with the +Z-axis towards the Sun and the +X-axis in the equatorial plane. The subsolar point is positioned at a latitude of +90°.

When generating tables of lunar radiance, care should be taken to understand how these inputs are used by the analysis software and how the discretization of the table will affect the analysis results. Table 4.3.2-1 has example values for hot case lunar radiance in Planetary (a) and Subsolar (b) coordinates that are coarsely discretized and provided for guidance. Thermal Desktop formatting requires values for longitudes from -180° to 180°and latitudes from -90° to 90°. There is no need to include interpolation points beyond the terminator in planetary (longitudes <-90° or >90°) or subsolar (latitudes <0°) coordinate systems since the unilluminated side of the Moon is assumed to be isothermal in DSNE. For the subsolar coordinate system, the lunar radiance does not vary with longitude since the +Z axis is set through the subsolar point instead of the lunar north pole. A subsolar table with columns for longitudes of only -180° and 180° would be sufficient, as is evident in Table 4.3.2-1(b).

TABLE 4.3.2-1 HOT CASE LUNAR RADIANCE, COMBINED VALUES

Planetary Latitude \ Planetary Longitude	-180	-90	-80	-70	-60	-50	-40	-30	-20	-10	0	10	20	30	40	50	60	70	80	90	180
-90	12	12	12	12	12	12	12	12	12	12	12	12	12	12	12	12	12	12	12	12	12
-80	12	12	49	85	119	150	177	199	214	224	227	224	214	199	177	150	119	85	49	12	12
-70	12	12	85	157	224	285	337	380	411	430	437	430	411	380	337	285	224	157	85	12	12
-60	12	12	119	224	322	411	488	550	596	624	633	624	596	550	488	411	322	224	119	12	12
-50	12	12	150	285	411	525	624	704	763	799	811	799	763	704	624	525	411	285	150	12	12
-40	12	12	177	337	488	624	741	836	907	950	964	950	907	836	741	624	488	337	177	12	12
-30	12	12	199	380	550	704	836	944	1023	1072	1088	1072	1023	944	836	704	550	380	199	12	12
-20	12	12	214	411	596	763	907	1023	1109	1162	1180	1162	1109	1023	907	763	596	411	214	12	12
-10	12	12	224	430	624	799	950	1072	1162	1217	1236	1217	1162	1072	950	799	624	430	224	12	12
0	12	12	227	437	633	811	964	1088	1180	1236	**1255**	1236	1180	1088	964	811	633	437	227	12	12
10	12	12	224	430	624	799	950	1072	1162	1217	1236	1217	1162	1072	950	799	624	430	224	12	12
20	12	12	214	411	596	763	907	1023	1109	1162	1180	1162	1109	1023	907	763	596	411	214	12	12
30	12	12	199	380	550	704	836	944	1023	1072	1088	1072	1023	944	836	704	550	380	199	12	12
40	12	12	177	337	488	624	741	836	907	950	964	950	907	836	741	624	488	337	177	12	12
50	12	12	150	285	411	525	624	704	763	799	811	799	763	704	624	525	411	285	150	12	12
60	12	12	119	224	322	411	488	550	596	624	633	624	596	550	488	411	322	224	119	12	12
70	12	12	85	157	224	285	337	380	411	430	437	430	411	380	337	285	224	157	85	12	12
80	12	12	49	85	119	150	177	199	214	224	227	224	214	199	177	150	119	85	49	12	12
90	12	12	12	12	12	12	12	12	12	12	12	12	12	12	12	12	12	12	12	12	12

(a)

Subsolar Latitude \ Subsolar Longitude	-180	0	180
-90	12	12	12
0	12	12	12
5	120	120	120
10	227	227	227
15	333	333	333
20	437	437	437
25	537	537	537
30	633	633	633
35	725	725	725
40	811	811	811
45	891	891	891
50	964	964	964
55	1030	1030	1030
60	1088	1088	1088
65	1138	1138	1138
70	1180	1180	1180
75	1213	1213	1213
80	1236	1236	1236
85	1250	1250	1250
90	**1255**	**1255**	**1255**

(b)

S_0 = 1426 W/m^2, a = 0.12, e = 0.98, T_{dark} = 120K)

The lunar surface colored by planetary radiance in subsolar coordinate system is shown in Figure 4.3.2-1a. The planetshine subsolar point (purple arrow) is shown properly positioned with respect to the solar vector (yellow arrow) and shadow cone. Figure 4.3.2-1b shows what may happen if care is not taken to align the planetshine subsolar point with the solar vector when using the planetary coordinate system. This caution is more significant when using vector list trajectories as there is no mechanism to align the planetshine subsolar point system to the solar vector in the orbit definition when using the planetary coordinate system.

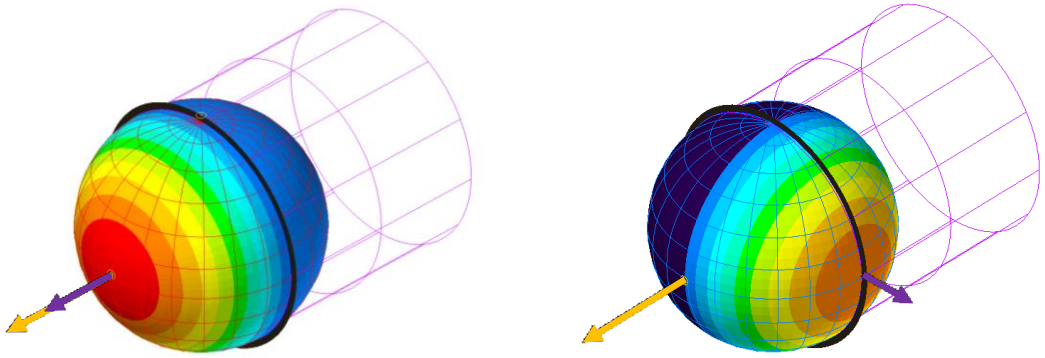

(a) Aligned (b) Misaligned

FIGURE 4.3.2-1: COORDINATING SUBSOLAR POINTS FOR SOLAR AND PLANETSHINE USING A PLANETARY COODINATE SYSTEM.

4.4 SOLAR ECLIPSE DURATIONS

4.4.1 Low Lunar Orbit

4.4.1.1 Earth Shadow

For Low Lunar Orbits (LLO), DSNE 3.3.9.1.4 describes worst case durations of a lunar eclipse at various circular orbital altitudes about the Moon for the worst case lunar eclipse during the years 2018-2035. Note that a solar eclipse viewed from the Moon (the Earth being between the Sun and the Moon) would be called a lunar eclipse when viewed from Earth. DSNE Table 3.3.9.1.4-1 includes the duration a spacecraft could experience eclipse totality and the duration of consecutive eclipse totality and lunar orbital shadow. These durations represent the worst case duration of no solar flux or albedo on a spacecraft in LLO. The surface temperature of the near side of Moon also drops significantly as the Moon passes through penumbra, partial and full eclipse. This results in a reduction of the longwave radiance from the near side of the Moon. Figure 4.4.1.1-1 reproduces Earth-based temperature measurements taken of 7 zones on the near side of the Moon during the February 10, 1971 lunar eclipse showing this temperature decrease [1].

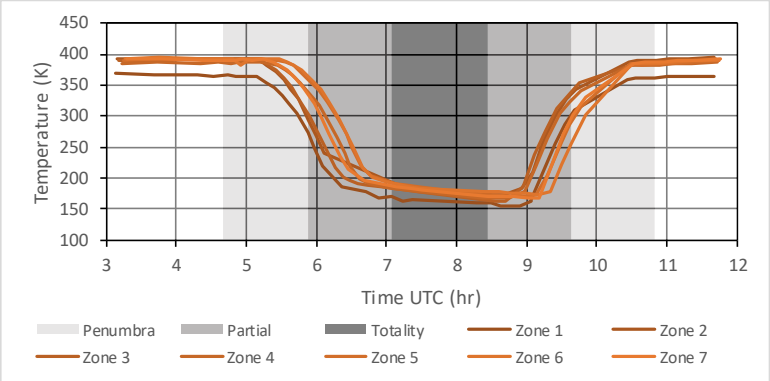

Figure 4.4.1.1-1: Lunar Eclipse Surface Temperatures, February 1971

To model the lunar space environments during a lunar eclipse, the Solar and Albedo environments should be set to zero for the duration of partial and total eclipse. Lunar longwave radiance should also be set to the unilluminated side values. This approach to lunar radiance during an eclipse is conservatively cold, but the radiance from the eclipsed lunar surface is not much greater than that from the unilluminated side of the Moon.

4.4.1.2 Lunar Shadow

For orbital mission timelines not inclusive of a lunar eclipse, normal shadowing by the Moon calculated by orbital parameters represents the worst case.

4.4.2 Near-Rectilinear Halo Orbit

4.4.2.1 Earth Shadow

For the NASA Gateway Near-Rectilinear Halo Orbit (NRHO), calculations by Johnson Space Center show that the planned 9:2 Lunar Synodic Resonant NRHO is able to mostly avoid eclipse by Earth shadow from January 2020 to February 2035, with two partial eclipses during the 14th and 15th years. These could also be avoided with orbital modifications [2].

4.4.2.2 Lunar Shadow

Eclipses by the Moon would occur several times every year, but are always less than 80 minutes. For Solar Eclipses by the Moon in an NRHO (GATEWAY) orbit, the minimum, mean, and maximum eclipse durations are given in Table 5 of the Gateway Integrated Thermal Model Development IAC4r0 document [3] and shown below in Table 4.4.2.2-1.

TABLE 4.4.2.2-1 DURATION IN LUNAR SHADOW FOR GATEWAY NRHO

Shade	Minimum [minutes]	Mean [minutes]	Maximum [minutes]
Penumbra	0.9	52.5	76.1
Umbra	10.2	49.9	73.2

[1] W. F. Fountain, et.al, “Observational and Theoretical Temperatures for a Total Lunar Eclipse”, “The Moon”, p421-437, 1976]

[2] D. E. Lee, “Gateway Destination Orbit Model: A Continuous 15 year NRHO Reference Trajectory”, NTRS 20190030294, Aug. 2019

[3] J. R. Smith. “Gateway Passive Thermal Guidelines and Model Utilization – IAC4”, Oct. 2019

5.0 LUNAR SURFACE THERMAL ENVIRONMENTS

DSNE 3.4.6 describes the lunar surface thermal environments which consist of radiative (direct solar insolation, sunlight reflected from the lunar surface, and emitted infrared from the lunar surface) and conduction with the lunar surface.

5.1 SURFACE FEATURES

DSNE 3.4.1 describes the lunar surface geology and geomorphology. The most relevant geologic parameter for thermal analysis is whether a particular location is on the maria or highlands (see 3.1). The different composition of the material in these terrains affect the albedo of the surface, see DSNE 3.4.6.1.1.

The geomorphology of the surface and its topography also affect the thermal environment by (1) affecting solar visibility and azimuth on slopes, (2) controlling shadowing, (3) reflecting radiation, and (4) reducing the fraction of visible sky to radiate heat into. Factors three and four are usually not that important, but would be significant for certain environments on the Moon’s surface (narrow subsurface pits, polar craters).

[1] M. B. K. Langseth, “In-situ measurements of lunar heat flow,” 1977.

[2] M. G. Langseth, S. J. Keihm, and K. Peters, “Revised lunar heat-flow values.,” *Lunar and Planetary Science Conference Proceedings*, vol. 3, p. 3143, Apr. 1976.

5.1.1 Crater Size Distribution/Topography

DSNE 3.4.1.1 provides a description of the crater size-frequency distribution and 3.4.1.2 describes the topography (crater depth to crater diameter ratios) for fresh lunar craters. The depth-diameter values in the DSNE for fresh craters imply the least sky visibility/most-shadowed case because the depth/diameter of craters decrease as they become less fresh.

For the depth-diameter ratio ζ in DSNE Table 3.4.1.2-1 an idealized, radially-symmetric crater shape model to test the thermal environment for the inside of a crater is:

$$h(r) = \begin{cases} \mathrm{D}\,(-0.825\,\zeta) & [flat\ floor, r < 0.2R] \\ \mathrm{D}\,(-0.825\,\zeta) + (r - 0.2)(\dfrac{\zeta}{0.8}) & [interior\ wall, 0.2R < \ r < R] \\ \mathrm{D}\,(0.175\,\zeta)\,r^{-3} & [outside\ crater, r > R] \end{cases}$$

for crater depth h, radial distance *r* from crater center, crater diameter D, and crater radius *R*. This shape model is only applicable to craters smaller than D=10-15 km.

The DSNE does not define a crater shape model for so-called complex craters (D>10-15 km), partly because the shape and depth/diameter ratio of these craters is known to be somewhat variable at a given size, and also vary significantly with size. If a function of complex crater properties is needed, however, an approximation for the depth of fresh complex craters as a function of diameter is $d=1.044D^{0.301}$. The flat floors of complex craters also extend to a larger fraction of craters’ interiors as size increases, $D\_flat=0.187D^{1.249}$.

For missions defined to landing sites with craters that have been specifically identified, it would be most advisable to use measured lunar topography to generate appropriate meshes (9.4.1).

5.1.2 Boulders/Rocks

DSNE 3.4.1.4 describes the rock size distributions for the lunar surface. See (Hayne et al. 2017) for discussion on how the presence of rocks impacts LRO diviner measured temperatures.

Rocks and boulders have different thermophysical properties than lunar regolith. These properties vary based on composition and rock type. DSNE 3.4.6.2.1 provides a general range of values. Thermal conductivities, specific heats, and thermal diffusivities of Apollo 11 rocks or rocks with similar material compositions are given in (Cremers 1974). Reflectances of chips of lunar rocks taken during Apollo 11 are given by (Birkebak 1974).

[1] P. O. Hayne *et al.*, “Global Regolith Thermophysical Properties of the Moon from the Diviner Lunar Radiometer Experiment: Lunar Regolith Thermophysical Properties,” *J. Geophys. Res. Planets*, vol. 122, no. 12, pp. 2371–2400, Dec. 2017.

[2] Cremers, C.J., 1974, “Heat Transfer Within the Lunar Surface Layer,” in Advances in Heat Transfer, vol. 10, J. P. Hartnett and T. F. Irvine, Eds. Elsevier, 1974, pp. 39–83.

[3] R. C. Birkebak, “Thermal Radiation Properties of Lunar Materials from the Apollo Missions,” in *Advances in Heat Transfer*, vol. 10, J. P. Hartnett and T. F. Irvine, Eds. Elsevier, 1974, pp. 1-37.

5.1.3 LRO Diviner Digital Surface Data

The LROC QuickMap website (https://quickmap.lroc.asu.edu) is a public website that displays 3D, cylindrical and polar stereographic projections of the Moon. Please refer to Section 9.4.1 of this document for detailed instructions on accessing and utilizing the digital surface data.

5.2 SURFACE TEMPERATURE

5.2.1 LRO Diviner Digital Temperature Data Maps

LRO’s Diviner instrument measures the emitted radiance in multiple thermal infrared bands. These are converted to bolometric surface temperatures by fitting an equivalent blackbody across the Diviner wavelengths. Native spatial resolution of Diviner is 160m cross-track by 320 m along-track at a 50-km orbit (note that many released products down sample from this native resolution).

Raw Diviner data (“Level 0” and “Level 1”) are extremely complex due to variation in observation conditions (spacecraft orbit, local time, season, etc.) and the use of these low-level data should be avoided if possible. The Diviner team has released a number of derived products for the globe and pole, available at the team website: https://www.diviner.ucla.edu/data and the Planetary Data System Geosciences node: https://pds-geosciences.wustl.edu/missions/lro/diviner.htm.

The global products below are described in Williams, J. P., Paige, D. A., Greenhagen, B. T., & Sefton-Nash, E. (2017). The global surface temperatures of the Moon as measured by the Diviner Lunar Radiometer Experiment. Icarus, 283, 300-325.

Global products:

- http://luna1.diviner.ucla.edu/~jpierre/diviner/level4_raster_data/diviner_tbol_min.xyz

Table of minimum bolometric temperatures at 0.5 pixels per degree spatial resolution. Format is ascii: lon, lat, bolometric temperature in K.

- http://luna1.diviner.ucla.edu/~jpierre/diviner/level4_raster_data/diviner_tbol_max.xyz

Table of maximum bolometric temperatures at 0.5 pixels per degree spatial resolution. Format is ascii: lon, lat, bolometric temperature in K.

- http://luna1.diviner.ucla.edu/~jpierre/diviner/level4_raster_data/diviner_tbol_hour00.xyz

Table of mean bolometric temperatures ±1 hour around midnight local time, gridded at 0.5 pixels per degree spatial resolution. Format is ascii: lon, lat, bolometric temperature in K.

- http://luna1.diviner.ucla.edu/~jpierre/diviner/level4_raster_data/diviner_tbol_hour12.xyz

Table of mean bolometric temperatures ±1 hour around noon local time, gridded at 0.5 pixels per degree spatial resolution. Format is ascii: lon, lat, bolometric temperature in K.

- http://luna1.diviner.ucla.edu/~jpierre/diviner/level4_raster_data/diviner_tbol_snapshot_**XXX**E.xyz

Replacing **XXX** with a number between 000 and 345 (in °E) gives a table of the instantaneous observed bolometric temperatures across the Moon at a given subsolar longitude **XXX** (e.g., noon at 30°E, replace **XXX** with 030). Gridded at 0.5 pixels per degree spatial resolution. Format is ascii: lon, lat, bolometric temperature in K.

Polar Products:

In addition to these global data, the Diviner team has released higher-resolution (240 m/px) data sets in the polar regions (http://luna1.diviner.ucla.edu/~jpierre/diviner/level4_polar/). These are described in Williams, J.-P., Greenhagen, B. T., Paige, D. A., Schorghofer, N., Sefton-Nash, E., Hayne, P. O., et al. (2019). Seasonal polar temperatures on the Moon. Journal of Geophysical Research: Planets, 124, 2505– 2521. https://doi.org/10.1029/2019JE006028. Descriptions of the data products from this study are described at http://luna1.diviner.ucla.edu/~jpierre/diviner/level4_polar/aareadme.txt.

Example data of interest include surface temperatures at polar latitudes in 1/96th increments of the lunar day in the winter and summer seasons.

The data are released in ascii tables and GMT-formatted binary files (.grd // a netcdf binary format) and as PNG browse files. The ascii files are formatted x,y,lon,lat,bolometric temperature. In the ascii files and GMT/netcdf grd files, the x and y values need to be converted to polar-stereographic meter coordinates by multiplying by the lunar radius (1737400m).

For some data analysis purposes, it is useful to convert the GMT/netcdf grd files to geotiff format (e.g., for use in a GIS software package, such as ArcMap or QGIS). The easiest tool for this is gdal (https://gdal.org/); available through conda on many systems, see https://anaconda.org/conda-forge/gdal.

For example, file polar_south_80_summer_tbol-ltim01.grd can be converted to a geotiff as follows:

gdal_translate polar_south_80_summer_tbol-ltim01.grd polar_south_80_summer_tbol-ltim01.tif -a_ullr \-304005.365165 304005.365165 304005.365165 \-304005.365165 -a_srs '+proj=stere +lat_0=-90 +lon_0=0 +k=1 +x_0=0 +y_0=0 +a=1737400 +b=1737400 +units=m +no_def' -a_nodata 0

ltim files run from 01 to 96. local noon is 48 and local midnight is 96. Converting a `polar_north` file is similar but with the center latitude for the polar stereographic projection: `+lat_0=90`

As an alternative, the grd files can be read in MATLAB® using:

xvalues=ncread('polar_south_80_summer_tbol-ltim01.grd','x');

yvalues=ncread('polar_south_80_summer_tbol-ltim01.grd','y');

zvalues=ncread('polar_south_80_summer_tbol-ltim01.grd','z');

In MATLAB®, X and Y values would again need to be converted to polar stereographic X/Y by multiplying by 1737400.

5.2.2 Analytical Expressions (Steady State Approximation)

Lunar surface temperatures are a function of direct incident sunlight, reflected sunlight, with nearby surfaces, conduction to or from objects on the surface, and subsurface heat flow. Radiative components of the energy exchanged between a flat section of the Moon's surface and an object on it is shown in Figure 5.2.2-1. Since the lunar surface has a very low thermal conductivity, surface temperatures are particularly sensitive to shading from vehicles or surface features.

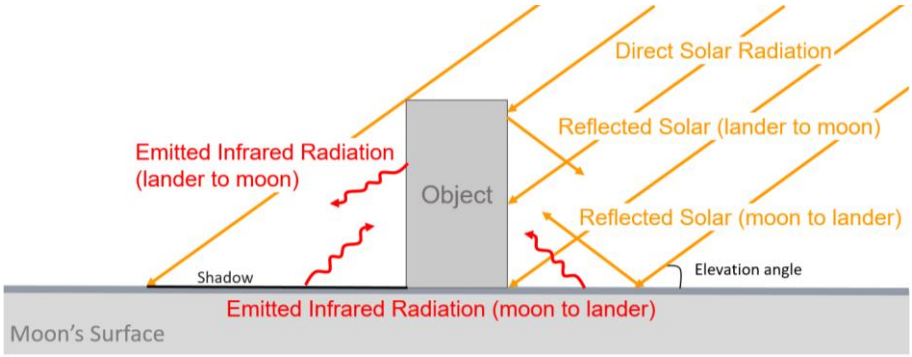

Figure 5.2.2-1: Radiation exchange at the lunar surface.

For equatorial locations, such as the Apollo landing sites, daytime surface temperatures can be approximated by an energy balance across the surface itself.

Consider a differential element of the lunar surface, dA_{moon}, that views deep space. The steady state energy balance is then:

$$dA_{moon} S_O \alpha \cos(\theta_z) = dA_{moon} \varepsilon \sigma {T_m}^4$$

where S_o is the solar flux), θ_z is the solar zenith angle, α is the ground absorptivity (in the solar spectrum), ε is the ground emissivity (in the infrared spectrum), σ is the Stefan-Boltzmann constant ($= 5.6704 * 10^{-8} \left[\frac{W}{m^2 K^4}\right]$), and T_m is the Moon's surface temperature.

The surface temperature, T_m is then:

$$T_m = \left(\frac{\alpha\, S_O \cos(\theta_z)}{\varepsilon \sigma}\right)^{0.25}, where\ \theta_z = 90 - \theta_a$$

θ_a is the solar elevation angle calculated by:

$$\theta_a = \sin^{-1}\left(\sin(\delta)\sin(\theta_{lat}) + \cos(\delta)\cos\left(\theta_{s,t}\right)\cos(\theta_{lat})\right)$$

where, δ is the solar declination angle, (i.e. the angle between the equator and the axis of the Moon's rotation which ranges between ±1.54°), θ_{lat} is the latitude in degrees, and $\theta_{s,t}$ is angle from the Sun at a particular time that changes as the Moon rotates (parallel to longitude) (Maslanka 2018).

To plot T verses time,$\theta_{s,t}$, can be calculated with

$$\theta_{s,t} = \frac{360}{\left(\frac{(solar\ day\ [hrs])}{time\ segment\ [hr]}\right)} + \theta_{s,t-1}$$

Figure 5.2.2-2 shows how using this approach at the Apollo 17 landing site compares to measured surface temperatures (Langseth 1977).

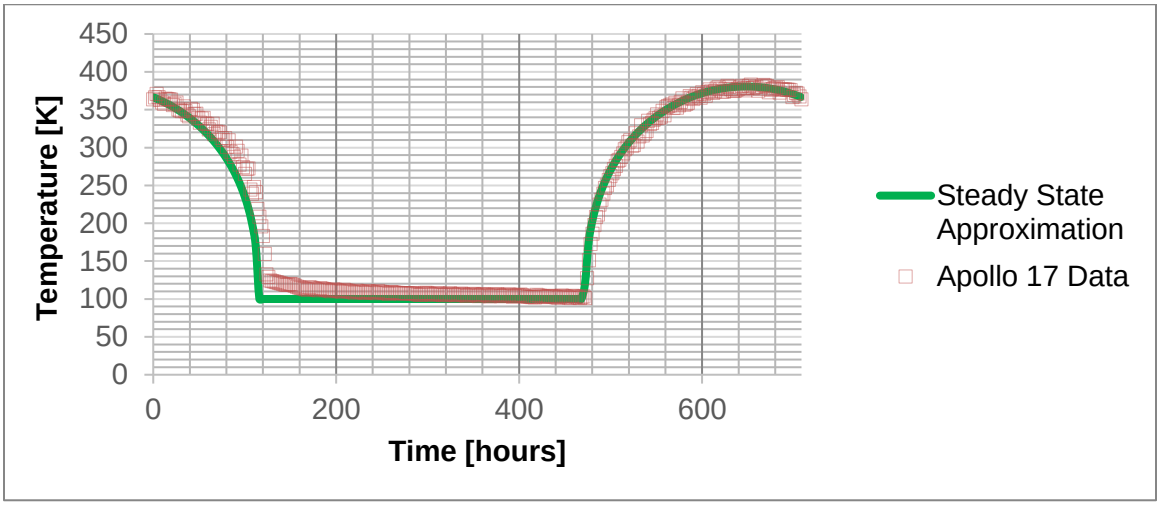

FIGURE 5.2.2-2: LUNAR SURFACE TEMPERATURES FROM APOLLO 17 MEASUREMENTS COMPARED TO THOSE CALCULATED WITH THE STEADY STATE APPROXIMATION (USING 100K AT NIGHT).

[1] D. Maslanka, "Introduction to Solar Geometry." Math 119 Illinois Institute of Technology Class Handout, 2018.

5.3 SUBSURFACE TEMPERATURE

Since the lunar regolith is a poor thermal conductor, large temperature gradients exist between the lunar surface and regolith several meters deep. Subsurface temperatures, like surface temperatures, are also site specific and can be impacted by both surface features and visiting vehicles. This section discusses subsurface temperature obtained from direct measurements or derived from measured data. Section 9.0 discusses how to build thermal models to predict subsurface temperatures.

5.3.1 Apollo and Derived LRO Measurements

Lunar subsurface temperatures have been measured at the Apollo 15 and 17 landing sites. Within the first 3.5cm regolith temperatures varied as much as 100K per month [1,2]. However, diurnal variations in incident radiation are not visible 0.8m beneath the surface [2]. At 1m to 1.5m temperatures are unaffected by both diurnal and seasonal variations and remain constant at 250.7 K (Apollo 15, 0.97deep) and 255K (Apollo 17, 1.3m deep) [3].

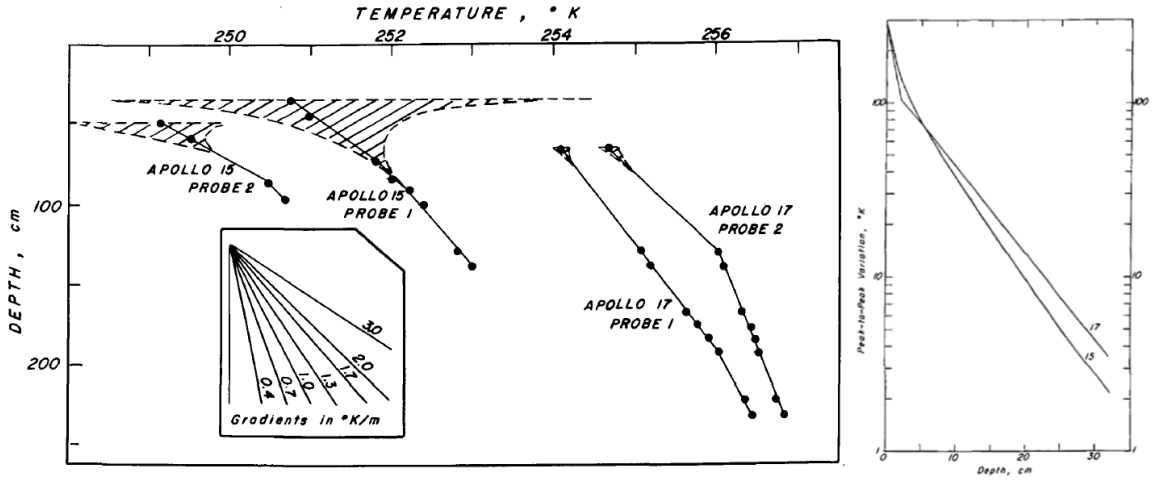

FIGURE 5.3.1-1: LUNAR SUBSURFACE TEMPERATURES (LEFT) AND MAXIMUM MONTHLY CHANGES IN TEMPERATURE VS DEPTH (RIGHT) FROM LANGSETH'S "IN-SITU MEASUREMENTS OF LUNAR HEAT FLOW".

Recently, combined infrared radiation measured by the LRO's Diviner Lunar Radiometer Experiment and microwave radiation measured by radiometers on Chang'E 1 (CE-1) and Chang'E 2 (CE-2) have been used to reproduce the Apollo subsurface temperatures and predict subsurface temperatures in additional locations [4,5,6]. The advantage of combining both data sets is that the Diviner can sense wavelengths from up to 2mm deep, while CE-1 and CE-2 can sense microwaves from up to 5m deep [4,5]. At a high level, these approaches use a 1D thermal model that provides inputs (e.g. temperatures and properties) to a 1D microwave radiative transfer model of the surface. Model parameters are then adjusted to produce measured surface temperatures and microwave emissions (which depend on subsurface temperatures) [4-7]. Wei et al. 2016 has published predicted temperature profiles for Cabeus, Haworth, and Shoemaker craters as well as the LCROSS impact site [5]. At 1.5m deep diurnal variations are <1K and were predicted to be between 41K and 42K [5].

[1] M. B. K. Langseth, "In-situ measurements of lunar heat flow," 1977.

[2] M. G. Langseth, S. J. Keihm, and K. Peters, "Revised lunar heat-flow values.," *Lunar and Planetary Science Conference Proceedings*, vol. 3, p. 3143, Apr. 1976.

[3] S. Nagihara, W. S. Kiefer, P. T. Taylor, D. R. Williams, and Y. Nakamura, "Examination of the Long-Term Subsurface Warming Observed at the Apollo 15 and 17 Sites Utilizing the Newly Restored Heat Flow Experiment Data From 1975 to 1977," *Journal of Geophysical Research: Planets*, vol. 123, no. 5, pp. 1125–1139, 2018.

[4] W. Zhang, "Lunar subsurface temperature profile modelling based on CE-1 and CE-2," *OGS / Bollettino di Geofisica Teoricae Applicata*, vol. 60, p. 489-516, Sep. 2019.

[5] G. Wei, X. Li, and S. Wang, "Thermal behavior of regolith at cold traps on the Moon′ s south pole: Revealed by Chang′E-2 microwave radiometer data," *Planetary and Space Science*, vol. 122, pp. 101–109, Mar. 2016.

[6] G. Wei, X. Li, and S. Wang, "Inversions of subsurface temperature and thermal diffusivity on the Moon based on high frequency of Chang'E-1 microwave radiometer data," *Icarus*, vol. 275, pp. 97–106, Sep. 2016.

[7]J. Feng, M. A. Siegler, P. O. Hayne, and D. T. Blewett, "Lunar Regolith Properties Constrained by LRO Diviner and Chang'e-2 Microwave Radiometer Data," presented at the Lunar and Planetary Science Conference, 2019, vol. 50, p. 3176.

5.4 GROUND HEAT FLOW

Ground heat flow is an important parameter for predicting lunar surface and subsurface temperatures. Langseth et al. calculated subsurface heat flows, given in Table 5.4-1, within the upper ~2m of lunar regolith at the Apollo 15 and 17 landing sites [1, 2]. The greater amount of the radioisotope thorium in the Hadley Rille region contributes to its higher ground heat flux [2,7].

Since the Hadley Rille and Taurus-Littrow have a higher thorium content than most regions on the Moon, their heat fluxes are not globally applicable [3]. Langseth et al. estimated a global average heat flux, assuming the subsurface heat flux equaled heat produced by radioisotopes beneath the Moon's surface. More recent calculations of subsurface heat fluxes in several presently shadowed craters on the Moon's surface, given in Table 5.4-1. These values are calculated using data from both LRO's Diviner radiometer experiment and Chang'E's microwave radiometer. Additional work to develop global heat flux maps is ongoing [4-7].

Table 5.4-1: Heat flow estimates for different locations on the Moon's surface

Region	Q [W/(m^{2}K)]	Derived from	Reference
Hadley Rille	0.021	Apollo 15 heat probe data	[1-2]
Taurus-Littrow	0.016	Apollo 17 heat probe data	[1-2]
Global average	0.018	Adjusted from Apollo 15 and 17 values based on estimated concentrations of subsurface K, U, and Tr	[1-2]
Cabeus & Haworth Crater	0.0112	Chang'E-2 microwave radiometer data	[4]
Shoemaker Crater	0.0074	Chang'E-2 microwave radiometer data	[4]
LCROSS impact site (49.6W, 84.7S)	0.01	Chang'E-2 microwave radiometer data	[4]
Lunar S. Pole	0.009	Chang'E-2 microwave radiometer data and LRO Diviner data	[6]

Perpetually Shaded Regions (PSRs) of the lunar polar craters may experience non-negligible thermal radiation and reflected solar radiance from the Earth relative to the ground heat flow.

Peak broadband earthshine may exceed 150 mW/m^2 for localized regions [5]. Additional details are contained in Section 11.1 of this document.

[1]M. Langseth, S. Keihm, and J. Chute Jr., “Heat-flow experiment. In Apollo 17 Preliminary Science Report.,” NASA SP-330.

[2] M. G. Langseth, S. J. Keihm, and K. Peters, “Revised lunar heat-flow values.,” Lunar and Planetary Science Conference Proceedings, vol. 3, p. 3143, Apr. 1976.

[3] M. Siegler and D. Paige, “Lunar Global Heat Flow: Predictions and Constraints,” presented at the Lunar Science for Landed Missions Workshop, NASA Ames, 2018.

[4] G. Wei, X. Li, and S. Wang, “Thermal behavior of regolith at cold traps on the Moon′s south pole: Revealed by Chang′E-2 microwave radiometer data,” Planetary and Space Science, vol. 122, pp. 101–109, Mar. 2016.

[5] David A. Glenar, et. al., “Earthshine as an Illumination Source at the Moon”, Icarus, Volume 321, p. 841-856, March 2019.

[6] J. Feng, M. Siegler, and P. Hayne, “2786.pdf,” presented at the 51st Lunar and Planetary Science Conference, 2020, Accessed: Apr. 28, 2020. [Online]. Available: https://www.hou.usra.edu/meetings/lpsc2020/pdf/2786.pdf.

[7] D. A. Paige and M. A. Siegler, “New Constraints on Lunar Heat Flow Rates from LRO Diviner Lunar Radiometer Experiment Polar Observations,” vol. 47, p. 2753, Mar. 2016.

6.0 THERMO-PHYSICAL PROPERTIES OF LUNAR REGOLITH

The following sections provide background information to the DSNE specification for the bulk thermo-physical properties (thermal conductivity, specific heat, density and thermal diffusivity) of lunar regolith. Much of the thermo-physical property data in both the DSNE and the following sections is derived from Apollo return samples, the Apollo Lunar Surface Experiments Package (ALSEP) and LRO Diviner measurements. In the event of any conflict, DSNE specification takes precedence over this document.

6.1 BULK THERMAL CONDUCTIVITY

DSNE 3.4.6.2.1 provides relationships for bulk in-situ thermal conductivity of lunar regolith. The theory behind these relationships is described below.

The thermal conductivity of bulk regolith at >100 K and in vacuum (< ~0.075 torr [12]) can be modeled assuming heat flows through the regolith by conduction and radiation heat transfer in parallel. . This model is given by Watson’s equation [1 – 4]:

$$k(T) = k_C + k_r T^3$$

where k_C is the grain thermal conductivity (also called solid phonon conductivity) and $k_r T^3$ is the effective conductivity from radiation. Effective conductivity from radiation equals distance times net heat radiation heat transfer over ΔT, and is therefore a function of T^3 [1]. Often k_r is modeled as $k_C \chi / 350^3$, where $\chi = k_r T^3 / k_C$ at 350 K.

Constants k_C and k_r depend on density and material composition, which vary with depth and location on the lunar surface. Table 6.1-1, shows the constants for Apollo samples calculated from tests conducted between ~100 K to ~400 K. Thermal conductivity vs depth profiles, down to 14cm, were derived based on data from the Apollo 15 and 17 heat flow experiments and are provided by Langseth 1977 [10].

TABLE 6.1-1: WATSON'S EQUATION FOR RETURNED APOLLO SAMPLES.

Mission	Area	Density [kg/m^3]	k_C [W/(mK)]	k_r [W/(mK^4)]	Ref.
Apollo 11	Mare	1300	1.425E-03	1.72E-11	[4]
Apollo 11	Mare	1640	1.868E-03	2.29E-11	[4]
Apollo 11	Mare	1950	1.793E-03	1.47E-11	[4]
Apollo 12	Mare	1300	9.220E-04	3.19E-11	[5]
Apollo 12	Mare	1970	1.150E-03	1.59E-11	[6]
Apollo 14	Highland	1100	8.360E-04	2.09E-11	[7]
Apollo 14	Highland	1300	6.190E-04	2.49E-11	[7]
Apollo 15	Mare/Highland	1300	6.246E-04	1.192E-11	[8]
Apollo 16	Highland	1500	4.840E-04	1.10E-11	[9]

Since the Apollo values are site specific, Hayne et al. 2017 derived the following relationships for the Watson's equation constants by best matching a 1D thermal model of the Moon's surface to global data from the LRO Diviner experiment [11].

$k_r = k_C \left(\frac{2.7}{350^3}\right) \left[\frac{W}{mK^4}\right]$ (Note: [16] suggests tentatively updating this to $k_C \left(\frac{1.8}{350^3}\right)$)

$k_C = k_{deep\ layer} - \left(k_{surface\ layer} - k_{deep\ layer}\right)\left(\frac{\rho_{deep\ layer} - \rho}{\rho_{deep\ layer} - \rho_{surface\ layer}}\right) \left[\frac{W}{mK}\right]$

$k_{surface\ layer} = 8.0 \times 10^{-4} \left[\frac{W}{mK}\right]$, $k_{deep\ layer} = 3.8 \times 10^{-3} \left[\frac{W}{mK}\right]$ [1]

$\rho_{surface\ layer} = 1100 \left[\frac{kg}{m^3}\right]$, $\rho_{deep\ layer} = 1800 \left[\frac{kg}{m^3}\right]$

$\rho = \rho_{deep\ layer} - \left(\rho_{deep\ layer} - \rho_{surface}\right)e^{-\frac{z}{H}} \left[\frac{kg}{m^3}\right]$

z = depth (from surface) [m]

H = H-parameter, a location dependent scaling factor that controls how density increases with depth.

Hayne provides a color map that gives H based on location for ±70°LAT. The average value for ±60°LAT is 0.068m with a standard deviation of 0.0007m.

Below 100K, k_C can no longer be accurately treated as temperature independent and the temperature dependence of k_C depends on the particle's crystal structure [2]. Recently, Woods-

[1] These are the updated constants provided by Feng et al. [17]

Robinson et al. 2019 presented a new physical model for bulk thermal conductivity along with coefficients fitted to laboratory data for the lunar simulant crushed basalt.

$$k(T,\rho,p) = AT^3 + (B + C\rho^2)(1-p)k_{am}$$

$$k_{am} = A_{am} + B_{am}T^{-4} + C_{am}T^{-3} + D_{am}T^{-2} + E_{am}T^{-1} + F_{am}T + G_{am}T^2 + H_{am}T^3 + I_{am}T^4$$

TABLE 6.1-2: COEFFICIENTS FOR BULK K OF CRUSHED BASALT

A_{am}	-2.03297E-01	A	1.30E-11
B_{am}	-11.472	B	9.90E-04
C_{am}	22.5793	C	9.20E-10
D_{am}	-14.3084		
E_{am}	3.41742		
F_{am}	0.011011		
G_{am}	-2.80491E-05		
H_{am}	3.35837E-08		
I_{am}	-1.40021E-11		

Additionally, water ice may be to be present at specific sites on the lunar surface and subsurface constantly below 100 K [13]. The presence of ice between the grains can increase thermal conductivity grains, but exact effect on the lunar surface is unknown [14]. Reiss 2017 summarizes the most recent models for icy regolith as well as regolith was gas between the particles [15].

[1] K. Watson, “I. The thermal conductivity measurements of selected silicate powders in vacuum from 150°-350° K. II. An interpretation of the Moon’s eclipse and lunation cooling as observed through the Earth’s atmosphere from 8-14 microns,” phd, California Institute of Technology, 1964.

[2] R. Woods-Robinson, M. A. Siegler, and D. A. Paige, “A Model for the Thermophysical Properties of Lunar Regolith at Low Temperatures,” *Journal of Geophysical Research: Planets*, vol. 124, no. 7, pp. 1989–2011, 2019.

[3] J. L. Linsky, “Models of the lunar surface including temperature-dependent thermal properties,” *Icarus*, vol. 5, no. 1, pp. 606–634, Jan. 1966.

[4] C. J. Cremers, “Heat Transfer Within the Lunar Surface Layer,” in *Advances in Heat Transfer*, vol. 10, J. P. Hartnett and T. F. Irvine, Eds. Elsevier, 1974, pp. 39–83.

[5] C. J. Cremers and R. C. Birkebak, “Thermal conductivity of fines from Apollo 12,” *Lunar and Planetary Science Conference Proceedings*, vol. 2, p. 2311, 1971.

[6] C. J. Cremers, R. C. Birkebak, and J. E. White, “Thermal characteristics of the lunar surface layer,” *International Journal of Heat and Mass Transfer*, vol. 15, no. 5, pp. 1045–1055, May 1972.

[7] C. J. Cremers, “Thermal conductivity of Apollo 14 fines,” *Lunar and Planetary Science Conference Proceedings*, vol. 3, p. 2611, 1972.

[8] C. J. Cremers and H. S. Hsia, “Thermal conductivity and diffusivity of Apollo 15 fines at low density,” *Lunar and Planetary Science Conference Proceedings*, vol. 4, p. 2459, 1973.

[9] C. J. Cremers and H. S. Hsia, “Thermal conductivity of Apollo 16 lunar fines,” *Lunar and Planetary Science Conference Proceedings*, vol. 3, p. 2703, 1974.

[10]M. B. K. Langseth, “In-situ measurements of lunar heat flow,” 1977.

[11] P. O. Hayne *et al.*, “Global Regolith Thermophysical Properties of the Moon from the Diviner Lunar Radiometer Experiment: Lunar Regolith Thermophysical Properties,” *J. Geophys. Res. Planets*, vol. 122, no. 12, pp. 2371–2400, Dec. 2017.

[12]A. E. Wechsler and P. E. Glaser, “Pressure effects on postulated lunar materials,” Icarus, vol. 4, no. 4, pp. 335–352, Sep. 1965.

[13]M. Siegler, D. Paige, J.-P. Williams, and B. Bills, “Evolution of lunar polar ice stability,” Icarus, vol. 255, pp. 78–87, Jul. 2015.

[14]G. Wei, X. Li, and S. Wang, “Thermal behavior of regolith at cold traps on the Moon′s south pole: Revealed by Chang′E-2 microwave radiometer data,” Planetary and Space Science, vol. 122, pp. 101–109, Mar. 2016.

[15]P. Reiss, “In-Situ Thermal Extraction of Volatiles from Lunar Regolith,” Technical University of Munich, 2018.

[16] J. Feng, M. A. Siegler, P. O. Hayne, and D. T. Blewett, “Lunar Regolith Properties Constrained by LRO Diviner and Chang’e-2 Microwave Radiometer Data,” presented at the Lunar and Planetary Science Conference, 2019, vol. 50, p. 3176.

[17] J. Feng, M. A. Siegler, and P. O. Hayne, “New Constraints on Thermal and Dielectric Properties of Lunar Regolith from LRO Diviner and CE-2 Microwave Radiometer,” Journal of Geophysical Research: Planets, vol. 125, no. 1, p. e2019JE006130, 2020, doi: 10.1029/2019JE006130.

6.2 SPECIFIC HEAT

DSNE 3.4.6.2.2 provides the specific heat as a function of temperature for lunar regolith.

6.3 BULK DENSITY

DSNE 3.4.2.3.1 describes the bulk density of the lunar regolith and provides a curve fit of bulk density verses depth based on Apollo data from Apollo 15, 16, and 17. The Lunar Sourcebook also presents a curve fit for Apollo 15 data [1].

Additional depth verses density curves have been developed as part of recent efforts to derive equatorial [2] and global [3] thermophysical regolith properties by best fitting temperatures predicted by lunar surface models to Diviner brightness temperatures. Hayne et al.’s density equation is presented in section 6.1.

Recent research has suggested these curves predict higher densities than what will be seen in permanently shadowed craters at the lunar poles. This is because (1) permanently shadowed regions undergo much less thermal cycling than periodically sunlit terrain, and (2) experiments with lunar simulant JSC-1A have indicated that thermal cycling contributed to the lunar regolith’s increase in density with depth.

[1] G. Heiken, D. Vaniman, and B. French, Lunar sourcebook: A user's guide to the Moon. New York: Cambridge University Press, 1991.

[2] A. R. Vasavada et al., "Lunar equatorial surface temperatures and regolith properties from the Diviner Lunar Radiometer Experiment:," J. Geophys. Res., vol. 117, no. E12, p. n/a-n/a, Dec. 2012, doi: 10.1029/2011JE003987.

[3] P. O. Hayne *et al.*, "Global Regolith Thermophysical Properties of the Moon from the Diviner Lunar Radiometer Experiment: Lunar Regolith Thermophysical Properties," *J. Geophys. Res. Planets*, vol. 122, no. 12, pp. 2371–2400, Dec. 2017.

[4] P. Metzger, S. Anderson, and A. Colaprete, "Experiments Indicate Regolith is Looser in the Lunar Polar Regions than at the Lunar Landing Sites," presented at the Earth & Space 2018 Conference (ASCE), 2018.

6.4 THERMAL DIFFUSIVITY

DSNE 3.4.6.2.3 provides the description of thermal diffusivity as a function of depth of the lunar regolith based on Watson's equation [1,2] for thermal conductivity with the grain thermal conductivity and the effective conductivity from radiation supplied by Langseth and Keihm [3]. Plots of the thermal diffusivity for regolith depths both less than and greater than 2 cm are provided in Figure 6.4-1 for a constant density of 1580 kg/m^3. The thermal diffusivity is calculated from $k/(\rho c_p)$ with the temperature dependent specific heat from DSNE 3.4.6.2.2.

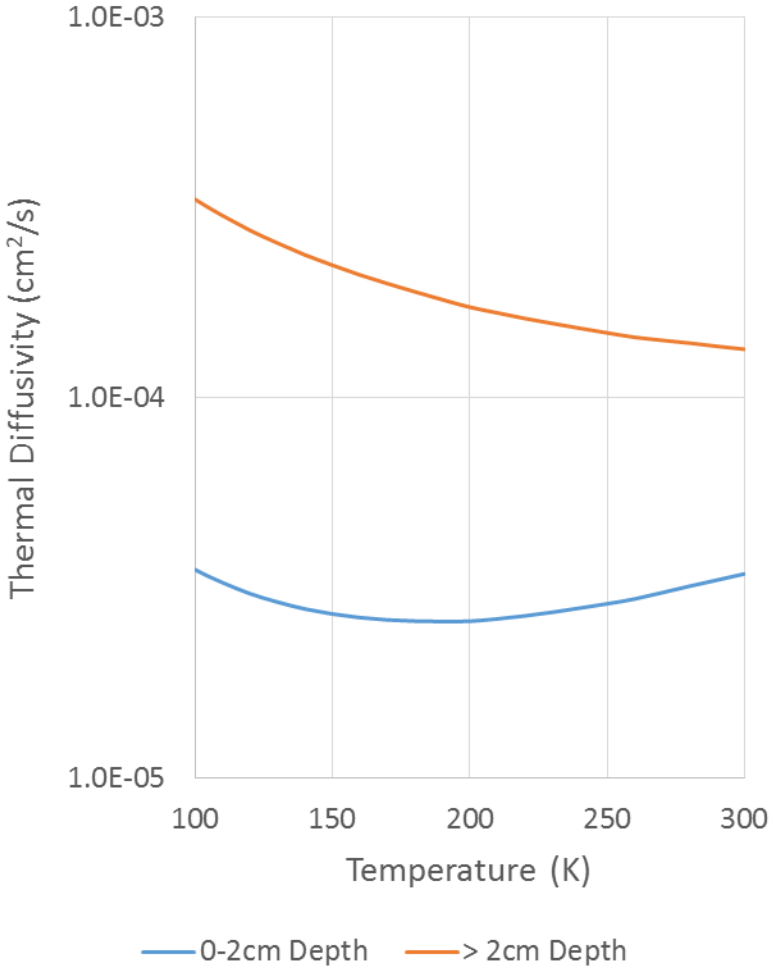

FIGURE 6.4-1: THERMAL DIFFUSIVITY OF LUNAR REGOLITH

Thermal diffusivity versus depth is shown in Figure 6.4-2 for three different temperatures. The thermal diffusivity is calculated from $k/(\rho c_p)$ with the thermal conductivity and density versus depth described by Hayne [4] (see Section 6.1 from this document) and the specific heat from DSNE 3.4.6.2.2 as before.

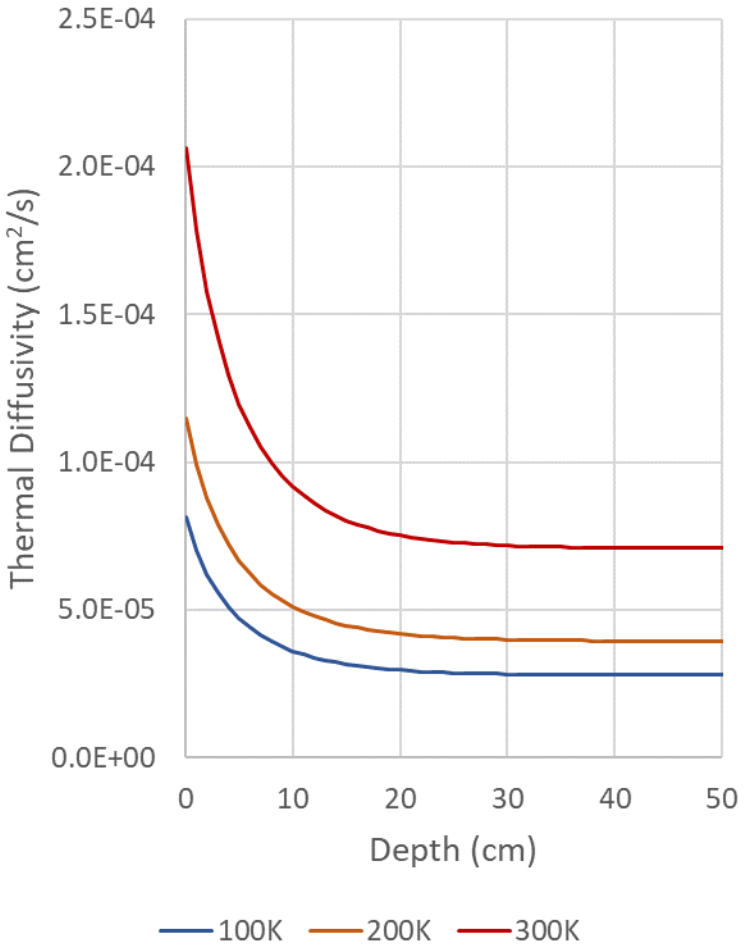

FIGURE 6.4-2: THERMAL DIFFUSIVITY OF LUNAR REGOLITH VERSUS DEPTH AND TEMPERATURE

[1] K. Watson, “I. The thermal conductivity measurements of selected silicate powders in vacuum from 150°-350° K. II. An interpretation of the Moon’s eclipse and lunation cooling as observed through the Earth’s atmosphere from 8-14 microns,” phd, California Institute of Technology, 1964.

[2] R. Woods-Robinson, M. A. Siegler, and D. A. Paige, “A Model for the Thermophysical Properties of Lunar Regolith at Low Temperatures,” *Journal of Geophysical Research: Planets*, vol. 124, no. 7, pp. 1989–2011, 2019.

[3] M.G. Langseth Jr., S.J. Keihm, and J.L. Chute Jr. (1973) “Heat-flow experiment. In Apollo 17

Preliminary Science Report”, *NASA SP-330*, pp. 9-1 to 9-24, 1973.

[4] P. O. Hayne *et al.*, “Global Regolith Thermophysical Properties of the Moon from the Diviner Lunar Radiometer Experiment: Lunar Regolith Thermophysical Properties,” *J. Geophys. Res. Planets*, vol. 122, no. 12, pp. 2371–2400, Dec. 2017.

7.0 OPTICAL PROPERTIES OF LUNAR REGOLITH

The distribution of electromagnetic radiation according to wavelength is known as the electromagnetic spectrum as shown in Figure 7.0-1 [1]. The spectrum is sub-divided into multiple bands based on differences in behavior. Of particular interest in radiation heat transfer is the "Thermal Radiation" band of the electromagnetic spectrum between 0.1 and 100 microns in wavelength. Outside of the thermal waveband, electromagnetic energy generally passes through objects or has very little heat energy (based on temperature) under practical conditions. Wavelengths beyond 100 microns may be of interest in measuring extremely low temperatures such as the far side of the Moon or perpetually shadowed craters. An object at a given temperature will emit energy over a spectrum of wavelengths. The Sun can be approximated as a black body with a temperature of 5800 K (10000°F). Thermal analyses are typically conducted using a two waveband absorptance model which subdivides the thermal energy spectrum into solar (< 3.0 μm) and infrared (>3.0 μm) wavelengths.

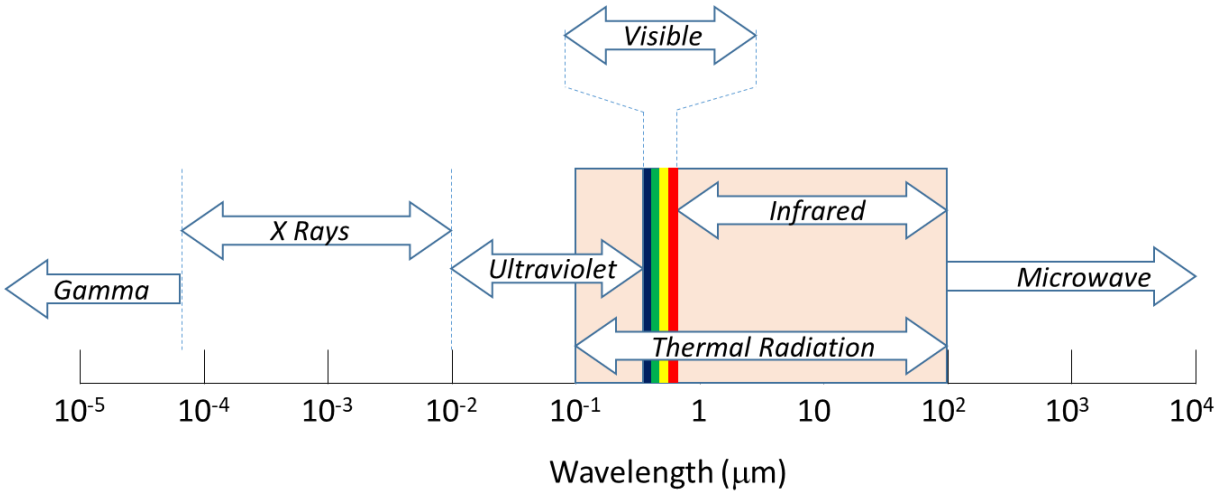

Figure 7.0-1: Electromagnetic Spectrum

Planck's law [2] describes the monochromatic emissive power of a black body at temperature T and wavelength λ into a vacuum where $C_1=2\pi hc^2$ and $C_2= hc/k$ and h, c and k are the Planck constant, speed of light and the Boltzmann constant respectively.

$$E_b(T,\lambda) = \frac{C_1}{\lambda^5\left(\exp\left(\frac{C_2}{\lambda T}\right)-1\right)}$$

The normalized spectral irradiance for environmental sources in a lunar application are shown in Figure 7.0-2. The normalized curves are derived by dividing by the black body emissive power from Planck's law by the maximum emissive power derived from Wien's law described by $\lambda T=b$ [3]. In order to parse the various wavebands, normalized spectral distributions are shown for the Sun, Lunar surface at noon (393K) and at midnight (90K) and a typical thermal control surface (293K). The overlapping wavebands between the lunar background at noon and a conventional thermal radiating surface illustrates the difficulty of rejecting heat during the lunar day.

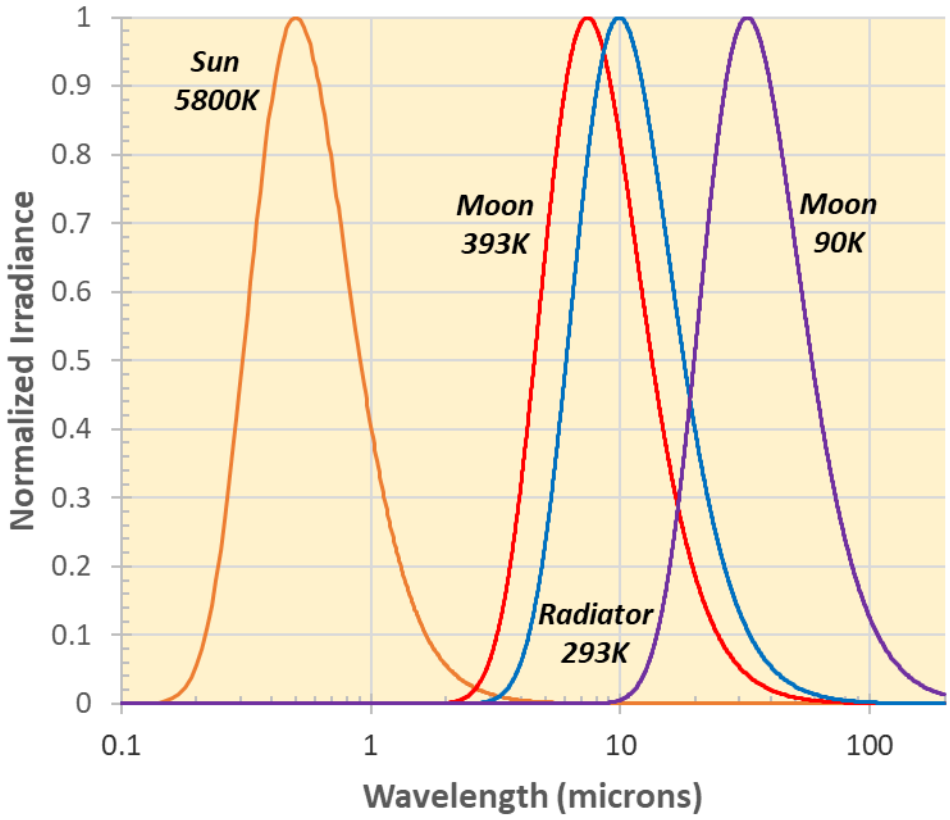

FIGURE 7.0-2: SOLAR, LUNAR AND THERMAL RADIATOR IRRADIANCE

7.1 SOLAR ABSORPTIVITY/ALBEDO

DSNE 3.4.6.1.1 describes the albedo of the lunar surface. For orbital calculations the material in DSNE 3.3.9.1.2 may be used. The DSNE specifications for minimum and maximum albedo take precedence but, if needed for a specific application, directional albedos are contained in the following section.

Albedo is the fraction of incident light or radiation reflected by a surface and may be defined in several different ways. ***Normal albedo*** is the reflectance of a surface when both viewed and illuminated in the local vertical direction (i.e. normal to the surface). ***Directional hemispherical albedo*** is the reflectance in all directions resulting from direct illumination from a specific direction. ***Total hemispherical albedo*** is the reflectance in all viewing directions integrated over all phase angles.

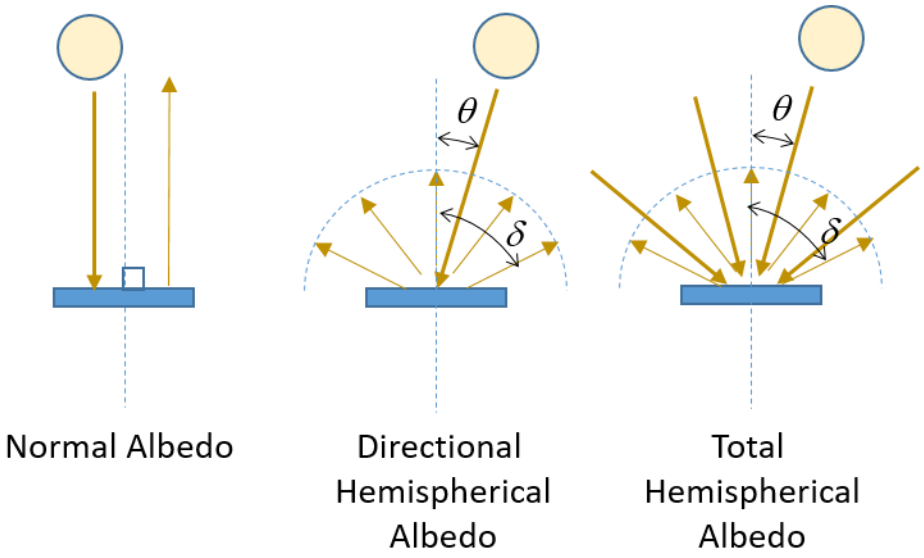

FIGURE 7.1-1: ALBEDO DEFINITIONS

Bolometric albedos are obtained by integrating the wavelength dependent albedo over the waveband of interest as illustrated below for the lunar surface normal and hemispherical albedos. A bolometric normal or hemispherical albedo would be averaged against the solar spectrum represented as a black body radiating at 5800K.

$$\overline{A_\perp} = \frac{\int_0^\infty A_\perp(\lambda)\, E_b(T,\lambda) d\lambda}{\sigma T^4}$$

$$A_\frown(\theta) = \frac{\int_0^\infty \left(\int_0^\delta A_\frown(\lambda,\theta,\delta) d\delta \right) E_b(T,\lambda) d\lambda}{\sigma T^4}$$

$$\overline{A_\frown} = \int_0^{\pi/2} A_\frown(\theta) d\theta$$

Dollfus and Bowell [3] derived the normal albedo from telescopic observations of the near side lunar surface. The measurements were made and averaged for 14 different regions over a wavelength range of 0.327μ to 1.05μ. The following relation was derived to fit the normal albedo to the observations.

$$A_\perp(\lambda) = 10^{0.83\log(\lambda) - 0.80}$$

Since the observed waveband does not include the entire solar spectrum, the normal wavelength dependent albedo is integrated against the truncated waveband to obtain the bolometric normal albedo as shown below.

$$\overline{A_\perp} = \frac{\int_{\lambda_1}^{\lambda_2} A_\perp(\lambda)\, E_b(T,\lambda) d\lambda}{\int_{\lambda_1}^{\lambda_2} E_b(T,\lambda) d\lambda} \sim 0.12$$

The bolometric normal albedo is recommended for orbital calculations involving a radiatively participating lunar surface as described in DSNE 3.3.9.1.2.

For detailed thermal modeling of the lunar surface temperature, a solar incident angle albedo obtained from direct measurement of Apollo Sample Fines [4] or correlations based on lunar surface temperature by a number of authors including Keihm [5], Williams [6], Vasvada [7], Hayne [8] or Feng [9] may be needed.

Birkebak [4] illuminated a lunar sample by shining a light onto a diffusely reflecting sphere containing a 25mm diameter sample of Apollo Lunar Fines and measured the radiance originating from both the sample and the sphere wall at a desired angle as shown in Figure 7.1-2. The ratio of the sample to sphere radiance is the reflectance. The radiance from the sphere (onto the sample) should be isotropic. By reciprocity, this method should be identical to shooting a collimated light onto the one side of the sample and then measuring the radiance to obtain directional hemispheric reflectance (or albedo) as described above. Birkebak's results for directional reflectance for Apollo samples of varying densities are shown in the Table 7.1-1.

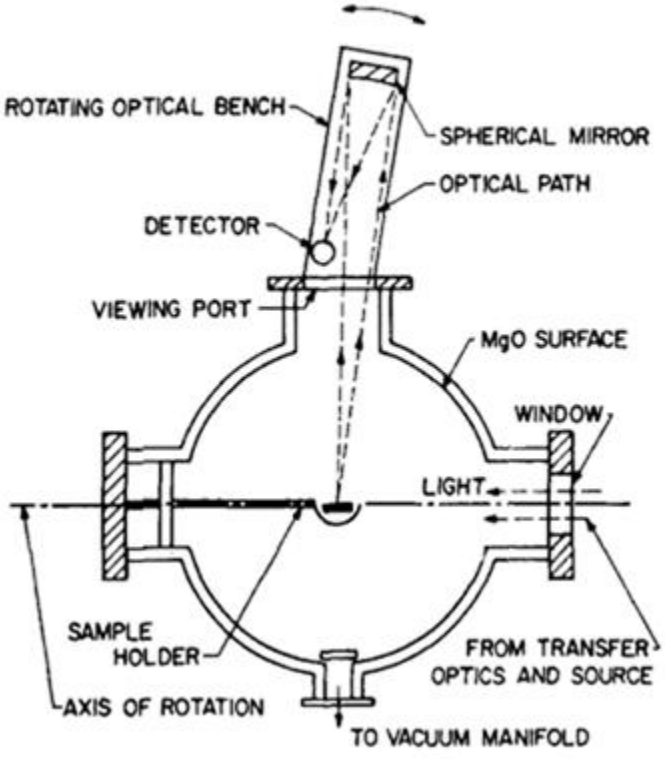

FIGURE 7.1-2: SCHEMATIC OF INTEGRATING SPHERE FOR APOLLO MEASUREMENTS

TABLE 7.1-1 APOLLO DIRECTIONAL REFLECTANCE

	Apollo 11				Apollo 12			Apollo 14		
Angle to normal, deg	1300 kg/m^3	1400 kg/m^3	1600 kg/m^3	1800 kg/m^3	1300 kg/m^3	1600 kg/m^3	1800 kg/m^3	1095 kg/m^3	1300 kg/m^3	1590 kg/m^3
0	0.08	0.09	0.10	0.10	0.10	0.12	0.12	0.18	0.21	0.21
10	0.07	0.08	0.10	0.09	0.10	0.12	0.12	0.18	0.21	0.22
20	0.08	0.10	0.11	0.11	0.11	0.12	0.13	0.18	0.21	0.21
30	0.09	0.11	0.11	0.11	0.11	0.11	0.13	0.19	0.22	0.22
40	0.09	0.11	0.11	0.11	0.11	0.12	0.13	0.21	0.23	0.25
50	0.08	0.11	0.11	0.11	0.14	0.16	0.15	0.22	0.25	0.27
60	0.11	0.14	0.14	0.14	0.20	0.23	0.20	0.25	0.28	0.30
70	0.22	0.25	0.25	0.24	0.33	0.38	0.32	0.33	0.36	0.35
80	0.49	0.52	0.51	0.50	0.58	0.62	0.57	0.53	0.57	0.52
85	0.71	0.73	0.72	0.72	0.77	0.79	0.76	0.72	0.75	0.71
90	1.00	1.02	1.00	1.00	1.00	1.00	1.00	1.00	1.00	1.00

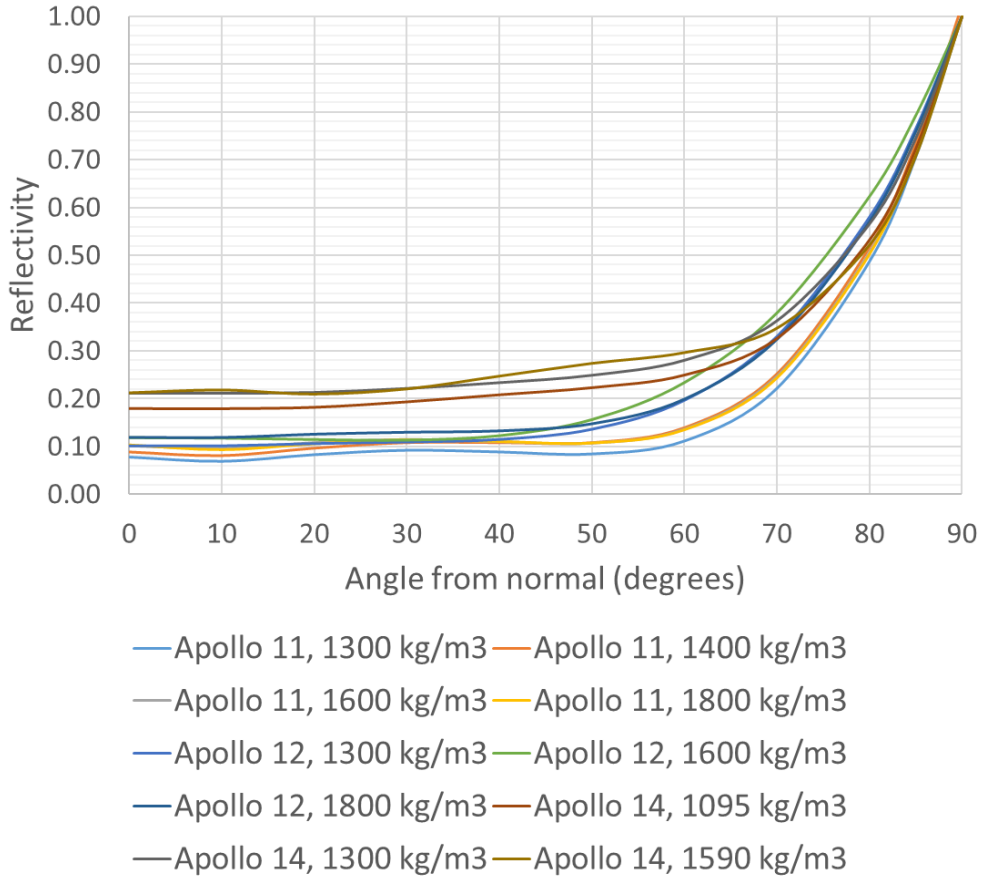

FIGURE 7.1-3: REFLECTIVITY OF APOLLO SAMPLES

The solar absorptance is obtained via Kirchoff's law:

$$\alpha(\theta) = 1 - A_{\frown}(\theta)$$

A comparison of the solar absorptance versus incident angle is shown in Figure 7.1-4 for the Apollo measurements.

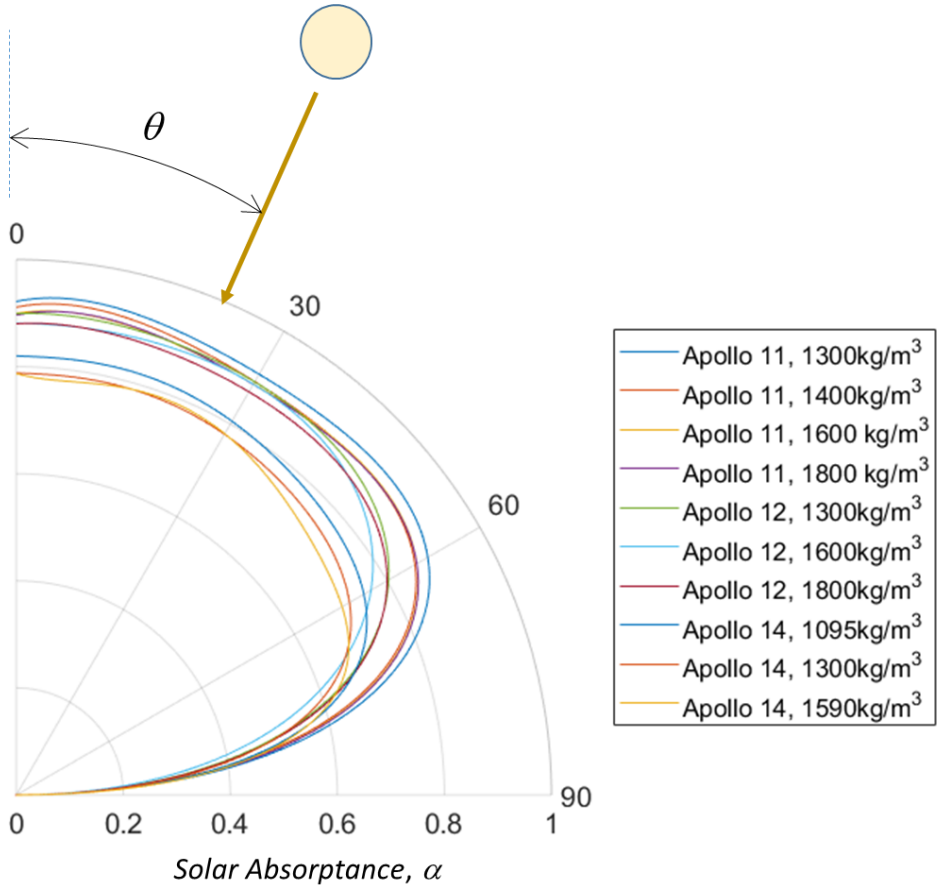

FIGURE 7.1-4: LUNAR SOLAR ABSORPTANCE VERSUS LATITUDE FROM APOLLO MEASUREMENTS

Keihm [5] proposed that the variation of albedo increases with incidence angle according to the function:

$$A_{\frown}(\theta) = A_O + a\left(\frac{\theta}{45}\right)^3 + b\left(\frac{\theta}{90}\right)^8$$

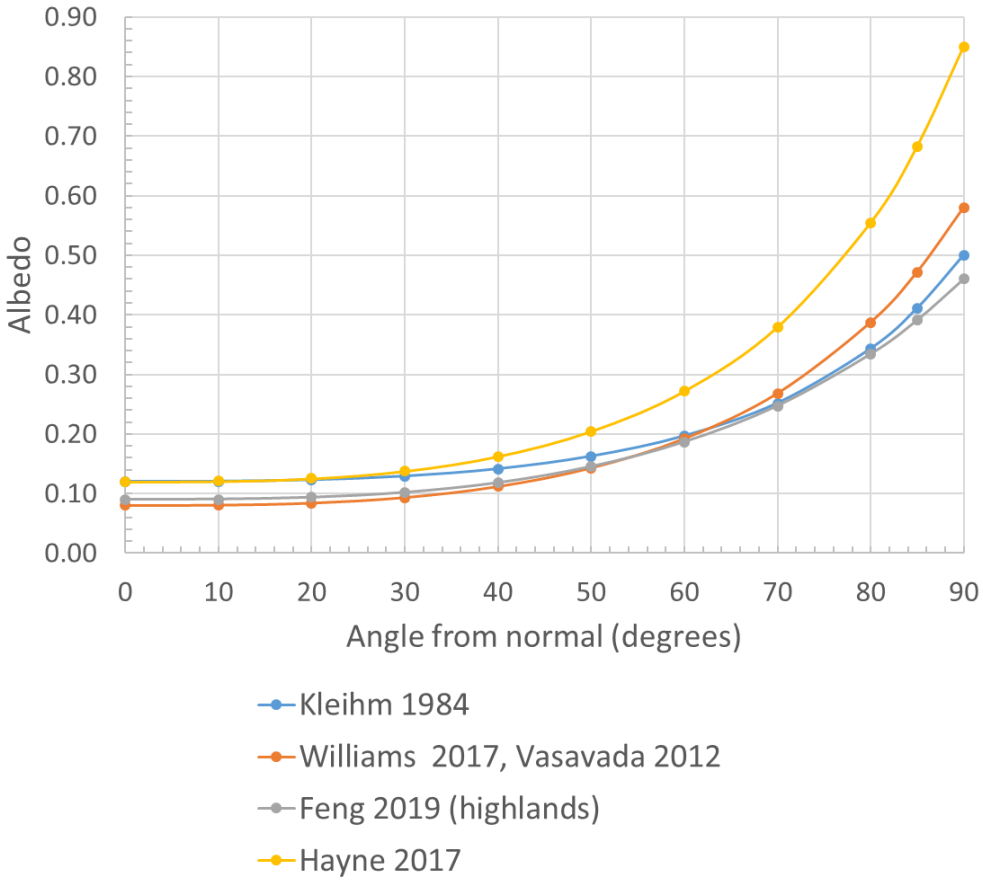

FIGURE 7.1-5: DIRECTIONAL ALBEDO FITS FROM VARIOUS LUNAR SURFACE MODELS

A comparison between Keihm [5], Williams [6] & Vasavada [7], Hayne [8] and Feng [9] is provided in Figure 7.1-6.

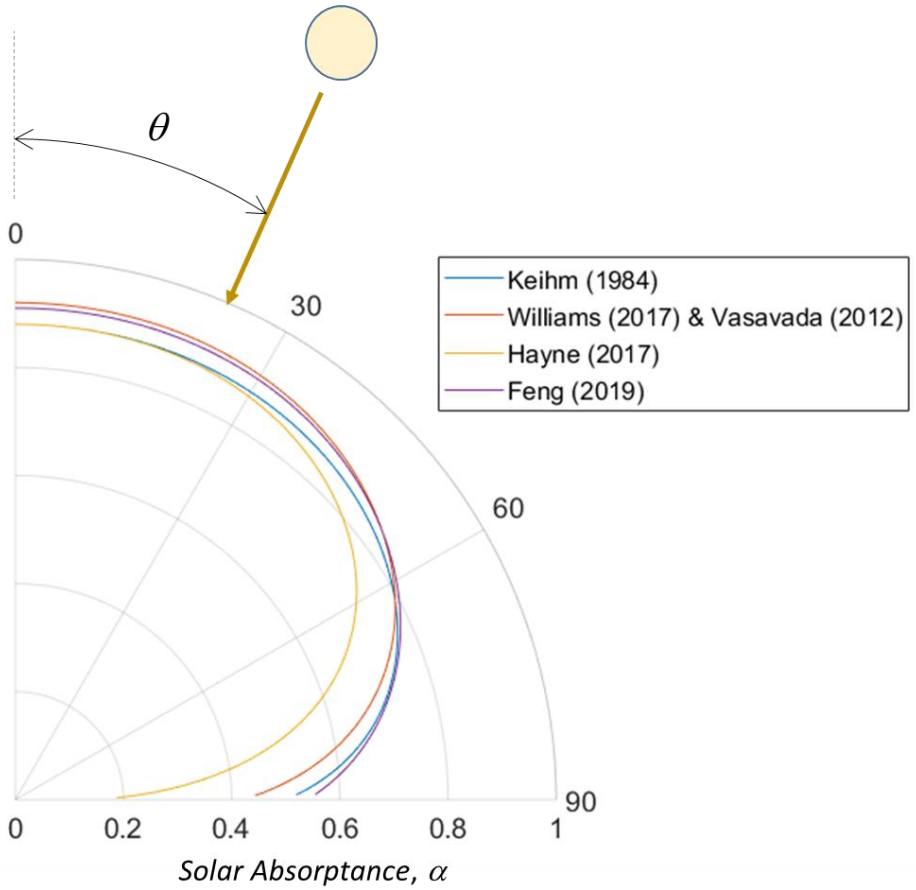

FIGURE 7.1-6: LUNAR SOLAR ABSORPTANCE VERSUS INCIDENCE ANGLE FROM LUNAR SURFACE MODELS

7.2 INFRARED EMITTANCE

The infrared emittance of the lunar regolith for mare and highland regions is described in DSNE 3.4.6.1.1.

7.3 LIGHT SCATTER/SPECULARITY OF LUNAR REGOLITH

Light scattering properties (Henyey-Greenstein phase function) of the lunar regolith are described in DSNE 3.4.5. If the higher fidelity Hapke scattering function is needed, it is described in Sato et al., 2014. An example application is also provided in Appendix G of this document.

[1] Bertrand Baudouy, “Heat Transfer and Cooling Techniques at Low Temperature”, *CEA Saclay, France*, January 2015.

[2] Max Planck, “The Theory of Heat Radiation”, P. Blakiston’s Son and Co., Philadephia, 1914, pages 86 and168.

[3] A Dollfus and E. Bowell, “Polarimetric Properties of the Lunar Surface and its Interpretation”, Astronomy and Astrophysics 10, 29-53, 1971.

[4] Richard C. Birkebak, “Thermophysical Properties of Lunar Materials: Part I Thermal Radiation Properties of Lunar Materials from the Apollo Missions”, Advances in Heat Transfer, Vol. 10, Academic Press, 1974.

[5] Stephen J. Keihm, “Interpretation of the Lunar Microwave Brightness Temperature Spectrum: Feasibility of Orbital Heat Flow Mapping”, Icarus 60, p. 568-589, 1984.

[6] J. P. Williams et al, “The Global Surface Temperatures of the Moon as Measured by the Diviner Lunar Radiometer Experiment”, Icarus, Elsevier, 2016.

[7] Ashwin R. Vasavada, et al, “Lunar equatorial surface temperatures and regolith properties from the Diviner Lunar Radiometer Experiment”, JOURNAL OF GEOPHYSICAL RESEARCH, VOL. 117, 2012.

[8] Paul O. Hayne, et al, “Global regolith thermophysical properties of the Moon from the Diviner Lunar Radiometer Experiment”, 2017.

[9] J. Feng, M. A. Siegler, P. O. Hayne, and D. T. Blewett, “Lunar Regolith Properties Constrained by LRO Diviner and Chang’e-2 Microwave Radiometer Data,” presented at the Lunar and Planetary Science Conference, 2019, vol. 50, p. 3176.

8.0 LUNAR ORBIT MODELING GUIDELINES/APPROACHES

The Lunar Orbit Modeling approach in this document is tailored to the HLS program, but is applicable to any space system in orbit about the Moon such as Gateway, Catalyst and others. Of particular concern to HLS are the NRHO utilized by Gateway, Low Lunar Orbits used to stage to and from the lunar surface, as well as detailed analysis of the descent and ascent trajectories.

Space systems have complex geometries and are flown in a multitude of orientations for communication, docking, and other mission objectives. The vehicle, subsystems, or individual components, may not respond similarly to a given set of imposed environments and orientations. It is recommended for Lunar Orbit modeling to analyze a sweep of expected Beta angles and vehicle orientations to understand systems and component sensitivities and responses and to develop a set of known vehicle specific worst case analyses.

The Solar and Lunar thermal environments have been addressed in previous sections of this document. This section will focus on defining the particular orbits of each mission phase.

8.1 NEAR RECTILINEAR HALO ORBIT (NRHO)

8.1.1 Description

Much of the definition of the NRHO is taken from “NASA White Paper, Gateway Destination Orbit Model: A Continuous 15 Year NRHO Reference Trajectory” [1]. This Orbit is discussed in the “Gateway Integrated Thermal Model Development Document IAC4r0” [2].

All the orbits being considered for Gateway are classified as L2 Halo Orbits. These use the unique gravity field around the Moon and L2 Lagrange Point to greatly reduce the amount of fuel required

to remain in orbit. The preferred Gateway orbit is the NRHO with the 9:2 NRHO very likely being chosen for its near polar Earth-Moon orientation, offering constant communication and avoidance of solar eclipses by the Earth. In a 9:2 NRHO, the spacecraft will make 9 orbits during 2 lunar months. The NRHO uses the gravitational fields of both the Earth and the Moon to maintain this orbit, rather than orbiting a single body [1].

Since the Moon and Orbit are both fixed (tidally locked) with respect to Earth, a spacecraft's longitude will always be near 90° and 270°. The beta angle of the orbit varies throughout the year between -90° and +90°. This orbit has an average perilune radius of 3366km with an average orbital period of 6.562 days [1].

8.1.2 Modeling Approach

8.1.2.1 Sun/Planet Vector Lists

To model the non-Keplerian NRHO orbit within an analysis tool like Thermal Desktop, a Sun/Planet/Radius Vector list describing an as-flown NRHO can be used to analyze thermal performance in an NRHO. For JSC Gateway analysis, orbital Sun/Planet/Radius vector lists were created from Guidance, Navigation, and Control (GN&C) provided data of Gateway's orbit around the Moon to define an orbital heating environment corresponding to the worst-case cold and worst-case hot environments experienced by Gateway. Fifteen years' worth of orbit data was received from GN&C that included an Epoch, solar beta angle, solar and planetary vectors, altitude, and true anomaly in increments of +1° true anomaly for the entire fifteen year period.

This data can be filtered to a manageable number of orbital positions with a higher concentration nearer periapsis. Once the spacecraft is beyond the thermal influence of the Moon's surface (>10 mean lunar radii), a single point in space can be used to generate environments until the next lunar pass.

For spacecraft analysis in proximity or docked to Gateway, it would be useful to utilize the orbit definitions, orientation constraints, and spacecraft environmental influences and shading included with the Gateway Integrated Thermal Model IAC4r0 [2]. For example, when docked at Gateway, the Orion spacecraft is constrained in a tail-to-Sun orientation which also constrains Gateway and any other docked spacecraft.

8.1.2.2 Keplerian Approximation

An NRHO is non-Keplerian and cannot be exactly modeled as an ellipse. However, vector lists are constrained by epoch and do not necessarily produce driving environment sets. A Keplerian orbit may be used to approximate an NRHO and closely match the orbital environments on the spacecraft. Using the Keplerian orbit provides the analyst with many advantages such as a visualization of the orbit and control over the orbital parameters such as beta angle and solar declination angle to create enveloping hot and cold orbital environments. Figure 8.1.2.2-1 shows an NRHO Vector list (orange) and Keplerian Ellipse (blue) in proximity of the Moon. Because the NRHO is not planar, a side view perpendicular to the Earth-Moon line of centers is shown. Each point on the lines represents the spacecraft position at the same point in time. Figure 8.1.2.2-2 shows a comparison of orbit radius, as a multiple of lunar mean radius, for the NRHO Vector and Keplerian modeling approaches.

To achieve this similarity, the Keplerian orbit uses same perilune radius, but the apolune radius is calculated from on the NRHO orbital period. This gives a value of several thousand kilometers less than the nominal apolune of about 71000km. The argument of periapsis for the vector list was also found to be close to ±2° from the lunar north pole. By tuning a standard Keplarian ellipse to match the orbital period and perilune of an NRHO, the orbital environments are closely matched those of a vector list. The time in eclipse was also calculated to be greater than 71min, which is closer to the maximum eclipse seen in 15 years of Gateway NRHO data than an unmodified ellipse.

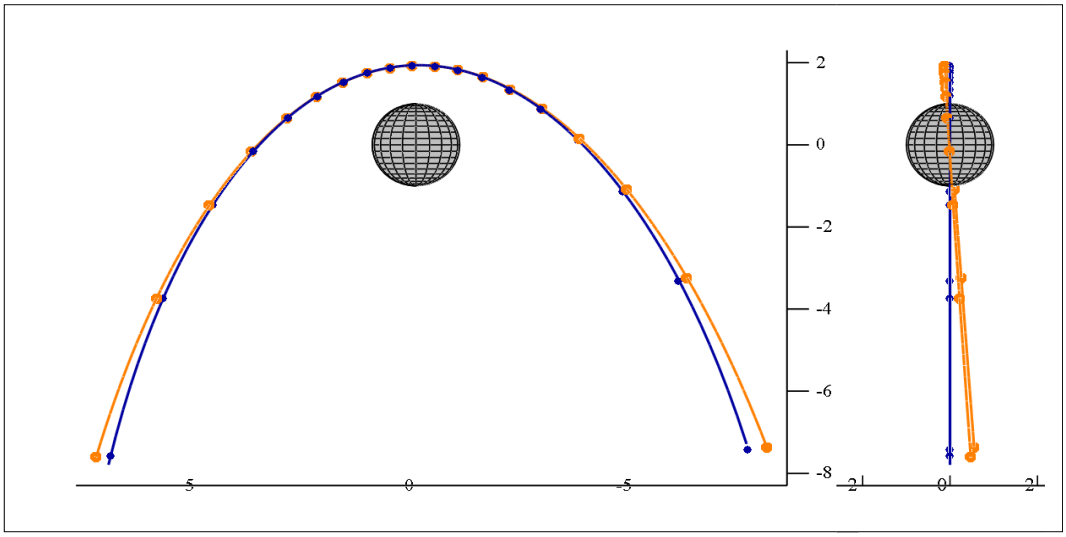

FIGURE 8.1.2.2-1: COMPARISON OF NRHO AND KEPLERIAN PERILUNE TRUE ANOMALY

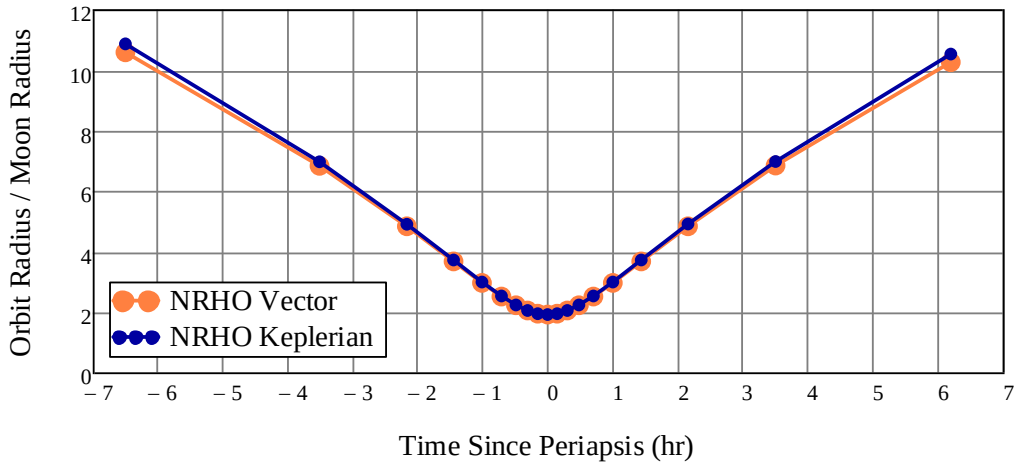

FIGURE 8.1.2.2-2: COMPARISON OF NRHO AND KEPLERIAN ORBITAL RADII NEAR MOON

For an NRHO, a beta angle of 0° maximizes both time in lunar shadow and proximity to and duration over the subsolar point. For hot case analysis, spacecraft should be placed over the subsolar point prior to entering lunar shadow. Cold case analysis should place the spacecraft through the lunar shadow prior to over the subsolar point. Another potential extreme case, depending on spacecraft design, is an NRHO with a beta angle of 90° oriented close to the terminator where the vehicle is always in the Sun, but doesn't fly over the subsolar point or through the lunar shadow. The orbital parameters of these NRHO Keplerian approximations are shown in table 8.1.2 below. The parameters for the 0° beta angle hot and cold are nearly identical, but by moving the Right Ascension of the Sun 180°, the direction of spacecraft approach, Sun declination angle, and time in eclipse are all adjusted accordingly for the cold case.

TABLE 8.1.2.2-1: ORBITAL PARAMETERS FOR KEPLERIAN NRHO APPROXIMATION WITH BOUNDING ENVIRONMENTS

Orbital Parameter	Hot (Beta 0°)	Cold (Beta 0°)	Cold (Beta 90°)
Orbit Inclination	90	90	90
Right Ascension of Ascending Node (RAAN)	270	270	90
Argument of Periapsis	88	88	90
Right Ascension of the Sun (RAS)	90	270	0
Right Ascension of the Prime Meridian	0	0	0

[1] D. E. Lee, "Gateway Destination Orbit Model: A Continuous 15 year NRHO Reference Trajectory", NTRS 20190030294, Aug. 2019

[2] J. R. Smith. "Gateway Passive Thermal Guidelines and Model Utilization – IAC4", Oct. 2019

8.2 LOW LUNAR ORBIT (LLO)

8.2.1 Description

Missions to and from the lunar surface often utilize a LLO, either for vehicle staging, system checkouts, or syncing with a spacecraft in another orbit such as an NRHO. An LLO presents several thermal challenges given the solar flux combined with lunar albedo and high planetary long-wave radiance. Just like an NRHO, a beta of 0° will maximize time in lunar shadow and the influence of the subsolar point. A beta of 90° results in zero time in lunar shadow and the orbital path is about the terminator.

8.2.2 Modeling Approach

If the Low Lunar orbit is circularized, environments can be varied by sweeping the orbit beta angle. For simplified orbits, with the Right Ascension of the Sun (RAS) set to 0° and the Right Ascension of the Ascending Node (RAAN) set to 90°, the beta angle is equal to orbit inclination. If the low lunar orbit is elliptical, care should be taken to set the argument of periapsis such that time in shadow or the influence of the subsolar point creates worst case environments while sweeping beta angle.

8.3 DESCENT/ASCENT

This section describes one method of modeling the ascent/descent phases of a lunar mission given a landing and/or launch trajectory profile. This mission phase is described by going from low lunar orbit down to the surface, or the surface to low lunar orbit. It focuses on modeling the trajectory, and does not provide a full comprehensive discussion on modeling methods. If a landing/launch trajectory profile is not known then it may be reasonable to bracket it by a worst case hot and cold. Where hot spends a majority on the Sun side and flies over the sub-solar point before landing, and cold spends a majority in the shadow side of the Moon. Even if the trajectory is known, it may still be reasonable to do the bracketing hot and cold case to simplify the amount of analysis work.

The work described in this section is taken from Alexander Szerszen's Thermal Fluid Analysis Workshop (TFAWs) paper and presentation titled "Thermal Environment Modeling Practices for the Descent Trajectory of Lunar Landers". Copies of which can be found on the NASA Technical Reports Server: paper link, presentation link.

It should be noted that this method is just one method, and it being discussed here should not be interpreted as being the only method, or the best method to use. Also this method has also not been correlated to a flight landing. Therefore users of this method assume the responsibility for its use and results.

8.3.1 Description

Descent/Ascent is a complex thermal environment including thruster firings, soak back, and electronics units with varying power dissipations versus time. It is important to check all the applied heat loads and ensure they are being applied at their proper time.

One important aspect is ensuring the vehicle is in the correct orientation during this period of time. The approach described below discusses how to do that for certain trajectory inputs.

The modeling approach assumes one will be using the heating rate case manager in Thermal Desktop to model the lunar surface. In other words, it does not explicitly create a lunar surface terrain model, but is using the IR planetshine versus latitude/longitude input (as described in Section 7.2 of the Guidebook). Therefore, this method does not capture flying in between hot hills, over localized cold craters, etc.

It is important for the model to initialize from an appropriate run, or that there is enough simulation time at the beginning to ensure that proper initial conditions have been reached.

8.3.2 Modeling Approach

As described above, this section focuses on ensuring that the vehicle is in the proper orientation during ascent/descent when given a trajectory profile.

Most descriptions of vehicle orientation during descent/ascent will be given with respect to the velocity vector. Currently in Thermal Desktop (V6.0) there is no built option to point a vehicle along the velocity vector for a terrestrial heating rate case. This can be done using a basic orbit heating rate case, which then could use a time dependent symbol to vary the altitude versus time. So if a

user's given problem can use a basic orbit heating rate case, then that is likely the best place to start. However, since there are thruster firings, which will change the orbit parameters versus time, using a terrestrial heat rate (where a user defines latitude/longitude/altitude versus time) may be what is needed.

Additionally for the method described here it assumes that no velocity vectors or vehicle rotations are available, and all that is known is the latitude, longitude, and altitude versus time.

Given this, a MATLAB® script was written to determine the individual vehicle rotation per time step based on the change in latitude, longitude and altitude. A copy of the script is given in Appendix E. The code works by taking the change in latitude, longitude and altitude per each time step and then determining the rotation in Cartesian coordinates necessary to keep the vehicle "perpendicular" to the Moon. The method allows for any number of rotations of the lander to orient itself and it will always simplify back down to three base rotations.

This method is based on aligning the vehicle to the celestial coordinate system, which in Thermal Desktop can be implemented in the orientation tab of the heating rate case manager. Aligning to Celestial Coordinate System (CCS) will place the World Coordinate System (WCS) that the model was built in along the Moon's coordinate system. So the WCS X-axis will align with the Moon's Vernal Equinox, the WCS Z-axis will align with the north pole, and the WCS Y-axis will be the cross-product of the other two axes.

The first inputs needed for Thermal Desktop are the Right Ascension (RA) of the Sun and right ascension of the prime meridian. These values need to be determined by the user and special care must be taken when inputting these values into Thermal Desktop. It is advised that anyone making a descent trajectory in Thermal Desktop read section 6.1.2 of the Thermal Desktop user manual and fully understand how the values for the right ascensions are interpreted. One way of looking at these settings is that the RA of the Sun sets the time of year, and RA of the Prime Meridian sets the time of day. If the exact time of landing is not known, a thermal analyst may want to bracket the analysis by setting these values to two cases: a hot case where the descent is maximum time in the Sun, and a cold case where the descent is minimum time in Sun.

The first step of creating the descent heating rate case is inputting the right ascensions, latitude, longitude and altitude versus time. Figure 8.3.2-1 presents an example of the Thermal Desktop interface for the terrestrial heating rate case and can be seen below with the primary inputs that shape the descent.

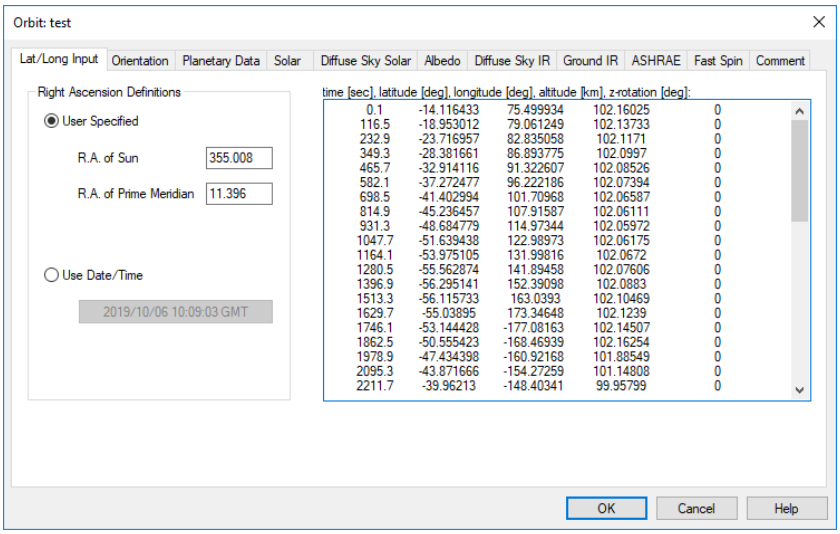

FIGURE 8.3.2-1: IMAGE OF THERMAL DESKTOP ORBIT INTERFACE

With the above data entered, an orbit similar to the one displayed in Figure 8.3.2-2 below can be obtained. The latitude, longitude and altitude of the lander versus time will now be correctly simulated but the orientation of the lander is not taken into account yet. Without any other input, the orientation of the lander will be fixed for all locations, the x-axis of the lander will be fixed parallel to the x-axis (vernal equinox) of the planet as will the y and z-axes. In Figure 8.3.2-2, the sequence of coordinate systems around the Moon represent each time step in the descent.

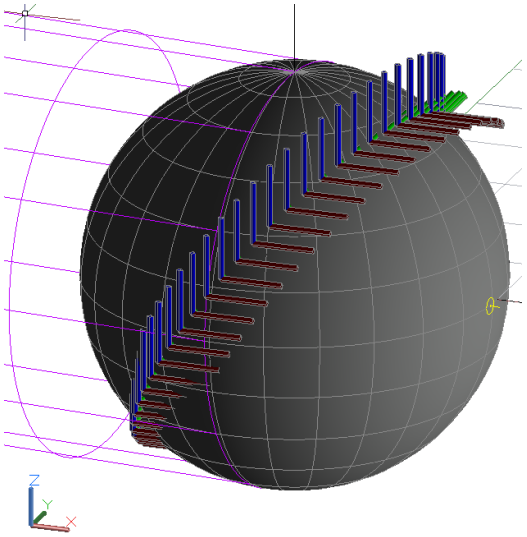

FIGURE 8.3.2-2: IMAGES OF LANDER ORIENTATION DURING DESCENT.

To ensure proper orientation, several rotations per time step are required, but only three additional rotations are currently allowed in Thermal Desktop. The first two rotations can be taken directly from the latitude and longitude. This can be simply done if the lander is rotated along the WCS Z-axis by the lander's longitude plus the value of the right ascension of the prime meridian at each time step, the WCS X-axis will point through CCS Z-axis. The right ascension of the prime

meridian is added into the Z-axis rotation because the right ascension of the prime meridian offsets the vernal equinox (x-axis) clockwise from the latitude/longitude origin (0,0) in Thermal Desktop. If the lander is then rotated along the WCS Y-axis by the negative value of the lander's latitude at each time step, the WCS X-axis will always point through the center of the Moon. At this point a rotation about the WCS X-axis is needed to ensure that the WCS Z-axis points along the velocity vector. To do this, the difference in latitude and longitude between two time steps is taken and used to calculate the angle of decline (or incline) between the two points. Figure 8.3.2-3 below shows how this can be done.

$$\theta_1 = tan^{-1}\left(\frac{y}{x}\right)$$

$$\theta_2 = tan^{-1}\left(\frac{x}{y}\right) + 90°$$

$$\theta_3 = tan^{-1}\left(\frac{y}{x}\right) + 180°$$

$$\theta_4 = tan^{-1}\left(\frac{x}{y}\right) + 270°$$

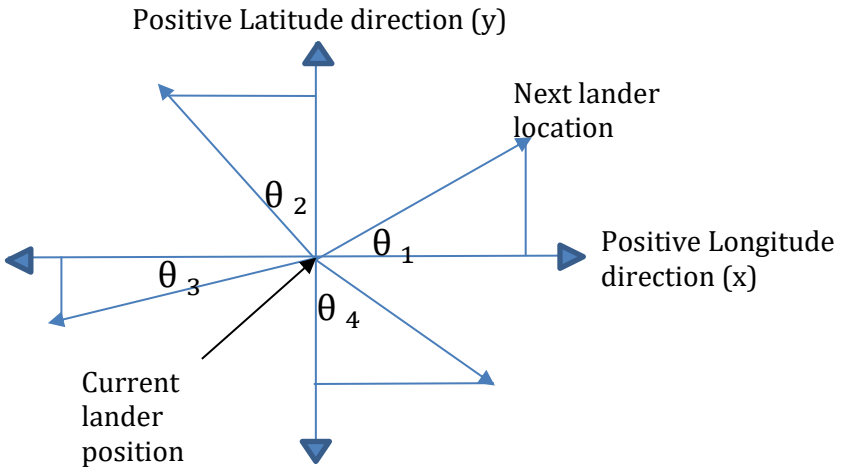

FIGURE 8.3.2-3: DEPICTION OF HOW THE X-AXIS ROTATION CAN BE DETERMINED

The difference in degrees between latitude and longitude is being used here as a length and the actual distances can be calculated with the known radius and altitude but those additional calculations are unnecessary. When looking at the lander points normal to the Moon, the altitude and curvature of the descent become mostly irrelevant so that just the angle of decline (or incline) between points is pertinent. With these calculations, the trajectory in Figure 8.3.2-4 can be obtained.

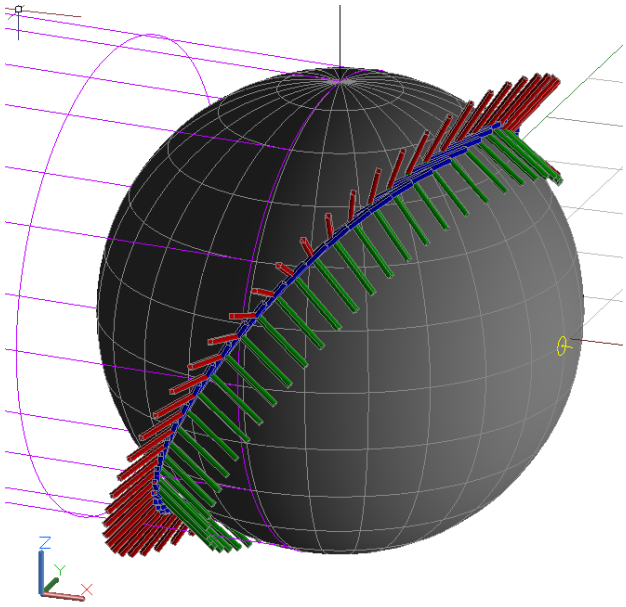

FIGURE 8.3.2-4: TRAJECTORY OF LANDER WITH THE Z-AXIS FACING THE VELOCITY VECTOR AND THE X-AXIS POINTING AWAY FROM THE CENTER OF THE PLANET.

If a trajectory like the one seen in Figure 8.3.2-4 is desired, then no further calculations are required. However, if additional rotations are required, then rotation matrices must be employed to account for additional rotations in order to input the data into Thermal Desktop. A rotation matrix is a matrix that is used to perform a rotation in Euclidean space. Rotation matrices are needed to simplify any extra rotations down to three base rotations.

To employ these additional rotations, one starts with an identity matrix then multiplies it by the rotation matrix for each axes being rotated about. Equation 1 below shows an example, note other users may have additional rotations, which can be added to the end. For this example, the lander is rotated about the WCS X-axis by alpha, then rotated about the WCS Y-axis by beta and finally rotated about the WCS Z-axis by gamma. Note, not all users will have their lander oriented in the WCS similarly. The additional rotations at the end are how one would ensure that they achieve the proper orientation at every time step. The first three rotations will ensure that the WCS is uniform for all time steps as seen in Figure 8.3.2-4. With that done, the user can then view the detailed WCS orientation from the surface to then add on any additional rotations for each time step to make sure that the lander is oriented properly based on their custom WCS settings. Note that matrix multiplications are order dependent so it is important that the user places their desired rotations at the end.

$$R(i) = I_3 * R_z(Longitude(i) + RA\ of\ prime\ meridian) * R_y\left(-Latitude(i)\right) * R_x\left(-\theta_{x_{rot}}(i)\right) * R_x(\alpha) * R_y(\beta) * R_z(\gamma) \quad (1)$$

Add on any additional rotations at the end and when simplifying down to three rotations, take the final matrix obtained and equate it to a rotation matrix using three base rotations as is shown below in Equation 2.

$$R = R_z(\phi)R_y(\theta)R_x(\psi)$$
$$= \begin{bmatrix} cos\theta\ cos\phi & sin\psi\ sin\theta\ cos\phi - cos\psi\ sin\phi & cos\psi\ sin\theta\ cos\phi + sin\psi\ sin\phi \\ cos\theta\ sin\phi & sin\psi\ sin\theta\ sin\phi + cos\psi\ cos\phi & cos\psi\ sin\theta\ sin\phi - sin\psi\ cos\phi \\ -sin\theta & sin\psi\ cos\theta & cos\psi\ cos\theta \end{bmatrix} \quad (2)$$

With the matrix above, it can be seen that solving for theta (θ) is simple whereas both phi (φ) and psi (ψ) have two solutions. To solve for phi and psi, one needs to use 2-argument arctangent as shown in the Equations 4 and 5.

$$\theta = asin(-r_{31}) \quad (3)$$

$$\psi = atan2(r_{32}, r_{33}) \quad (4)$$

$$\phi = atan2(r_{21}, r_{11}) \quad (5)$$

The conditions regarding how to use 2-argument arctangent are shown below in Figure 8.3.2-5 . Once this is done, theta, psi, and phi can be obtained for each time step. This can be done by hand, but MATLAB® also has 2-argument arctangent built into the software.

$$\operatorname{atan2}(y,x) = \begin{cases} \arctan(\frac{y}{x}) & \text{if } x > 0, \\ \arctan(\frac{y}{x}) + \pi & \text{if } x < 0 \text{ and } y \geq 0, \\ \arctan(\frac{y}{x}) - \pi & \text{if } x < 0 \text{ and } y < 0, \\ +\frac{\pi}{2} & \text{if } x = 0 \text{ ard } y > 0, \\ -\frac{\pi}{2} & \text{if } x = 0 \text{ and } y < 0, \\ \text{undefined} & \text{if } x = 0 \text{ and } y = 0. \end{cases}$$

FIGURE 8.3.2-5: EXPRESSION FOR 2-ARGUMENT ARCTANGENT IN TERMS OF STANDARD ARCTANGENT FUNCTION.

With the base three rotations per time step solved for, one can then move back to Thermal Desktop and finish creating the heating rate case. To do this, create symbol arrays for time, theta, psi, and phi in the Symbol Manager, select the option “Align to Celestial Coordinate System” on the orientation tab for the terrestrial heating rate case, select the order of the additional rotations and finally use the “interp” function as an expression for each of the three additional rotations. Note that the interpolation is being done using the Thermal Desktop automatically generated system “hrTimeSec” that sets the current heating rate time. Figure 8.3.2-6 and Figure 8.3.2-7 gives an example of how this is done in Thermal Desktop.

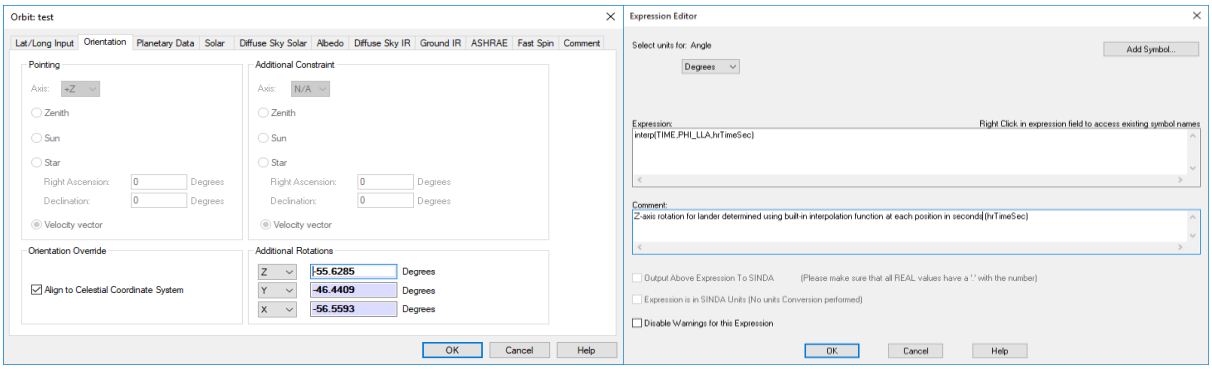

FIGURE 8.3.2-6: EXAMPLE OF OF SYMBOL ARRAY IN THERMAL DESKTOP

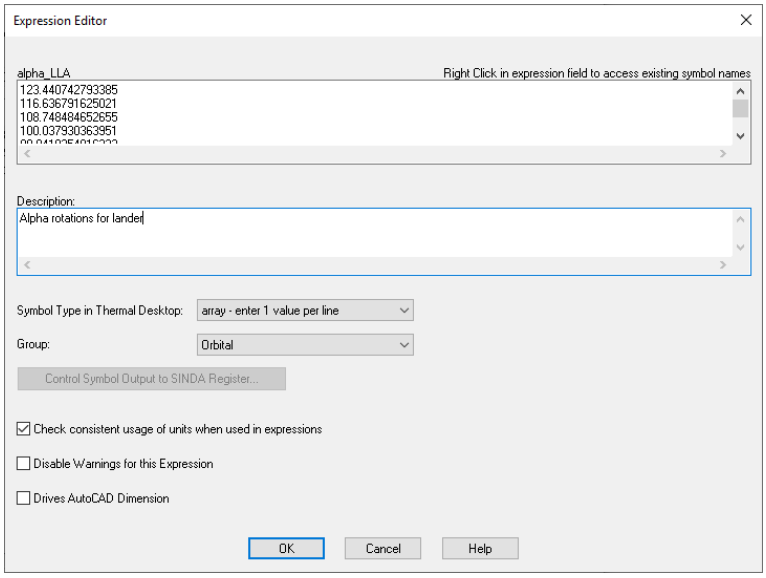

FIGURE 8.3.2-7: IMAGES OF THERMAL DESKTOP ORBIT INTERFACE SHOWING

With all this done, one can then obtain an orbit similar to the one shown in Figure 8.3.2-8. This orbital view is a good way to check that the lander rotations have been calculated and entered correctly. Another way to check the lander's orientation during descent is to view the lander from the perspective of the Moon in Thermal Desktop for each time step of the descent. Both methods should be checked to ensure that the lander is properly oriented for the entire descent.

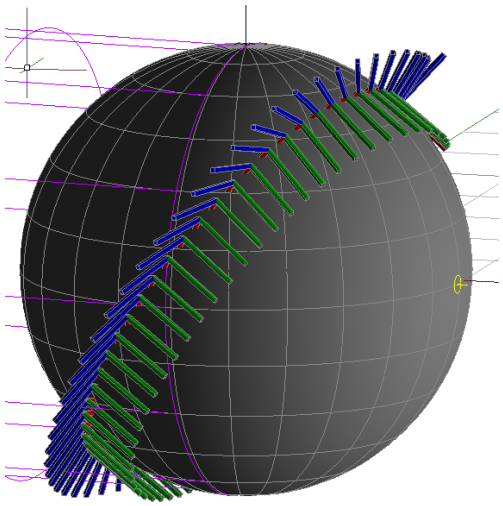

FIGURE 8.3.2-8: IMAGE OF FINAL LANDER ORIENTATION DURING DESCENT.

Note that the latitude, longitude, and altitude versus time will need to be inputted in to the Thermal Desktop units, so conversion may be necessary before inclusion. A copy of the MATLAB® referenced here is given in the Appendix E.

9.0 LUNAR SURFACE MODELING GUIDELINES/APPROACHES

Different techniques are used to predict temperatures of objects on the lunar surface than objects orbiting the Moon. This section presents techniques for building thermal models that include the lunar surface. Discussion is geared towards models intended for vehicle level thermal analysis. Often this type of analysis is performed using software such as Thermal Desktop, ESATAN™, COMSOL®, TherMoS™, etc. However, examples given here are limited to Thermal Desktop.

The level of detail required when modeling the lunar surface depends on the point in a design cycle. The LRO derived surface temperatures (section 5.2.1) and analytical expressions (section 5.2.2) are useful for initial sizing of thermal control components with hand calculations.

As a design matures, more accurate results can be produced once a thermal model of a vehicle is built and placed on the Moon's surface. Since the top layer of the lunar regolith has a very low thermal conductivity, incident heating or shadowing from a vehicle on the Moon's surface can cause the surface temperature to change significantly and quickly. This in turn impacts the temperature of the vehicle itself [1]. Therefore, it is generally necessary to calculate surface temperatures as opposed to setting surface temperatures to boundary temperatures obtained.

A common way to model the lunar surface is to represent the ground with simple geometric shapes [2 – 5]. For example, terrain may be simple flat or sloped plates, cylindrical valleys, or bowl or conic craters. Depending the desired level of fidelity and landing site, this approach may or may not be sufficient. This approach works well in flat regions such as the Mare regions near the Apollo 11 landing site. This method is described in detail in section 9.4.2.

It may be possible add simple representations of nearby mountains or plateaus that can heat or shade a vehicle in order to improve the fidelity of a simple geometric model [6]. This approach is described in Section 9.4.3.

However, representing the ground with simple geometric shapes is not accurate in an areas with very rough terrain. For example, at the South Pole craters with permanently shadowed regions (PSRs) often have complex shapes and cannot be treated as cones or bowls. (Other special considerations for modeling PSRs are provided in Section 11.0).

Another way to model the lunar surface is to represent the ground as meshed object [7, 8]. Including a ground mesh enables more accurate prediction of solar blockage and heating from nearby surface features. Since the South Pole has a rough terrain, before finalizing a design, it may be necessary to include detailed lunar topography in a thermal model. However, when representing the lunar surface as a mesh, it is easy to create a thermal model that will take several days to run. Care must be taken in balancing the required level of surface detail with model run time.

Moreover, the presence of lunar dust on a vehicle can impact its temperatures. Section 10.0 discusses how to account for lunar dust when conducting thermal analysis.

[1] J. F. Gasbarre, R. M. Amundsen, S. Scola, F. B. Leahy, and J. R. Sharp, “Ground Plane and Near-Surface Thermal Analysis for NASA’s Constellation Programs,” p. 13, 2008.

[2] D. A. Ochoa, B. M. Miranda, B. C. Conger, and L. A. Trevino, “Lunar EVA Thermal Environment Challenges,” *SAE Transactions*, vol. 115, pp. 492–505, 2006.

[3] R. Christie, D. Plachta, and M. Hasan, “Transient Thermal Model and Analysis of the Lunar Surface and Regolith for Cryogenic Fluid Storage,” Aug. 2008.

[4] T.-Y. Park, J.-J. Lee, J.-H. Kim, and H.-U. Oh, “Preliminary Thermal Design and Analysis of Lunar Lander for Night Survival,” 2018.

[5] B. O’Connor and E. Abel, “Radiator Study for Stationary Lunar Landers,” NESC Thermal Fluids and Analysis Workshop, 2018.

[6] H. Rana, V. Laneve, P. Hager, and T. Tirolien, “Thermal Modelling of Luna 27 Landing Site,” p. 10, 2017.

[7] D. A. Paige et al., “Diviner Lunar Radiometer Observations of Cold Traps in the Moon’s South Polar Region,” Science, vol. 330, no. 6003, pp. 479–482, Oct. 2010.

[8] T. J. Warren, O. King, N. E. Bowles, E. Sefton-Nash, R. Fisackerly, and R. Trautner, “The Oxford 3D Thermophysical Model with Application to the Lunar PROSPECT Mission,” Lunar and Planetary Science Conference, p. 2040, Mar. 2019.

9.1 MODELING THE GROUND-PLANE SOLAR ENVIRONMENT

When modeling the lunar surface in Thermal Desktop, the radiative environment is defined by 1) creating a heat rate case (i.e. an orbit), 2) configuring a case’s radiation analysis tasks to include calculations for both *heating rates* and *radks*. A *heat rate* is defined as $\sigma\, radk\, (T_i^4 - T_j^4)$, were σ

is the Stephan Boltzmann Constant and T_i and T_j corresponding to the temperature of surface *i* and *j.* A *radk* is defined as $\varepsilon_i A_i B_{ij}$ where ε_i is the emissivity of surface *i*, A_i is the area of surface *i*, and B_{ij} is the grey-body exchange factor from *i* to *j* [1].

Sections 9.1.1 and 9.1.2 describe different heat rate cases that can be used to calculate incident solar heating. These are 1) terrestrial orbits, and 2) trajectory orbits. See the Thermal Desktop user's manual for additional explanations (Panczak et al. 2017).

Each orbit, like basic and Keplerian orbits, creates an idealized spherical planet whose temperature uniformly reflects/emits energy according user defined temperatures or fluxes. All modeled objects are placed above the idealized planet and will be heated as specified in the IR Planetshine dialog box by the idealized planet unless blocked by another object.

Since the idealized planet's emitted IR is unaffected by objects above it, if we wish to predict temperatures of a lander on the Moon, a separate ground surface must be modeled. The ground should 1) be large enough to block any radiation exchange between the idealized planet and the lander [2], and 2) have adequate nodalization to capture temperature gradients due to the lander's shadow. Moreover, to prevent unnecessary computation, the backside of the ground to should not participate in radiation calculations.

Configuring Radiation Analysis Tasks

To do this, first go to the *Case Set Manager* and select the desired case. Then create a radiation task with *Radks* as the calculation type. This will determine the IR energy exchange between the lunar surface and objects on it. Set the space node temperature to 2.73 K. This is needed to for a correct energy balance at the surface because the heat rates (not the space node) define incident heating. The rational is provided in the Thermal Desktop Manual Section 6.1.4.1 "Radk Calculations with Planetary Surface Modeling" [1].

Next, create a radiation task with *Heating Rates* as the calculation type. Use the same radiation analysis group as the *Radks* radiation task and select the predefined orbit to use in the calculations. In the Radiation Analysis Data tab, shown in Figure 8.3.2-1, only Solar should be selected at a heat rate source[2]. Otherwise, a tilted ground plane could see incident IR Planetshine. As a result, any user specified lunar surface temperatures, ground emissivity, and albedo in the *Heat Rate Case Manager* will not affect the ground temperatures.

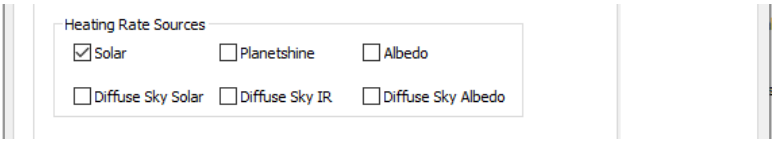

FIGURE 9.1-1: CONTROL TAB IN CASE SET MANAGER>CASE> RADIATION TASKS> RADIATION ANALYSIS DATA DIALOG BOX.

Thermal Desktop tracks several orbit parameters as heat rate symbols. These include the x y and z unit vectors from the ground to the planet's center as well as the unit vector from the ground to the Sun (e.g. HRPLANETX, HRSUNX). To view their resulting values with other SINDA registers,

[2] Diffuse Sky Solar and IR are not needed because the Moon has no atmosphere.

select the *Output HR Symbols to SINDA* option in the *Heat rate Output* tab of the heat rate's radiation task. You can also view them in the Symbol Manager and Model Browser (in TD Version 6.0 or higher).

While the solar elevation angle is not given, both it and the solar zenith angle can be calculated using the dot product of the unit vectors from the ground to planet center and unit vectors from the ground to the Sun [3,4]

9.1.1 Traditional Orbit Definition

One orbit type useful for lunar surface thermal modeling is a *Terrestrial orbit* (also called planetary orbit). Terrestrial orbits (also called planetary orbits) automatically calculate the solar elevation angle and resulting incident solar heat rates for a given latitude, longitude, altitude, and solar declination angle. Terrestrial orbits are made using the *Heat Rate Case Manager (aka Orbit Manager)*, by selecting the *Planetary Latitude/Longitude/Altitude List* option for a new heating environment.

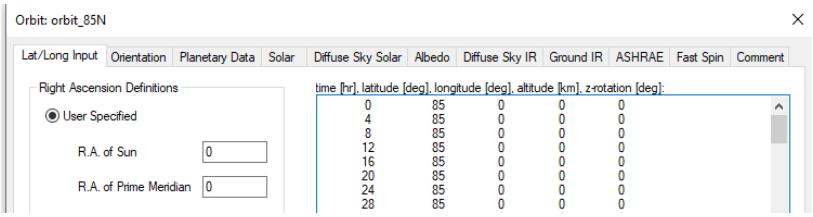

FIGURE 9.1.1-1: HEATING RATE CASE MANAGER > TERRESTRIAL > LAT/LONG INPUT TAB.

Terrestrial orbit parameters are specified in the orbit's heat rate case dialogue box. The *Planetary Data* tab is used to set information about the idealized planet (e.g. radius). Thermal Desktop has presets for the major planets and Earth's Moon. The max inclination of the Moon's equator (1.54º) is set in the *Planetary Data* tab. The actual inclination used for heat rate calculations is controlled by changing the right ascension of the Sun (RA Sun). For example:

- RA Sun = 0 → declination = 0°.
  - This corresponds to the fall and spring equinox.
- RA Sun = 90 → max declination =1.54°.
  - This corresponds to summer solstice, and summer at positive latitudes (North).
- RA Sun = 270 → min declination is min-1.54°.
  - This corresponds to winter solstice, and winter at positive latitudes (North).

For a single orbit, the RA of the Sun is a static value that cannot be updated.

This orbit type is easy to setup and use. In many scenarios the worst case cases can be estimated assuming the max/min declination angles. However, to run an analysis with a changing declination angle, multiple cases with different orbits would need to be pieced together.

The orbit's starting point is determined by the difference between the right ascension of the prime meridian and the right ascension of the Sun. To begin a run at solar noon, set the right ascension of the prime meridian equal to the right ascension of the Sun [1]. Longitude = 0 at the prime meridian.

Note that the sidereal period (time for the Moon to rotate once) and the mean solar day are different. The heat rates on the vehicle and ground cycle with the solar day. Therefore, the orbit period should be set to the mean solar day of 708.7hrs.[3]

The vehicle's location is set in the *Lat/Long Input* tab via setting the following: time, latitude, longitude, altitude, and z-rotation. Latitude describes the angle from the equator (e.g. degrees North) and longitude describes the angle from the plane perpendicular to the equator (e.g. degrees East). The planet is assumed to be a perfect sphere. Positive/negative convections for Latitude and Longitude are: Latitude + North, - South, Longitude + East, - West. The altitude describes the distance the modeled objects are raised above the idealized planet's surface and cannot be negative. Z-rotation, is the rotation of all modeled objects.

If the vehicle does not move, only change values for time. The last time value provided specifies the orbit period. Incorrectly setting the orbit period will lead to incorrect results.

9.1.2 Orbit Vector List

The second type of orbit useful for lunar surface thermal modeling is a *trajectory orbit*. A trajectory orbit can be defined with the **Heat Rate Case Manager** by selecting the Orbital Sun/Planet/Radius Vector List option for a new heating environment [1]. This type of orbit requires the following to be defined at each time interval: solar vector, planet factory, ratio of distance from planet center to planet radius.

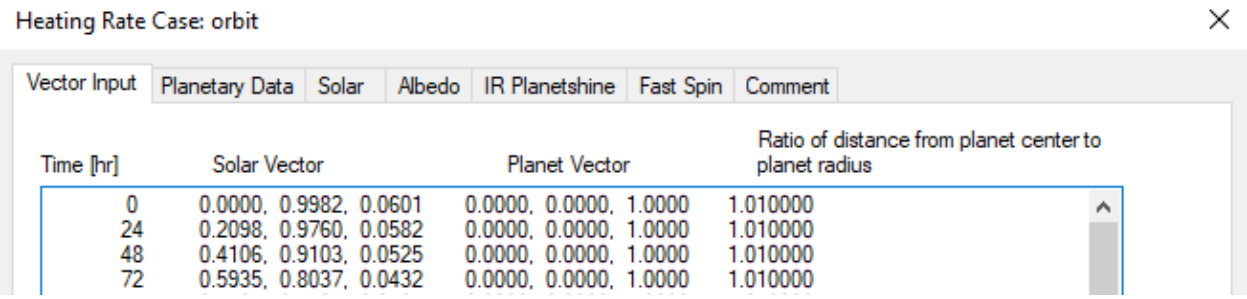

FIGURE 9.1.2-1: HEATING RATE CASE MANAGER > TRAJECTORY > VECTOR INPUT TAB.

The advantage of this orbit type is that the vectors can account for the different lunar seasons. Where the terrestrial orbit requires piecing together multiple orbits to change solar declination for a solution. When using this type of orbit, the Sun vector will cycle both above and below the x-y plane. An artificial barrier may be needed in the model to prevent small amounts of sunlight from hitting the terrain of interest during when the Sun's elevation angle is negative.

For analysis at the Moon's South Pole, this orbit type is particularly useful, because the radiative environment changes significantly with the season. Seasons on the lunar surface change as the solar declination angle on the Moon alternates between 1.54º and -1.54º over the course of

[3] The sidereal period determines the rate of planet rotation, while the ground and vehicle's position is determined by the solar period. This does not impact analysis with constant Albedo and IR. (From email exchange with Doug Bell at CRTech).

roughly 354 earth days [5].To illustrate, a flat surface model was ran at a latitude of 85ºN for solar declinations of: 0º (RA of 0º), 1.54º (RA of 90º), and -1.54º (RA of 270º). The results are displayed in Figure 9.1.2-2. At solar noon the axis tilt caused a 35 K difference in the temperature predictions. During the lunar night the difference lessens to about 10 K.

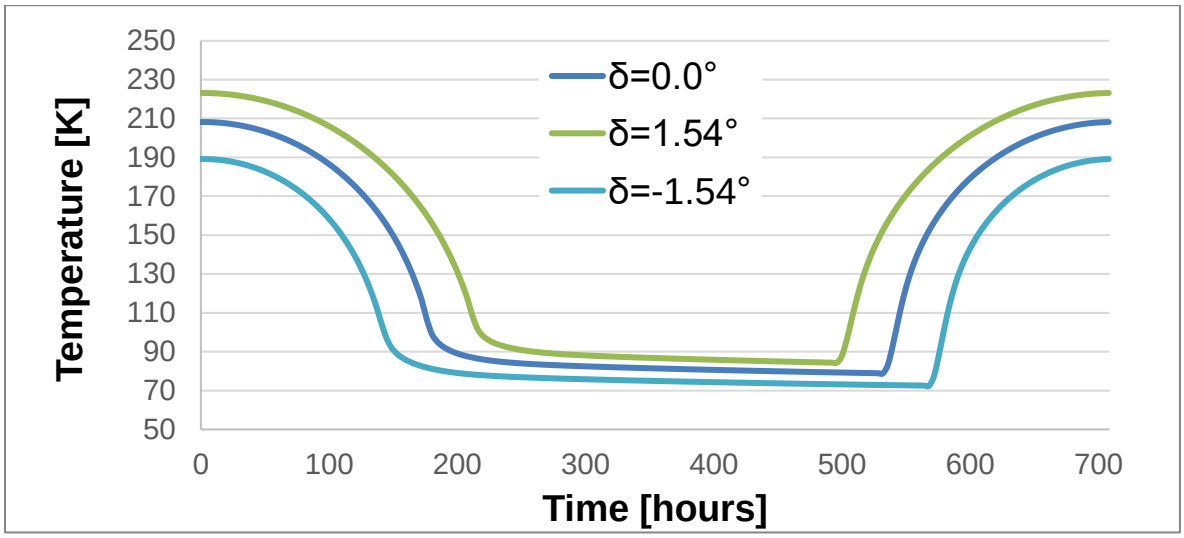

FIGURE 9.1.2-2: DIURNAL LUNAR SURFACE TEMPERATURES AT 0E AND 85N FOR DIFFERENT SOLAR DECLINATION ANGLES PREDICTED BY A FLAT PLANE SURFACE MODEL IN THERMAL DESKTOP.

An orbit vector list may be generated from an ephemeris. A web interface is available to provide limited access to the JPL HORIZONS application which may be used to generate ephemerides for solar system bodies [6]. Specifically for lunar analyses, the application allows placement of an observer anywhere on or above the surface of the Moon to tracking a target body (such as the Sun) via a set of user defined parameters. Elevation angle and azimuth are convenient for conversion into a vector list commonly used by thermal analysis applications such as Thermal Desktop. After accessing the web interface at https://ssd.jpl.nasa.gov/horizons.cgi#results, the user is presented with the following default settings:

Ephemeris Type [change] : **OBSERVER**
Target Body [change] : **Mars** [499]
Observer Location [change] : **Geocentric** [500]
Time Span [change] : Start=**2020-02-05**, Stop=**2020-03-06**, Step=**1 d**
Table Settings [change] : *defaults*
Display/Output [change] : *default* (formatted HTML)

Each setting may be altered through the “change” button. Leave the ephemeris type in *Observer* mode and change the target body to the Sun as shown in Figure 9.1.2-3.

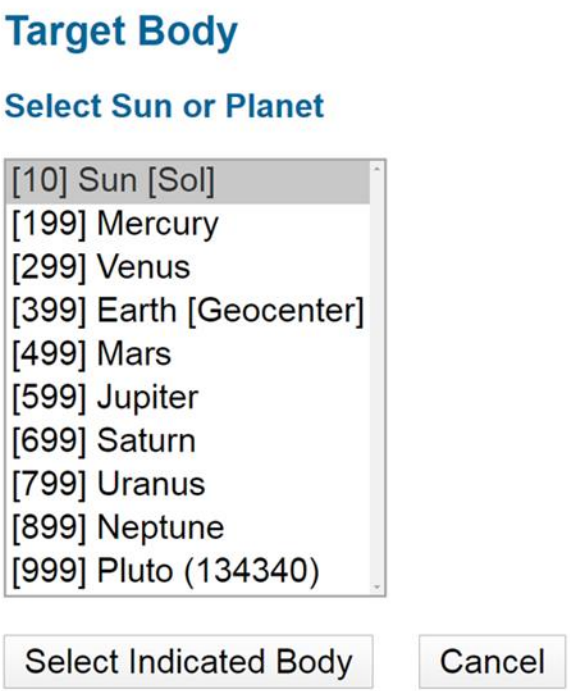

FIGURE 9.1.2-3: HORIZONS TARGET BODY

Change the observer location by entering the desired longitude, latitude and altitude into the displayed dialog (bottom of the web page) titled ***Specify Origin: Topocentric Coordinates***. Note that the altitude is specified with respect to the IAU reference ellipsoid surface for the Moon. The ***Body ID*** for the Moon is 301. Under ***Time Span***, enter the desired begin and end dates for the ephemeris. Under ***Table Settings*** the following options are displayed (see Figure 9.1.2-4). Select #4 ***Apparent AZ & EL*** and #13 ***Target angular diameter*** and select ***Use Selected Settings*** to continue.

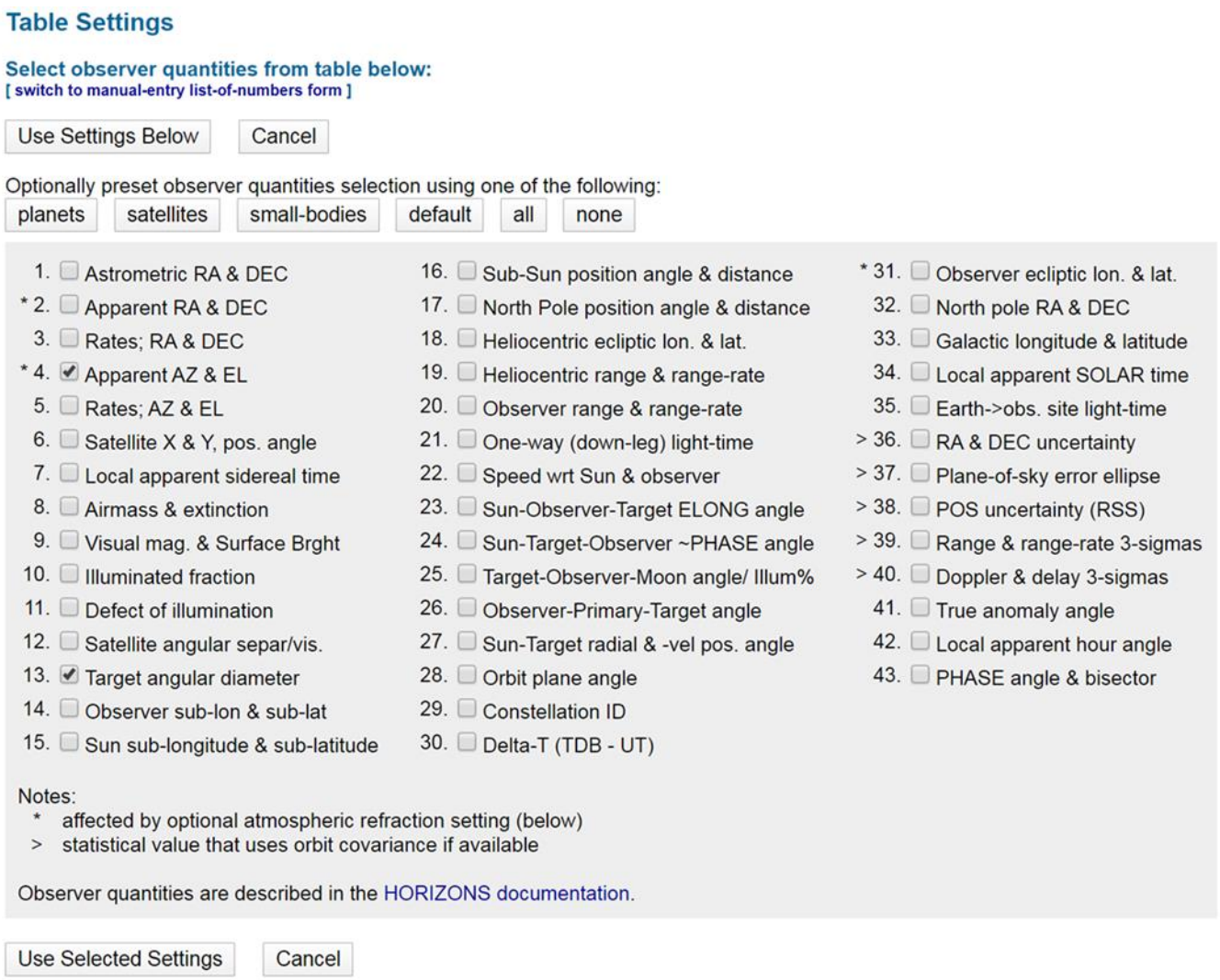

FIGURE 9.1.2-4: HORIZONS TABLE SETTINGS

The input form should appear as shown below:

Ephemeris Type [change] : **OBSERVER**
Target Body [change] : **Sun [Sol]** [10]
Observer Location [change] : Topocentric @301 [Moon] (**0°00'00.0"E, 89°00'00.0"N, 0.1 km**)
Time Span [change] : Start=**2020-02-04**, Stop=**2020-03-05**, Step=**1 d**
Table Settings [change] : QUANTITIES=**4,13**
Display/Output [change] : *default* (formatted HTML)

Select ***Generate Ephemeris*** to display the results. Typical results are shown in Figure 9.1.2-5.

```
Date__(UT)__HR:MN     Azi_(a-appr)_Elev Ang-diam
*********************************************
$$SOE
 2020-Feb-04 00:00 *x  118.8699  -0.4435 1945.383
 2020-Feb-05 00:00 *x  131.0140  -0.2902 1944.197
 2020-Feb-06 00:00 *x  143.1527  -0.1679 1943.127
 2020-Feb-07 00:00 *x  155.2869  -0.0828 1942.214
 2020-Feb-08 00:00 *   167.4176  -0.0394 1941.495
 2020-Feb-09 00:00 *   179.5460  -0.0403 1941.000
 2020-Feb-10 00:00 *   191.6739  -0.0862 1940.745
 2020-Feb-11 00:00 *   203.8029  -0.1757 1940.731
 2020-Feb-12 00:00 *   215.9349  -0.3057 1940.941
 2020-Feb-13 00:00 *   228.0714  -0.4714 1941.343
 2020-Feb-14 00:00     240.2138  -0.6664 1941.891
 2020-Feb-15 00:00     252.3635  -0.8831 1942.535
 2020-Feb-16 00:00     264.5210  -1.1129 1943.220
 2020-Feb-17 00:00     276.6869  -1.3465 1943.893
 2020-Feb-18 00:00     288.8612  -1.5745 1944.505
 2020-Feb-19 00:00  x  301.0436  -1.7873 1945.015
 2020-Feb-20 00:00  x  313.2334  -1.9763 1945.385
 2020-Feb-21 00:00  x  325.4298  -2.1333 1945.589
 2020-Feb-22 00:00  x  337.6313  -2.2519 1945.605
 2020-Feb-23 00:00  x  349.8365  -2.3272 1945.419
 2020-Feb-24 00:00  x    2.0435  -2.3562 1945.027
 2020-Feb-25 00:00  x   14.2507  -2.3381 1944.431
 2020-Feb-26 00:00  x   26.4563  -2.2744 1943.638
 2020-Feb-27 00:00  x   38.6587  -2.1685 1942.664
 2020-Feb-28 00:00  x   50.8565  -2.0260 1941.527
 2020-Feb-29 00:00  x   63.0487  -1.8541 1940.252
 2020-Mar-01 00:00  x   75.2344  -1.6614 1938.869
 2020-Mar-02 00:00  x   87.4131  -1.4572 1937.411
 2020-Mar-03 00:00  x   99.5848  -1.2514 1935.914
 2020-Mar-04 00:00  x  111.7495  -1.0538 1934.420
 2020-Mar-05 00:00  x  123.9074  -0.8737 1932.974
$$EOE
```

Figure 9.1.2-5: Ephemeris Table

The first column is the date/time stamp. The * symbol indicates daylight or the solar upper limb is on or above the apparent horizon. Absence of the symbol indicates night time or the Sun has set. “Azi” and “Elev” are the azimuth and elevation angles relative to the target center. Azimuth is measured clockwise from due north while the elevation angle is respect to the ground plane perpendicular to the local zenith direction. The final column is the angular diameter of the target (i.e. the Sun) in arc seconds (1 deg=3600 arc seconds). For this application, the angular diameter may be useful for blockage calculations by local terrain or the horizon.

The solar azimuth and elevation angles may be used to derive a unit vector for an orbit description within Thermal Desktop. If the z axis is the local vertical with the x axis pointing to the lunar North Pole, a local coordinate system may be defined as shown in Figure 9.1.2-6. The elevation angle is denoted as θ_a and the azimuth angle is denoted as α.

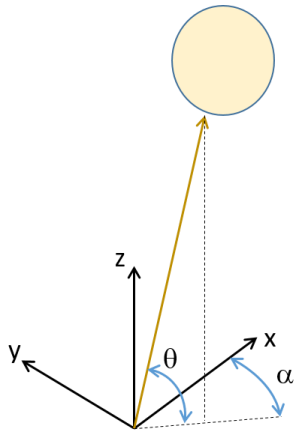

FIGURE 9.1.2-6: COORDINATE DEFINITION FOR SUN VECTOR

The solar vector (as described above) may be computed from the elevation and azimuth angles via the relation: $\vec{v} = \hat{\imath} \cos\theta_a \cos\alpha - \hat{\jmath} \cos\theta_a \sin\alpha + \hat{k} \sin\theta_a$.

Based on the local coordinate system with the z-axis as the local zenith, the planet vector may be defined as (0, 0, -1) as described above. Derive the ratio of distance from planet center to planet radius from the altitude previously entered into the ephemeris.

If the ground plane to be included in the thermal model is not oriented to the actual position on the lunar surface, the local (position dependent) azimuth and elevation angles from the ephemeris should be used to calculate the Sun vector with the ground plane oriented such that the x-axis is pointing toward the North Pole and the z-axis is the local zenith. However, if the ground plane is correctly positioned onto the spherical Lunar surface, it may be more convenient to obtain the direction of the Sun relative to the Lunar global coordinate system by specifying the Lunar North Pole as the observer location in the ephemeris. The Lunar global coordinate system has the z-axis coincident with the Moon's axis of rotation and the x-axis in plane with the Lunar prime meridian (pointing to the intersection of the equator and 180° east longitude). The relative Sun angle will virtually be correct as the modeled ground plane is already oriented properly to the Lunar global coordinate system. Because of the distance between the Sun and the Moon, the absolute angular difference in the Sun vector between the North pole and any location on the Lunar surface will be less than 0.002°.

For more information see the "HORIZONS user Manual" [6].

9.1.3 Solar Elevation Angle

The solar elevation angle for a point on the lunar surface is directly available from the HORIZONS ephemeris. The solar elevation angle may be used to compute the solar heat flux (as a function of time) upon the lunar surface. For a surface with a normal coincident with the local zenith, the flux is expressed as $\alpha\, S_O \sin(\theta_a)$ where S_O is the solar flux, θ_a is the solar elevation angle and α is the ground absorptivity (in the solar spectrum). The solar elevation angle must be adjusted to account for a surface normal not coincident with the local zenith. Incident fluxes may similarly be computed for assets on the surface such as habitats, landers, rovers, etc.

The yearly variation of the solar elevation angle from an observer located at a range of latitudes near the Lunar South Pole is shown in Figure 9.1.3-1. Negative elevation angles imply that the Sun is either totally or partially below the horizon. The seasonal variation is quite evident at the pole as the Sun sets below the horizon for approximately half of the calendar year. The local Sun angle is determined by the Moon's obliquity relative to the ecliptic plane with a superimposed monthly variation (Synodic period) resulting from variation of the local surface normal due to the difference in latitude from the pole. At the poles, the monthly variation is zero, resulting in the approximate sinusoidal curve shown below. The superimposed latitude induced variation is quite evident away from the poles and becomes the dominant factor at lower latitudes. A maximum elevation angle (for design purposes) may be obtained from the ephemeris by inputting a long time span (> 1 year).

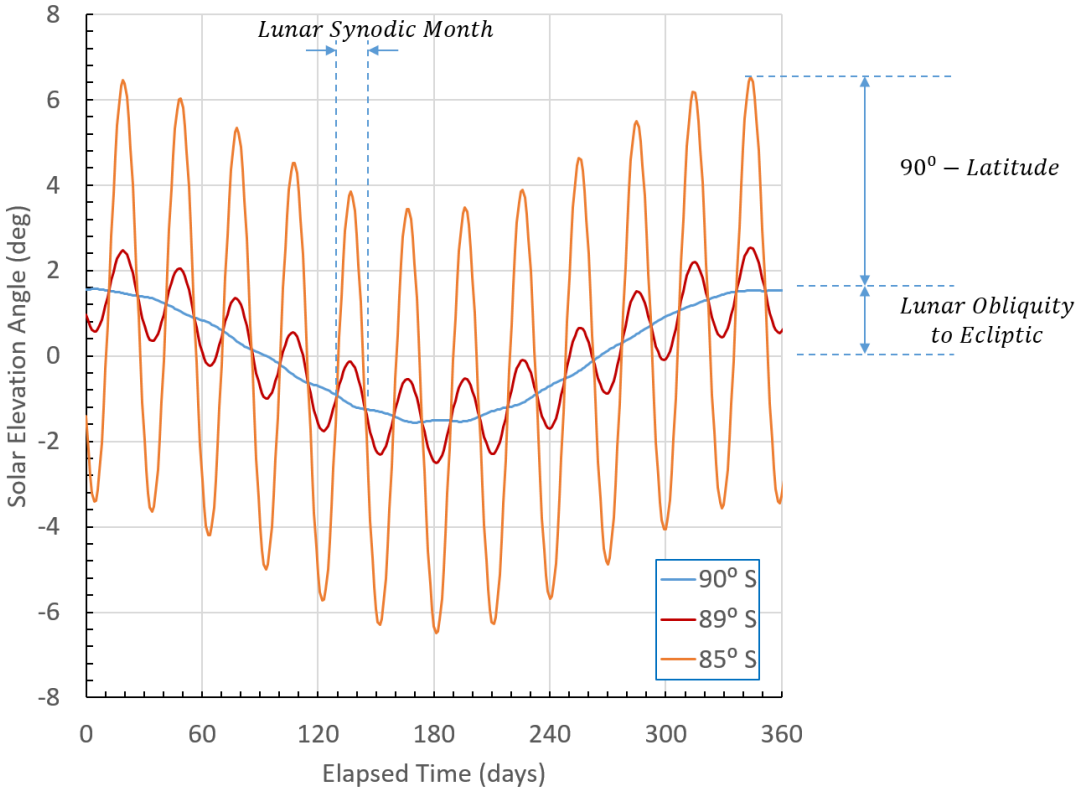

FIGURE 9.1.3-1: SOLAR ELEVATION ANGLE VARIATION OVER CALENDAR YEAR

The Sun has an apparent angular diameter of approximately 0.53º but the variation in angular diameter is also available through the ephemeris by selecting option #13 "Target angular diameter" as described above. The angular diameter of the Sun may be used to predict simple occultation as the Sun rises or sets above or below the horizon. Solar flux is directly proportional to the areal fraction of the visible Sun disc and may be estimated as shown in Figure 9.1.3-2.

$$\%Visible = \frac{acos\left(\frac{2H}{D}-1\right)-\left(\frac{2H}{D}-1\right)\sqrt{1-\left(\frac{2H}{D}-1\right)^2}}{\pi}$$

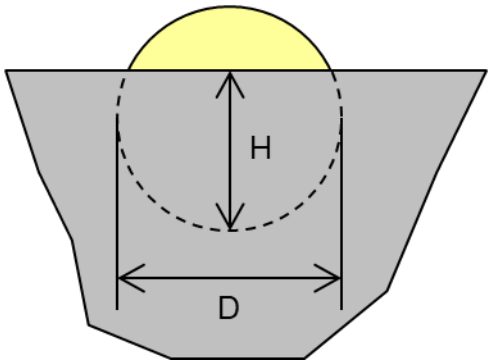

FIGURE 9.1.3-2: SOLAR OCCULTATION BASED ON HEIGHT AND DIAMETER

The percent visible may be expressed in a more convenient form (based on the solar elevation angle, θ_α and the angular diameter, ϕ) as shown in the equation below. The Sun occultation is shown in Figure 9.1.3-3.

$$\%Visible = \frac{acos\left(\frac{tan\,\theta_a}{tan\phi}\right)-\frac{tan\,\theta_a}{tan\phi}\sqrt{1-\left(\frac{tan\,\theta_a}{tan\phi}\right)^2}}{\pi}$$

$$-\phi \le \theta_a \le \phi$$

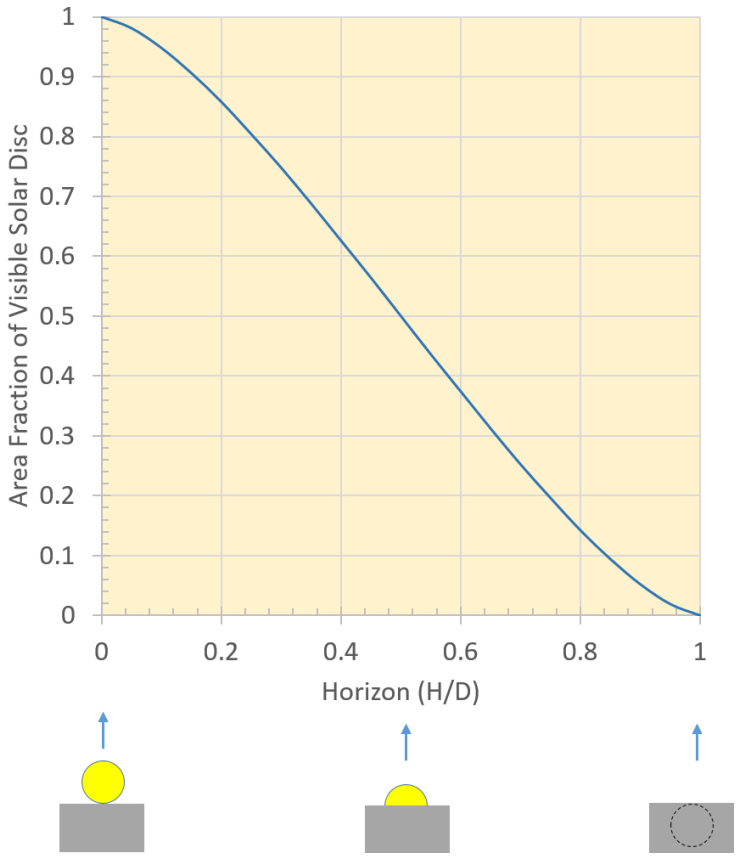

FIGURE 9.1.3-3: SOLAR OCCULTATION BASED ELEVATION AND ANGULAR DIAMETER

References:

[1] Timothy D. Panczak, Steven G. Ring, Mark J. Welch, David Johnson, Brent A. Cullimore, and Douglas P. Bell, “Thermal Desktop User’s Manual, CAD Thermal Analysis and Design Version 6.0.” C&R Technologies, Inc. (“CRTech”), 2017.

[2] J. F. Gasbarre, R. M. Amundsen, S. Scola, F. B. Leahy, and J. R. Sharp, “Ground Plane and Near-Surface Thermal Analysis for NASA’s Constellation Programs,” p. 13, 2008.

[3] R. A. Schowengerdt, *Remote Sensing: Models and Methods for Image Processing*. Chapter 2 “Optical Radiation Models” p. 52. Elsevier, 2006.

[4] M. Kharseh, “Solar Radiation Calculation,” Jun-2018, doi: http://dx.doi.org/10.13140/RG.2.2.34480.05129.

[5] A. Vasavada, D. Paige, and S. Wood, “Near-Surface Temperatures on Mercury and the Moon and the Stability of Polar Ice Deposits,” *Icarus*, vol. 141, no. 2, pp. 179–193, Oct. 1999.

[6] Giorgini, Jon, et al., “HORIZONS user Manual” Version 4.50, December 2019. (https://ssd.jpl.nasa.gov/?horizons_doc)

9.2 SUBSURFACE MODELING

Lunar surface and subsurface temperatures can be predicted by solving the following energy balance for 1D conduction across a d meter deep section of regolith [1]. In-plane conduction can be neglected because of the low thermal conductivity of the lunar surface [1,2]. d should be set such that $T(d) \approx constant$ throughout the year [3].

$$\dot{E}_{in} - \dot{E}_{out} = \dot{E}_{st}$$

$$\frac{\partial}{\partial z}\left(k\frac{\partial T}{\partial z}\right) = \rho c_p \frac{\partial T}{\partial t}$$

where k is the regolith's thermal conductivity, ρ is the regolith's density, c_p is the regolith's specific heat, $\frac{\partial T}{\partial t}$ is the change in regolith temperature for a given change in time, and $\frac{\partial T}{\partial z}$ is the change in regolith temperature for a given change in depth.

As discussed in section 6.0 both k and ρ are functions of z. Moreover, k and c_p are functions of T. Therefore, this differential equation is often solved using the finite difference method [4]. Using finite difference, the ground is split vertically split into n layers. Each layer is assumed have a uniform temperature and constant properties [2,3,5]. Layer sizes are discussed in 9.2.3. Since the initial conditions of the surface and subsurface are unknown, calculations are performed at each time step until the temperatures reach a cyclic steady state. This is discussed in section 9.2.4.

9.2.1 Approach

When building a lunar surface model in Thermal Desktop the ground can be built out of (1) finite difference (FD) solids, or (2) thin shells (including finite element surfaces).

Model with FD Solids: Create each layer with a different solid, since each solid has uniform properties. Merge nodes at interfaces or apply appropriate thermal contacts between layers.

Model with Thin Shells/Surfaces: First, create the top layer for the lunar surface with a built in TD shape such as a rectangle, disk, or paraboloid, or a finite mesh element. This top layer can be very thin (e.g. 0.001m). Second, define the remaining layers as a Material Stack in the Material Stack Manager (located in the Thermal > Thermophysical Properties drop down). In the Materials Stack Manager, the total number of layers is set, as well as the properties, thicknesses, and number of nodes per layer. A single node can be assigned to one layer. Additionally, the option to "generate lateral conductors" can be unselected since the low thermal conductivity of the lunar regolith generally makes lateral conduction negligible [2].

Third, add the defined Material Stack as insulation beneath the surface element. To do this edit the Insulation tab of the Thin Shell Data dialogue box, pictured in Figure 9.2.1-1. Choose to (1) place insulation beneath the surface, (2) define the insulation with a Multiple Materials (stack),

and (3) Calc type: “Based on material property.” The last option allows the thermal mass of the subsurface layers to be included in the calculations.[4]

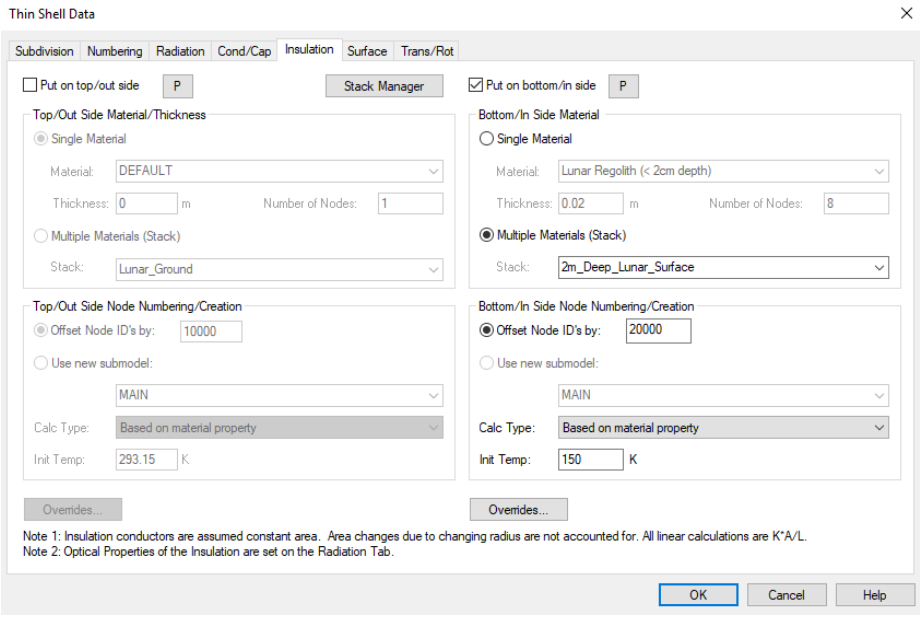

FIGURE 9.2.1-1: THIN SELL DIALOGUE BOX

Only the top surface of the top layer should be set to participate in the radiation calculations. This is so the surface does not exchange heat with the idealized planet TD constructs. A subsurface heat flux is applied to the bottom surface of the bottom layer. When insulation nodes are used, select the box “Put heat load into insulation nodes” when defining the heat load.

9.2.2 Boundary Conditions

In a solely radiative environment, were the surface radiates to deep space, the boundary condition at the surface $z = 0$ is:

$$-k\frac{\partial T}{\partial z} = \alpha\, S_O \cos(\theta_z) + \varepsilon\sigma\left(T_{space}^4 - T_m^4\right)$$

where $S_O$is the solar flux(see section 4.1), θ_z is the solar zenith angle, α is the ground absorptivity (in the solar spectrum), ε is the ground emissivity (in the infrared spectrum), σ is the Stefan-Boltzmann constant ($= 5.6704 * 10^{-8}\left[\frac{W}{m^2K^4}\right]$), T_m is the Moon’s surface temperature, and T_{space} is the temperature of deep space (about 3K).

The boundary condition at $z = d$ is:

$$k\frac{\partial T}{\partial z} = q"_{sub}$$

[4] Note: Insulation is assumed to be constant area, for curved surfaces as the depth increases the area decreases slightly, this could introduce some error in the model.

where $q"_{sub}$ is the subsurface heat flux (see section 5.4). Ochoa et al. approximates q_{sub} as 0 to simplify the analysis [1]. This is because in some locations (e.g. equatorial) the subsurface heat flux has negligible impact on the surface temperature.

9.2.3 Discretization

In general, a finite difference model of the lunar surface needs to only include the upper portion of Moon's regolith layer. DSNE 3.4.2.1 describes the Moon's subsurface structure. The regolith layer ranges between roughly 3 to 15 m in thickness, depending on the location. However, it is sufficient to set the thickness such the deepest layer is unaffected by the Moon's cyclic environment, or any surface operations (e.g. drilling) [3]. The required thickness may be able to be estimated by running a model where the lunar surface is represented with simple geometric shapes. Often thickness between 0.6 - 3 m are used, with deeper thicknesses used at the poles and in permanently shadowed regions [3,1,6,7,2,8]. At the Apollo 15 and 17 landing sites, 1 m deep should be sufficient since, yearly temperature fluctuations are < 0.01 K [9].

Since the top layer of the lunar surface responds much quicker than the deeper layers (see section 9.0), it is common to have the thickness of each subsurface layer increase with depth. For example, Christie et al. placed divided the layers at: 0 m, 0.01 m, 0.02 m, 0.13 m, 0.25 m, 0.39 m, and 0.62 m [6]. Hager's TherMoS™ model divided layers such that nodes were located at 0.00027 m, 0.00067 m, 0.0018 m, 0.005 m, 0.0135 m, 0.0366 m, 0.0996 m, 0.2707 m, 0.7358 m, and 2 m (a logarithmic increase in spacing) [2]. The increased spacing with each layer reflects how the density increases exponentially with depth.

Ideally, in plane discretization (e.g. horizontal) should be tight enough to capture significant interactions between the lunar surface and the vehicle. For example, hot spots could be created by sunlight reflecting from the vehicle to the lunar surface and back. To reduce model run time, a common technique is to have a highly discretized region near the vehicle and a less dense region further from the vehicle [1,,610]. Garsbarre et al.'s parametric method describes how choose the size of the highly discretized region.

9.2.4 Initial Conditions Cyclic Steady State

Before a transient thermal analysis is performed on the lunar surface, initial conditions of the lunar surface and subsurface layers must be determined. This can be done by first running the lunar surface model to a *cyclic steady state*. At cyclic steady state, surface and subsurface temperatures for each repeated point in the lunar cycle are the same. The lunar diurnal (day-night) cycle is 29.5 Earth days, and a lunar year is 354 Earth days [3]. In locations with little seasonal variation, such as the Apollo landing sites, cyclic steady state can be determined with respect to the diurnal cycle.

The time to reach cyclic steady state varies based on the location, layer thickness, and layer discretization. Since the density increases with depth (section 6.3), it takes longer for deeper layers to reach steady state. Temperatures at the deepest layer should approach a constant value (section 9.2.3).

To give an idea of how long it may take for a model to reach cyclic steady state, a flat 1 m^2 section of lunar regolith at -85.393N was modeled in Thermal Desktop. The square was made of 9 layers

of thicknesses given in Table 9.2.4-1. A heat flux of 0.018 W/m^2 was applied at the bottom of the bottom layer to account for subsurface heat flow.

TABLE 9.2.4-1 DEPTH VS. DENSITIES IN EXAMPLE MODEL

Layer	Depths [m]	Density [kg/m^3]
1	0 - 0.001	1105.122
2	0.001 - 0.02	1198.203
3	0.02 - 0.04	1348.08
4	0.04 - 0.08	1506.14
5	0.08 - 0.16	1673.101
6	0.16 - 0.32	1774.401
7	0.32 - 0.64	1798.667
8	0.064 - 1.28	1799.994
9	1.28 – 2.00	1800

Figure 9.2.4-1 shows how long it takes the square to reach cyclic state for two cases. Case 1: all layers start at 298 K. Case 2: layer 1 starts at 298 K, while layers 2 - 9 are start at 150 K. At the surface, cyclic steady state is reached within 5 years. The subsurface temperatures take much longer to reach cyclic steady state. However, providing a better initial guess for subsurface temperatures shortens this time. For example, for layer 9 takes 80 Earth years to be <0.5 K of steady sate for Case 1, but only requires 50 Earth years for Case 2. Table 9.2.4-2 shows Case 2's change in yearly maximum and minimum temperatures at 2, 10, 50, 80, and 100 Earth years. This model took little very little time to run. Similar simulations may be useful for choosing starting temperatures for runs that calculate a lunar surface thermal model's initial conditions.

Depending on the application, an analyst can decide what is considered to be close enough to cyclic steady state. Christi et al.'s lunar surface model was ran for ~7.5 earth years to obtain its initial condidions [6]. Paige et al's lunar surface model was initially ran for ~6 years, to obtain better starting temperatures, then another 6 years to obtain its initial conditions [7].

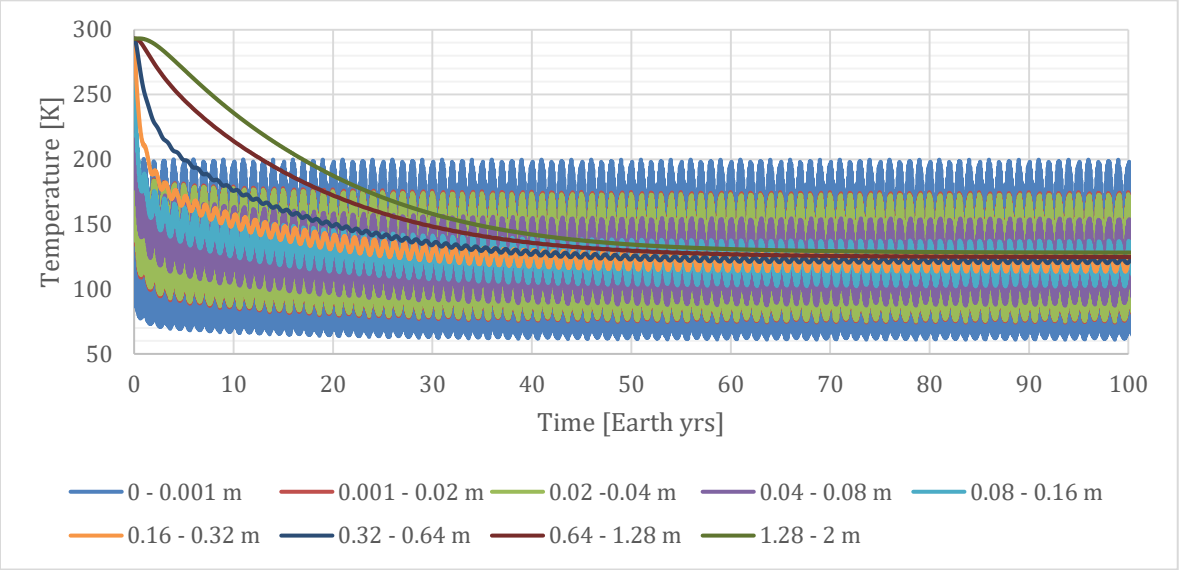

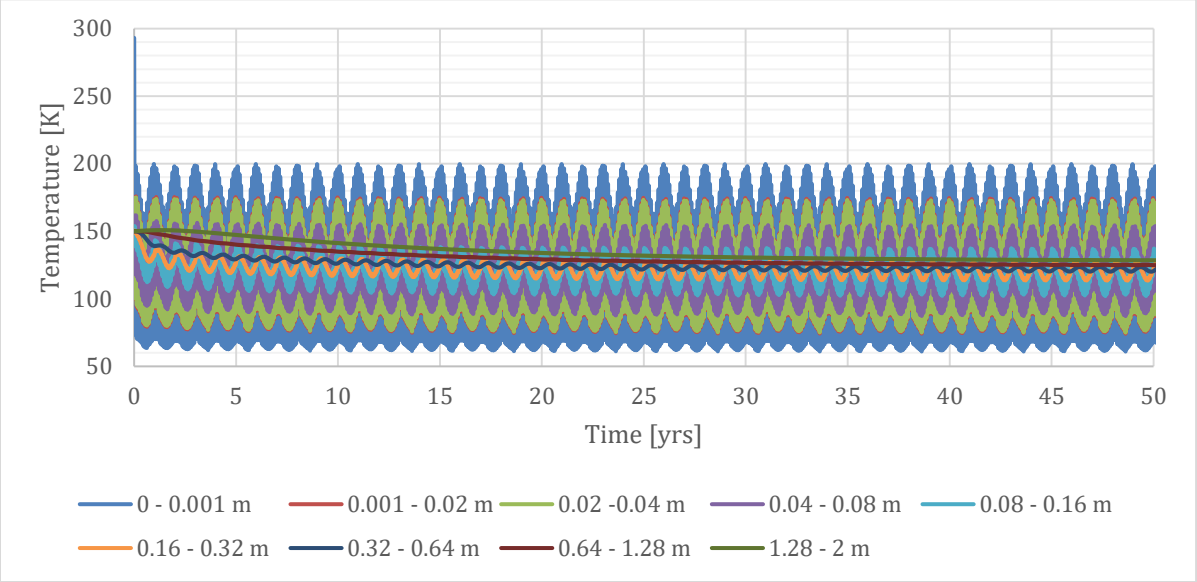

FIGURE 9.2.4-1: PREDICTED LUNAR SURFACE AND SUBSURFACE TEMPERATURES FOR A 1 M^2 SECTION AT -85.393N LATITUDE REACHING CYCLIC STEADY STATE. (TOP) CASE 1: ALL LAYERS START AT 298K. (BOTTOM) CASE 2: LAYER 1 STARTS AT 298K AND LAYERS 2 - 9 START AT 150K.

TABLE 9.2.4-2 COMPARISON OF MAXIMUM AND MINIMUM SURFACE AND SUBSURFACE TEMPERATURES FOR A 1 M^2 SECTION AT -85.393N LATITUDE UP TO 100 YEARS FOR CASE 2.

time, [yrs]	2		10		50		80		100	
depth [m]	T max [K]	T min [K]	T max [K]	T min [K]	T max [K]	T min [K]	T max [K]	T min [K]	T max [K]	T min [K]
0 - 0.001	198.532	62.694	199.72	61.50	199.70	61.28	199.70	61.26	199.70	61.26
0.001 - 0.02	174.869	77.362	172.78	75.08	172.38	74.66	172.37	74.63	172.36	74.62
0.02 - 0.04	173.569	78.325	171.62	75.97	171.20	75.54	171.18	75.50	171.17	75.50
0.04 - 0.08	154.949	91.901	154.73	88.53	153.81	87.91	153.78	87.86	153.77	87.86
0.08 - 0.16	141.063	106.962	138.88	103.39	137.17	102.50	137.11	102.43	137.11	102.42
0.16 - 0.32	134.006	120.736	129.79	114.91	126.73	113.56	126.62	113.44	126.61	113.44
0.32 - 0.64	135.820	131.669	128.93	122.41	123.48	120.13	123.29	119.95	123.28	119.93
0.064 - 1.28	145.693	143.398	134.92	128.82	125.13	124.89	124.80	124.55	124.78	124.52
1.28 – 2.00	150.620	149.782	141.26	133.49	128.51	128.47	128.06	128.05	128.04	128.02

References:

[1] D. A. Ochoa, B. M. Miranda, B. C. Conger, and L. A. Trevino, “Lunar EVA Thermal Environment Challenges,” *SAE Transactions*, vol. 115, pp. 492–505, 2006.

[2] P. B. Hager, “Dynamic thermal modeling for moving objects on the Moon,” Technische Universität München, Germany, 2013.

[3] A. Vasavada, D. Paige, and S. Wood, “Near-Surface Temperatures on Mercury and the Moon and the Stability of Polar Ice Deposits,” *Icarus*, vol. 141, no. 2, pp. 179–193, Oct. 1999.

[4] D. G. Gilmore, and R Collins. “Thermal Design Analysis.” Chapter 15, *Spacecraft Thermal Control Handbook*, 2nd ed. El Segundo, Calif. : Reston, Va.: Aerospace Press ; American Institute of Aeronautics and Astronautics, 2002.

[5] P. O. Hayne *et al.*, “Global Regolith Thermophysical Properties of the Moon from the Diviner Lunar Radiometer Experiment: Lunar Regolith Thermophysical Properties,” *J. Geophys. Res. Planets*, vol. 122, no. 12, pp. 2371–2400, Dec. 2017.

[6] R. Christie, D. Plachta, and M. Hasan, “Transient Thermal Model and Analysis of the Lunar Surface and Regolith for Cryogenic Fluid Storage,” Aug. 2008.

[7] D. A. Paige *et al.*, “Diviner Lunar Radiometer Observations of Cold Traps in the Moon’s South Polar Region,” *Science*, vol. 330, no. 6003, pp. 479–482, Oct. 2010.

[8] T. J. Warren, O. King, N. E. Bowles, E. Sefton-Nash, R. Fisackerly, and R. Trautner, “The Oxford 3D Thermophysical Model with Application to the Lunar PROSPECT Mission,” *Lunar and Planetary Science Conference*, p. 2040, Mar. 2019.

[9] S. Nagihara, W. S. Kiefer, P. T. Taylor, D. R. Williams, and Y. Nakamura, “Examination of the Long-Term Subsurface Warming Observed at the Apollo 15 and 17 Sites Utilizing the Newly Restored Heat Flow Experiment Data From 1975 to 1977,” *Journal of Geophysical Research: Planets*, vol. 123, no. 5, pp. 1125–1139, May 2018.

[10] J. F. Gasbarre, R. M. Amundsen, S. Scola, F. B. Leahy, and J. R. Sharp, “Ground Plane and Near-Surface Thermal Analysis for NASA’s Constellation Programs,” p. 13, 2008.

9.3 SELECTING TERRAIN SIZE

When modeling a vehicle on the lunar surface, the size of the terrain to include in the model should be determined by considering: 1) the vehicle’s view of the lunar surface, and 2) potential solar blockage from surface features that either shade the vehicle or the surface near it. In addition to the techniques described in this section, parametric analysis, like the one Gasbarre et al.’s study can be useful for sizing terrain [1].

9.3.1 Sizing Ground Plane

The exchange of radiant energy between an object and the lunar ground plane may be characterized through the use of configuration factors. Configuration factors, also known as view factors, are defined as the fraction of radiant energy leaving a surface that is incident upon a second surface. For certain idealized geometries, closed form mathematical expressions exist for configuration factors. These expressions, along with summation rules and reciprocity relations, allow for an estimation of the radiant heat transfer interaction between a spacecraft and the lunar ground plane. For the guidelines presented in this document, the lunar ground plane has been modeled as an idealized planar surface for sizing purposes, i.e. the actual topography of the lunar surface is not considered. As such, the guidelines presented here will be highly conservative in nature. In addition, the nomenclature used is specific to a given section of this document and at times there is overlap. For this reason, particular attention should be given to the context in which guidelines are presented.

9.3.1.1 Radiant Energy: Ground Plane to Lander Exchange

To gain insight into the appropriate sizing for analysis purposes of the lunar ground plane, a lander was approximated as a coaxial cylinder displaced from the ground plane by a fixed distance. The fraction of the radiant energy incident upon the spacecraft from the ground plane, $F_{1-2,3}$, is given by

$$F_{1-2,3} = F_{1-2} + F_{1-3}$$

where F_{1-2} is the radiant energy incident upon the lower surface of the spacecraft from the ground plane and F_{1-3} is the radiant energy incident upon the outer sides of the spacecraft from the ground plane. F_{1-2} may be calculated using the following: (from [2])

$$F_{1-2} = \left(\frac{2RH_2}{1-R^2}\right)F_2 - \left(\frac{2RH_1}{1-R^2}\right)F_1$$

where $R = r_2/r_1$, $H_1 = L/r_1$, $H_2 = (h+L)/r_1$, $A = H^2 + R^2 - 1$, $B = H^2 - R^2 + 1$,

$$F_1 = \left(\frac{B_1}{8RH_1}\right) + \left(\frac{1}{2\pi}\right)\left\{\cos^{-1}\left(\frac{A_1}{B_1}\right) - \left(\frac{1}{2H_1}\right)\left[\frac{(A_1+2)^2}{R^2} - 4\right]^{1/2}\cos^{-1}\left(\frac{A_1 R}{B_1}\right) - \left(\frac{A_1}{2RH_1}\right)\sin^{-1}R\right\}$$

$$F_2 = \left(\frac{B_2}{8RH_2}\right) + \left(\frac{1}{2\pi}\right)\left\{\cos^{-1}\left(\frac{A_2}{B_2}\right) - \left(\frac{1}{2H_2}\right)\left[\frac{(A_2+2)^2}{R^2} - 4\right]^{1/2}\cos^{-1}\left(\frac{A_2 R}{B_2}\right) - \left(\frac{A_2}{2RH_2}\right)\sin^{-1}R\right\}$$

F_{1-3} may be calculated using [4]

$$F_{1-3} = \frac{1}{2}\left\{X - \left[X^2 - 4\left(\frac{R_3}{R_1}\right)^2\right]^{1/2}\right\}$$

where $R_1 = r_1/L$, $R_3 = r_2/L$, and

$$X = 1 + \frac{1+R_3^2}{R_1^2}$$

Figure 9.3.1.1-1 is a plot of the fraction of the radiant energy incident upon the lander from the ground plane ($F_{1-2,3}$) as a function of normalized ground plane radius for several lander aspect ratios. Five aspect ratios were chosen to give a broad representation of the entire range of potential lunar landers. A somewhat ad hoc decision was made to fix the lander radius at 2 m and the height of the lander above the lunar surface at 0.5 m. These values are on the same order of magnitude as many past/potential landers. As can be seen from the figure, $F_{1-2,3}$ decreases rapidly and by a normalized ground plane radius of 100 is effectively zero for all aspect ratios considered. On the other hand, $F_{1-2,3}$ is observed to be a weak function of aspect ratio.

A trend line was fitted to points corresponding to $F_{1-2,3} = 0.05$ (for all aspect ratios considered) and the associated normalized ground plane radius as a function of aspect ratio was found to be

$$(r_1/r_2)_{F_{1-2,3}=0.05} \cong 2.08ln(AR) + 7.34$$

with a coefficient of determination, R^2, of 0.996. For modeling purposes, selecting a ground plane radius corresponding to a configuration factor > 99.7% of the asymptotic limit is recommended for a given aspect ratio so that the radiant energy from the ground plane to the lander may be taken as negligible.

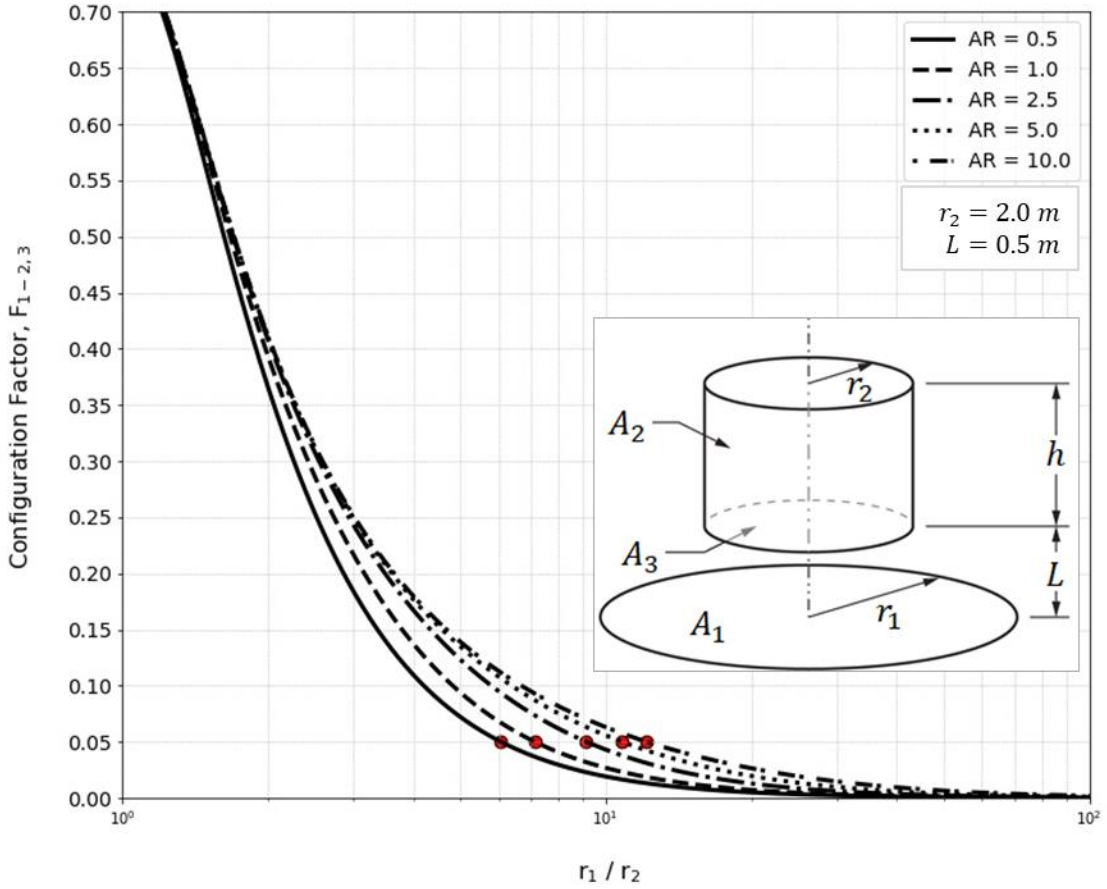

FIGURE 9.3.1.1-1: CONFIGURATION FACTOR ($F_{1-2,3}$) FOR THE GROUND PLANE TO THE EXTERNAL SURFACE OF A CYLINDER, OF HEIGHT h, RADIUS r_2, AND DISPLACED A DISTANCE L FROM THE GROUND PLANE, AS A FUNCTION OF NORMALIZE GROUND PLANE RADIUS (r_1/r_2) AND ASPECT RATIO ($AR = h/2r_2$). LOCATION OF 5% DELTA FROM $r_1/r_2 \rightarrow \infty$ ASYMPTOTIC CONFIGURATION FACTOR VALUE INDICATED AS RED DATA POINTS.

9.3.1.2 Radiant Energy: Lander to Ground Plane Exchange

The radiant energy leaving both the bottom and outer sides of a lander that is incident on the ground plane may be found using a reciprocity relationship, i.e.

$$A_1 F_{1-2,3} = A_2 F_{2,3-1}$$

Figure 9.3.1.2-1 is a plot of the radiant energy leaving by the lander bottom and outer sides that is incident upon the ground plane as a function of the lander aspect ratio, i.e. $F_{2,3-1}$. Not shown on the figure is the individual contributions from the bottom of the lander (F_{3-1}) and the sides of the lander (F_{2-1}). F_{3-1} asymptotically approaches a value of one for a normalized ground plane radius of greater than ten (10) for all aspect ratios considered. As expected, F_{2-1} tracks closely with $F_{2,3-1}$ for all cases considered. From the figure, one can see that the respective values of the

configuration factor asymptotically converges to a constant as $r_1/r_2 \to \infty$ and this constant is a function of the lander aspect ratio. A trend line was fitted to points corresponding to

$$\left|\left(F_{2,3-1}\right)_{r_1/r_2\to\infty} - F_{2,3-1}\right| = 0.05$$

for all aspect ratios considered and the associated normalized ground plane radius as a function of aspect ratio was found to be

$$(r_1/r_2)_{\Delta 5\%} \cong 12.65(AR) + 0.286$$

with a coefficient of determination, R^2, of 1.000. For modeling purposes, selecting a ground plane radius corresponding to a configuration factor > 99.7% of the asymptotic limit is recommended for a given aspect ratio so that the radiant energy from the lander bottom and outer sides to the ground plane may be taken as negligible.

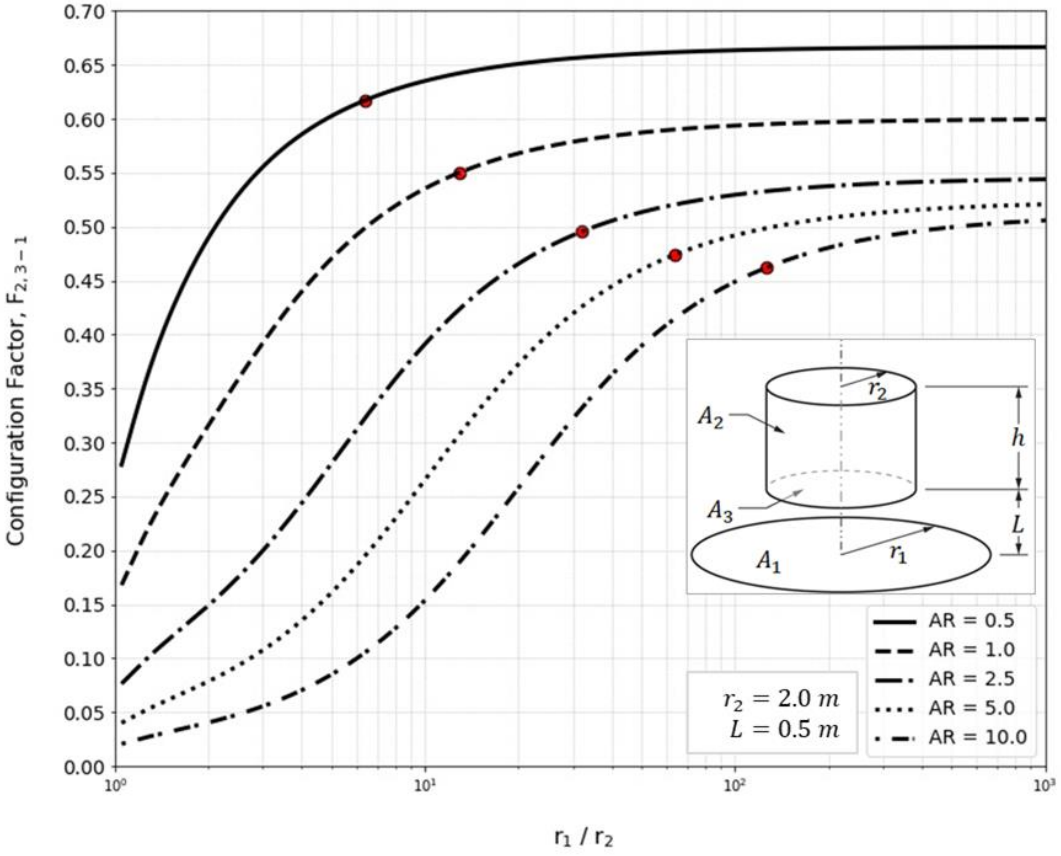

FIGURE 9.3.1.2-1: CONFIGURATION FACTOR ($F_{2,3-1}$) FOR THE EXTERNAL SURFACE OF A CYLINDER, OF HEIGHT h, RADIUS r_2, AND DISPLACED A DISTANCE L FROM THE GROUND PLANE, TO THE GROUND PLANE AS A FUNCTION OF NORMALIZE GROUND PLANE RADIUS (r_1/r_2) AND ASPECT RATIO ($AR = h/2r_2$). LOCATION OF 5% DELTA FROM $r_1/r_2 \to \infty$ ASYMPTOTIC CONFIGURATION FACTOR VALUE INDICATED AS RED DATA POINTS.

9.3.1.3 Radiant Energy: Cylinder to Ground Plane Exchange

Situations may exist where the object is not displaced from the ground plane (for example, thermal radiation heat transfer to or from an astronaut or a vertical structure). For these situations, the configuration factor from the object (assuming the object is a cylinder) to the ground plane may be found using (Sparrow, et al. 1962)

$$F_{1-2} = \frac{B}{8RH} + \frac{1}{2\pi}\left\{\cos^{-1}\left(\frac{A}{B}\right) - \frac{1}{2H}\left[\frac{(A+2)^2}{R^2} - 4\right]^{1/2}\cos^{-1}\left(\frac{AR}{B}\right) - \frac{A}{2RH}\sin^{-1}R\right\}$$

where $R = r_1/r_2$, $H = h/r_2$, $A = H^2 + R^2 - 1$, and $B = H^2 - R^2 + 1$. The above corresponds to the configuration factor for the outer surface of a cylinder of radius r_1 to an annular disk of radius r_2 at one end of the cylinder.

Figure 9.3.1.3-1 is a plot of the radiant energy leaving the outer sides of a cylinder that is incident upon the ground plane as a function of normalized ground plane radius for several cylinder aspect ratios. As with the prior case, five aspect ratios were chosen to give a broad representation of the entire range of potential situations. The minimum aspect ratio was chosen to ensure that the configuration factor associated with radiant exchange for a notional astronaut would be included. For American females and males, height (stature) ranges from 148.6 cm to 194.6 cm while the minimum forearm-forearm breadth width ranges from 38.9 cm to 66.0 cm (Liskowsky and Seitz, 2014). If a standing human is modeled as a finite length cylinder and if the aspect ratio of this cylinder is defined as the height divided by diameter, then for American males and females (shirt sleeve conditions), the aspect ratio ranges from 2.9 to 3.8. This is well within the range of aspect ratios considered and it was assumed that astronauts wearing spacesuits would also have similar aspect ratios. On the other hand, the largest aspect ratio ($AR = 50$) for a 0.25 m radius corresponds to a 25 m cylinder height.

As expected, the respective values of the configuration factor asymptotically converges to a constant value of 0.5 as $r_2/r_1 \to \infty$ as a function of aspect ratio. A trend line was fitted to points corresponding to

$$\left|(F_{1-2})_{\,r_2/r_1\to\infty} - F_{1-2}\right| = 0.05$$

for all aspect ratios considered and the associated normalized ground plane radius as a function of aspect ratio was found to be

$$(r_2/r_1)_{\Delta 5\%} \cong 12.63(AR) + 0.943$$

with a coefficient of determination, R^2, of 1.000. For modeling purposes, selecting a ground plane radius corresponding to a configuration factor > 99.7% of the asymptotic limit is recommended for a given aspect ratio so that the radiant energy from the outer sides of the cylinder to the ground plane may be taken as negligible.

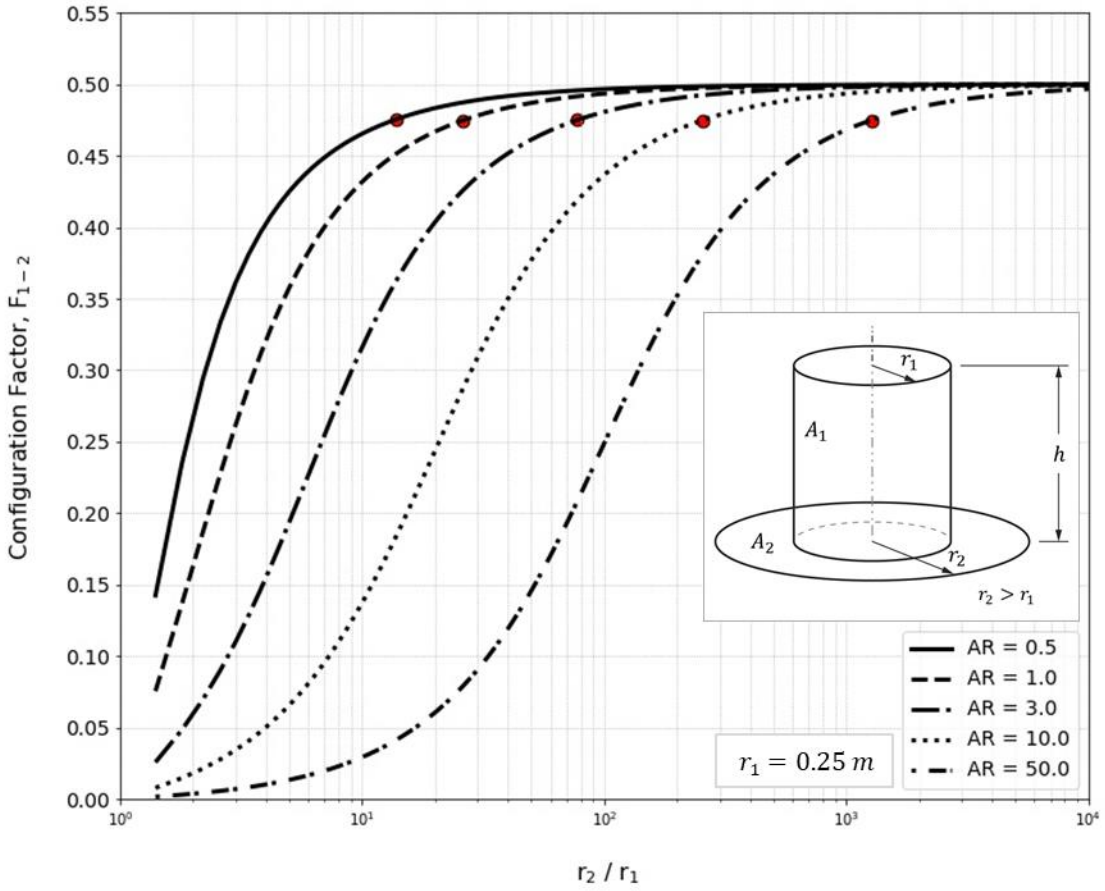

FIGURE 9.3.1.3-1: CONFIGURATION FACTOR (F_{1-2}) FOR THE EXTERNAL SURFACE OF A CYLINDER, OF HEIGHT h, TO THE ANNULAR SURFACE OF THE GROUND PLANE AS A FUNCTION OF NORMALIZE GROUND PLANE RADIUS (r_2/r_1) AND ASPECT RATIO ($AR = h/2r_1$). LOCATION OF 5% DELTA FROM $r_2/r_1 \rightarrow \infty$ ASYMPTOTIC CONFIGURATION FACTOR VALUE INDICATED AS RED DATA POINTS

9.3.1.4 Radiant Energy: Ground Plane to Cylinder Exchange

The radiant energy leaving the annular surface of the ground plane that is incident on the outer sides of the cylinder may be found using a reciprocity relationship, i.e.

$$A_1 F_{1-2} = A_2 F_{2-1}$$

Figure 9.3.1.4-1 is a plot of the fraction of the radiant energy incident upon a cylinder from the ground plane (F_{2-1}) as a function of normalized ground plane radius for several cylinder aspect ratios. The same aspect ratios as used for the cylinder to ground plane configuration factor were used for this case. As can be seen from the figure, F_{2-1} decreases rapidly and by a normalized ground plane radius of 100 is effectively zero for all aspect ratios considered.

A trend line was fitted to points corresponding to $F_{1-2,3} = 0.05$ (for all aspect ratios considered) and the associated normalized ground plane radius as a function of aspect ratio was found to be

$$(r_1/r_2)_{F_{2-1}=0.05} \cong 1.77ln(AR) + 5.85$$

with a coefficient of determination, R^2, of 0.944. For modeling purposes, selecting a ground plane radius corresponding to a configuration factor > 99.7% of the asymptotic limit is recommended for a given aspect ratio so that the radiant energy from the ground plane to the vertical cylinder may be taken as negligible.

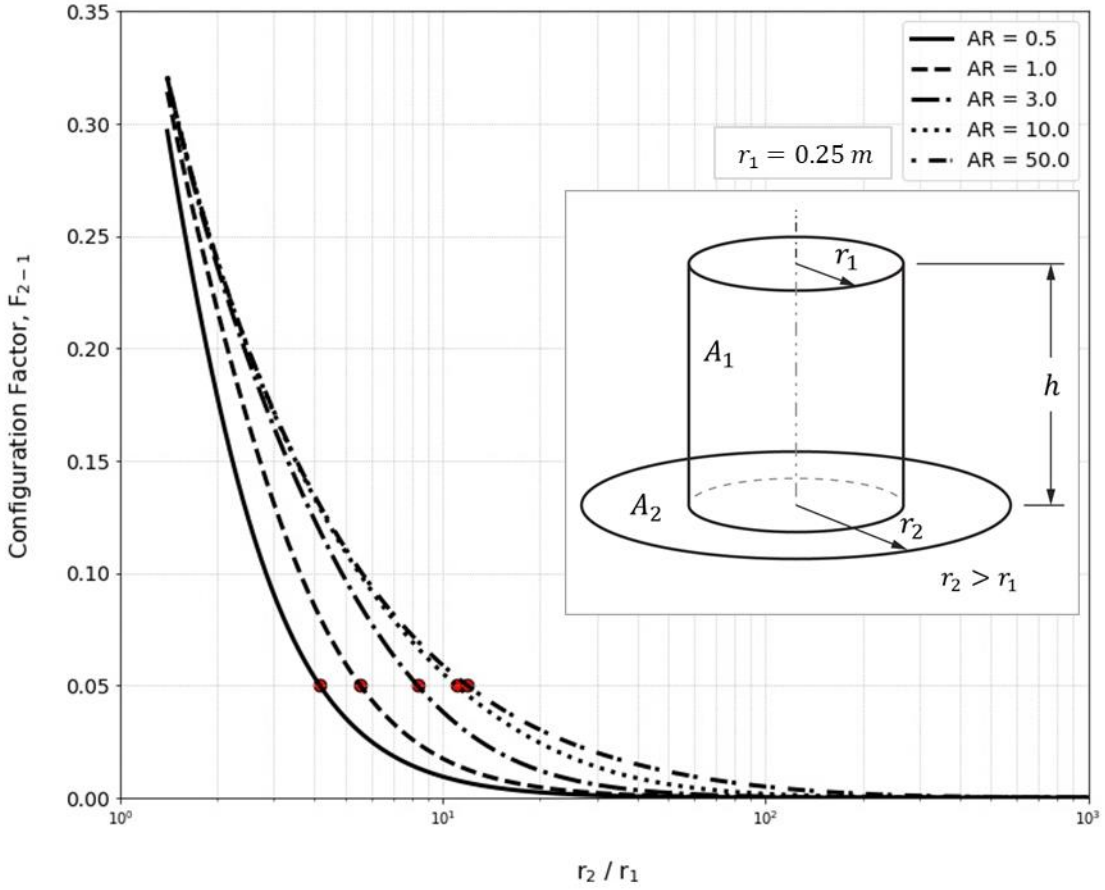

FIGURE 9.3.1.4-1: CONFIGURATION FACTOR (F_{2-1}) FOR THE ANNULAR SURFACE OF THE GROUND PLANE TO THE EXTERNAL SURFACE OF A CYLINDER, OF HEIGHT h, AS A FUNCTION OF NORMALIZE GROUND PLANE RADIUS (r_2/r_1) AND ASPECT RATIO ($AR = h/2r_2$). LOCATION OF 5% DELTA FROM $r_2/r_1 \to \infty$ ASYMPTOTIC CONFIGURATION FACTOR VALUE INDICATED AS RED DATA POINTS.

9.3.1.5 Radiant Energy: Sphere Located at a Fixed Distance above the Ground Plane to the Ground Plane

In the following section, a comparison of configuration factors will be used to estimate the altitude where the curvature of the Moon need no longer be a consideration. For altitude where the idealized lunar surface may be treated as a planar disk, the configuration factor from a spacecraft (represented here as a sphere) and the ground plane (the planar disk) may be found using [3]

$$F_{1-2} = \frac{1}{2}\left[1 - \frac{1}{(1+X^2)^{1/2}}\right]$$

where $X = r_2/h$.

Figure 9.3.1.5-1 provides a plot of the configuration factor variation as a function of the normalized ground plane radius (r_2/h). An altitude of 100 m was used to generate the values shown in the plot. As expected, as the normalized ground plane radius $(r_2/h) \to \infty$, the configuration factor asymptotically approaches a constant value of 0.5. A delta of less than 5% between the calculated configuration factor and the asymptotic configuration factor is achieved for values of $r_2/h > 9.95$ (shown as a red data point on the figure) while a 5% percent difference, defined as

$$\frac{\left|(F_{1-2})_{\,r_2/h\to\infty} - F_{1-2}\right|}{(F_{1-2})_{\,r_2/h\to\infty}} = 0.05$$

is achieved for values of $r_2/h > 20.0$ (this value is not show in the figure). Depending upon the level of accuracy desired, these values should provide guidance when determining the radius of the ground plane above which negligible error can be expected.

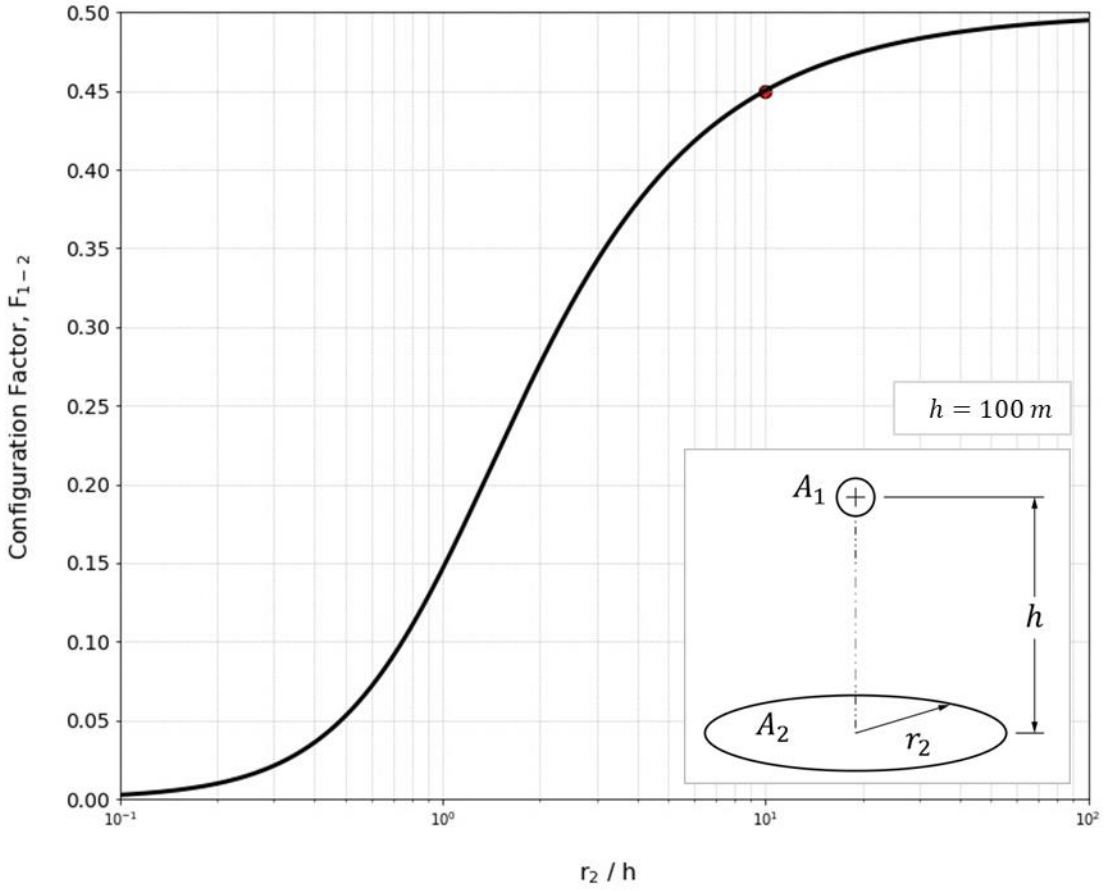

FIGURE 9.3.1.5-1: CONFIGURATION FACTOR (F_{1-2}) FOR THE EXTERNAL SURFACE OF A SPHERE, AT A DISTANCE h ABOVE THE SURFACE OF THE GROUND PLANE, TO THE GROUND PLANE AS A FUNCTION OF NORMALIZE GROUND PLANE RADIUS (r_2/h). LOCATION OF 5% DELTA FROM $r_2/h \rightarrow \infty$ ASYMPTOTIC CONFIGURATION FACTOR VALUE INDICATED AS RED DATA POINTS.

9.3.1.6 Radiant Energy: Ground Plane to a Sphere Located at a Fixed Distance above the Ground Plane

The radiant energy leaving the ground plane that is incident upon a sphere located at a fixed distance above the ground plane may be found using a reciprocity relationship, i.e.

$$A_1 F_{1-2} = A_2 F_{2-1}$$

For the purposes of calculation, a unit sphere was used to determine F_{2-1}. Note that $F_{2-1}$is a decreasing function of altitude. No figure is provided for this case as it was determined that above an altitude of 1 m, F_{2-1} is always less than 0.05.

9.3.1.7 Radiant Energy: A Domed Structure to the Ground Plane

To gain insight into the radiant transfer between notional hemispherical lunar habitats and the ground plane, the configuration factor between the outer surface of a hemisphere of radius r_1 and a concentric equatorial disk of radius r_2 (where $r_2 > r_1$) was used. This configuration factor is calculated using [5]

$$F_{1-2} = \frac{1}{4} - \frac{1}{2\pi}[X - (X^2 - 1)\sin^{-1}(R)]$$

where $R = r_1/r_2$ and $X = \sqrt{(1/R^2) - 1}$.

Figure 9.3.1.7-1 is a plot of the above configuration factor as a function of normalized ground plane radius. For the calculations, a value of 5.5 m was assumed as the radius for the hemisphere. This was motivated by the fact that the HI-SEAS Habitat (HI-SEAS, 2019) is a geodesic dome that is approximately 10.97 m in diameter. As can be seen in the figure, the F_{1-2} approaches a value of 0.25 as the normalized ground plane radius $(r_2/r_1) \to \infty$. A delta of less than 5% is achieved for values of $r_2/r_1 > 4.27$ (shown as a red data point on the figure) while a 5% percent difference, defined as

$$\frac{\left|(F_{1-2})_{\,r_2/r_1\to\infty} - F_{1-2}\right|}{(F_{1-2})_{\,r_2/r_1\to\infty}} = 0.05$$

is achieved for values of $r_2/r_1 > 17.0$. Depending upon the level of accuracy desired, these values should provide guidance when determining the radius of the ground plane above which negligible error can be expected.

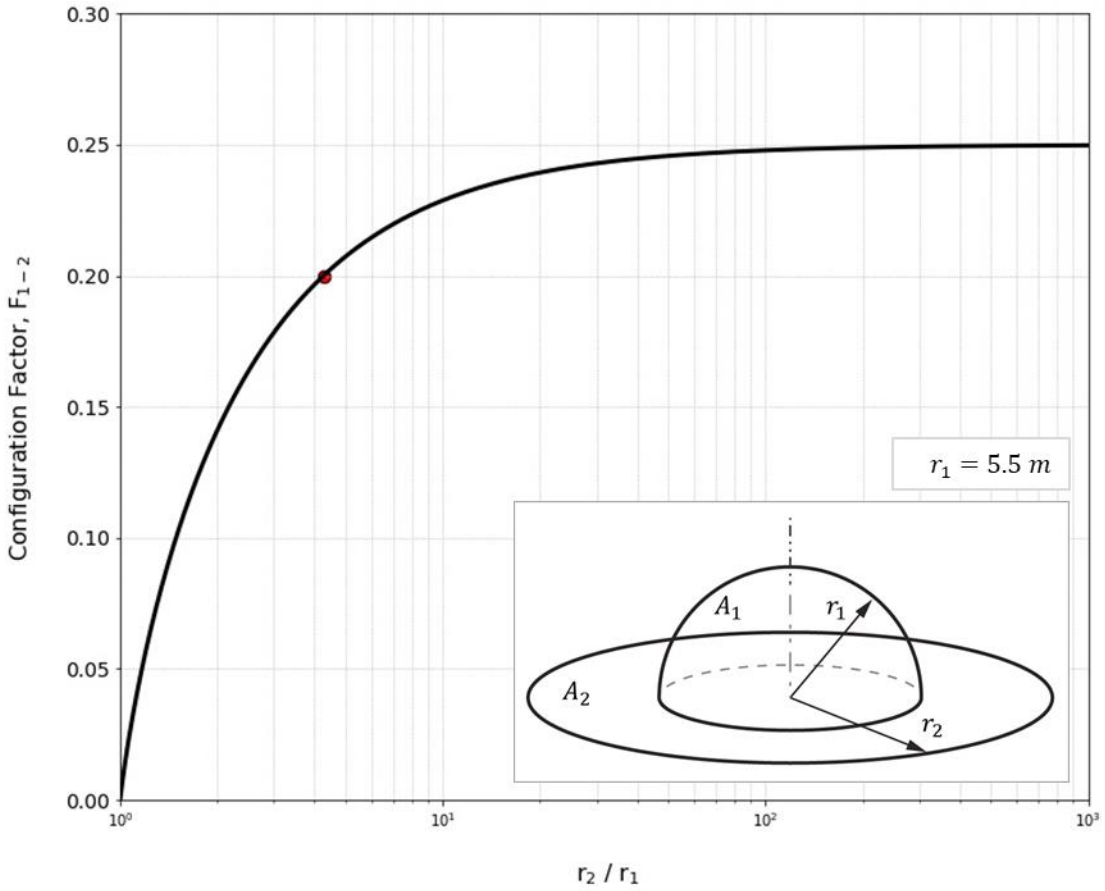

FIGURE 9.3.1.7-1: CONFIGURATION FACTOR (F_{1-2}) FOR THE EXTERNAL SURFACE OF A HEMISPHERICAL DOME, OF RADIUS r_1, TO THE ANNULAR GROUND PLANE AS A FUNCTION OF NORMALIZE GROUND PLANE RADIUS (r_2/r_1). LOCATION OF 5% DELTA FROM $r_2/r_1 \rightarrow \infty$ ASYMPTOTIC CONFIGURATION FACTOR VALUE INDICATED AS RED DATA POINTS.

9.3.1.8 Radiant Energy: Ground Plane to a Domed Structure

The radiant energy leaving the ground plane that is incident upon the outer surface of a hemisphere may be found using a reciprocity relationship, i.e.

$$A_1 F_{1-2} = A_2 F_{2-1}$$

Figure 9.3.1.8-1 is a plot of the above configuration factor as a function of normalized ground plane radius, i.e. r_2/r_1. As for the hemisphere to ground plane configuration factor, a value of 5.5 m was assumed as the radius for the hemisphere. From the figure it is clear that F_{1-2} is a monotonic decreasing function of normalized ground plane radius and approaches a value of zero as the normalized ground plane radius $(r_2/r_1) \rightarrow \infty$. A delta of less than 5% is achieved for values of $r_2/r_1 > 2.82$ (shown as a red data point on the figure). For modeling purposes, selecting a ground plane radius corresponding to a configuration factor > 99.7% of the asymptotic limit is

recommended for a given aspect ratio so that the radiant energy from the ground plane incident on the surface of the hemisphere may be taken as negligible.

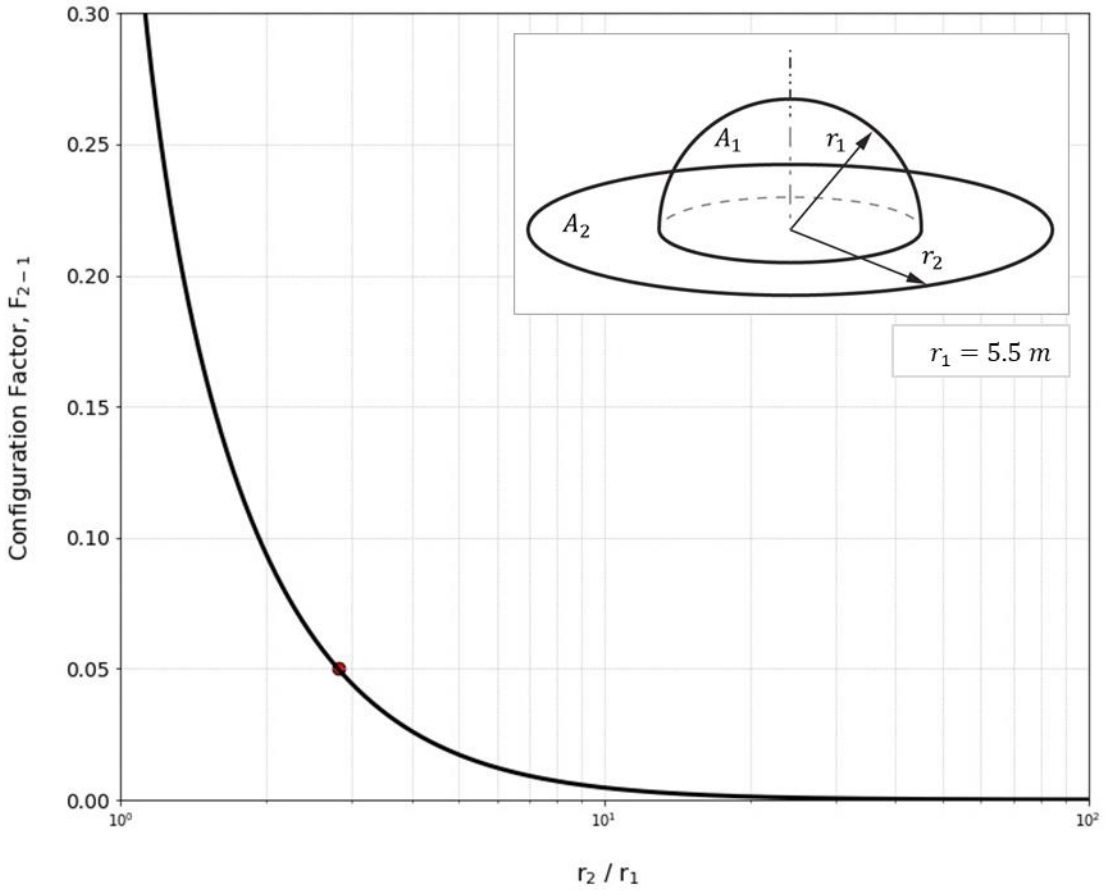

FIGURE 9.3.1.8-1: CONFIGURATION FACTOR (F_{2-1}) FOR THE ANNULAR GROUND PLANE TO THE EXTERNAL SURFACE OF A HEMISPHERICAL DOME, OF RADIUS r_1, AS A FUNCTION OF NORMALIZE GROUND PLANE RADIUS (r_2/r_1). LOCATION OF 5% DEVIATION FROM $r_2/r_1 \rightarrow \infty$ ASYMPTOTIC CONFIGURATION FACTOR VALUE INDICATED AS RED DATA POINTS.

9.3.2 Shadowing by Terrain Features

Simple geometry can be used to predict if a surface feature shadows a target location (e.g. a landing site). If the surface feature is near the target location, the Moon's curvature can be neglected. For example, the shadow length, L, from a boulder of height h, can be calculated as:

$$L = \frac{h}{\tan(\alpha)}$$

where α is the solar elevation angle. Then the height of the shaded region, y, a distance x away from the boulder can be calculated by using similar triangles:

$$\frac{y}{h} = \frac{L - x}{L}$$

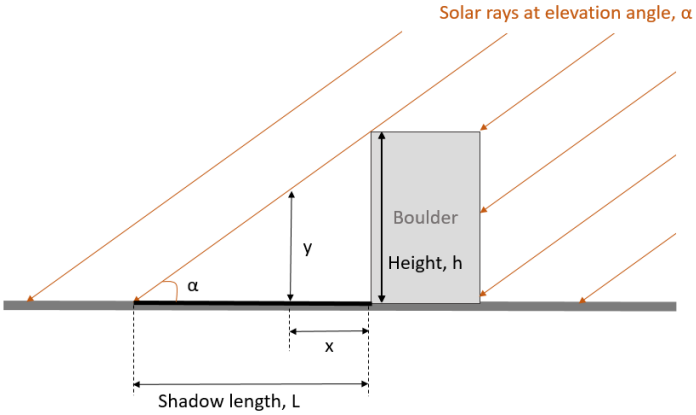

FIGURE 9.3.2-1: LENGTH OF SHADOW DUE TO A BOULDER

If the surface feature is very far away from the target location, then the Moon's curvature should not be neglected. This is because the Moon's curvature effectively reduces the height of the surface feature with respect to the target location. Consider a feature H tall in Figure 9.3.2-2, at location P_H and a target location at point P. A flat ground plane extends from P in all directions.

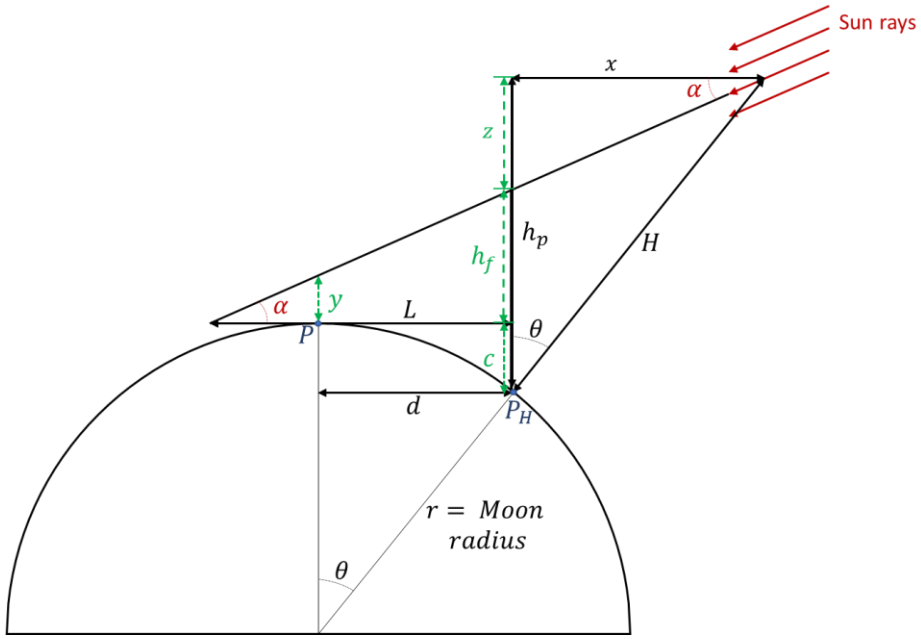

FIGURE 9.3.2-2: SHADOW LENGTH, L, FROM A LARGE OBJECT OF HEIGHT H ON A PERFECTLY SPHERICAL MOON, GIVEN A SOLAR ELEVATION ANGLE A AT POINT P. THE SCALE IS ADJUSTED FOR VISIBILITY.

The height of the feature projected on to a plane perpendicular to P's ground plane is:

$$h_p = H\,cos(\theta)$$

where θ is estimated as the difference between latitudes (to estimate maximum potential shading). This calculation assumes that the Moon is a perfect sphere. The effective height of the feature that shades P's ground plane is h_f and is calculated with using the following series of equations:

$$x = H\sin(\alpha)$$
$$z = x\tan(\alpha)$$

$$z = Hsin(\theta)\tan(\alpha)$$

$$c = r - rcos(\theta)$$

$$h_f = h_p - c - z$$

where r is the radius if the Moon. The distance between P and the feature along the ground plane is d and can be calculated as:

$$d = r\sin(\theta)$$

Knowing d and h_f, the shadow length L and height y can be calculated with the method that ignores surface curvature.

$$L = h_f/\tan(\alpha)$$

$$y = h_f\left(\frac{L-d}{L}\right)$$

If $y < 0$, then P is not shaded by the surface feature. If P was elevated above the ground plane at a height H_p then P would not be shaded if $y - H_p < 0$.

It is important to note that since sunlight is imperfectly collimated (±0.5°), this estimate can be improved by checking for shadowing from a range of elevation angles $0 < \alpha \leq \alpha_{max} + 0.5$. Shadowing is more likely at lower angles and for some thermal models a time in shadow may not be large enough to impact the results.

Using this process, the shadowing at a location on Shackleton's rim was estimated by surface features at two different locations, the results are shown in Table 9.3.2-1. In some scenarios the fraction of time in shadow may be small enough to neglect a surface feature in a thermal model.

TABLE 9.3.2-1: ESTIMATED SHADOWING FROM SURFACE FEATURES AT POINT P_H ON TO POINT P.

Case	P, Lon	P, Lat	P_H, Lon	P_H, Lat	H_P [m]	H [m]	Max α	Target shadowed?
1	203.844	-89.781	222.855	-89.439	1733.7	1954.4	1.77	if α < 1.04
2	203.844	-89.781	39.18366	-84.5533	1733.7	6688.8	1.77	no

9.4 SIMPLIFIED TERRAIN MODELING

9.4.1 Far Field Boundary Conditions and Lunar Curvature

The influence that the curvature of the lunar surface has on thermal analyses may be estimated by examining the difference between the configuration factor for a sphere radiating to an infinite plane and that of a small sphere radiating to a much larger sphere. For a sphere radiating to an infinite plane, the configuration factor is given as

$$F_{1-\infty} = 0.5$$

while the configuration factor for a small sphere radiating to a sphere with a much larger radius may be calculated using:

$$F_{1-2} = \frac{1}{2}\left(1 - \sqrt{1 - \frac{1}{h_{12}^2}}\right)$$

where $h_{12} = R_{12}/r_2$, $R_{12} \geq r_2$, and $r_2 \gg r_1$ [7]. Note that, for this case, the configuration factor F_{1-2} is not a function of the radius of the smaller sphere. From Figure 9.4.1-1, it may be seen that as the normalized altitude, i.e. $(R_{12} - r_2)/r_2$, approaches zero, the two configuration factors converge. At a normalized altitude of less than approximately 0.00125, the normalized difference between the two configuration factors, i.e. $(F_{1-2} - F_{1-\infty})/F_{1-\infty}$ has an absolute value of less than 5% and an idealized lunar surface may be considered, with marginal error, as a planar surface. Assuming that radius of the Moon is $1{,}737.1\ km$, this corresponds to an altitude of $2.171\ km$ above the lunar surface.

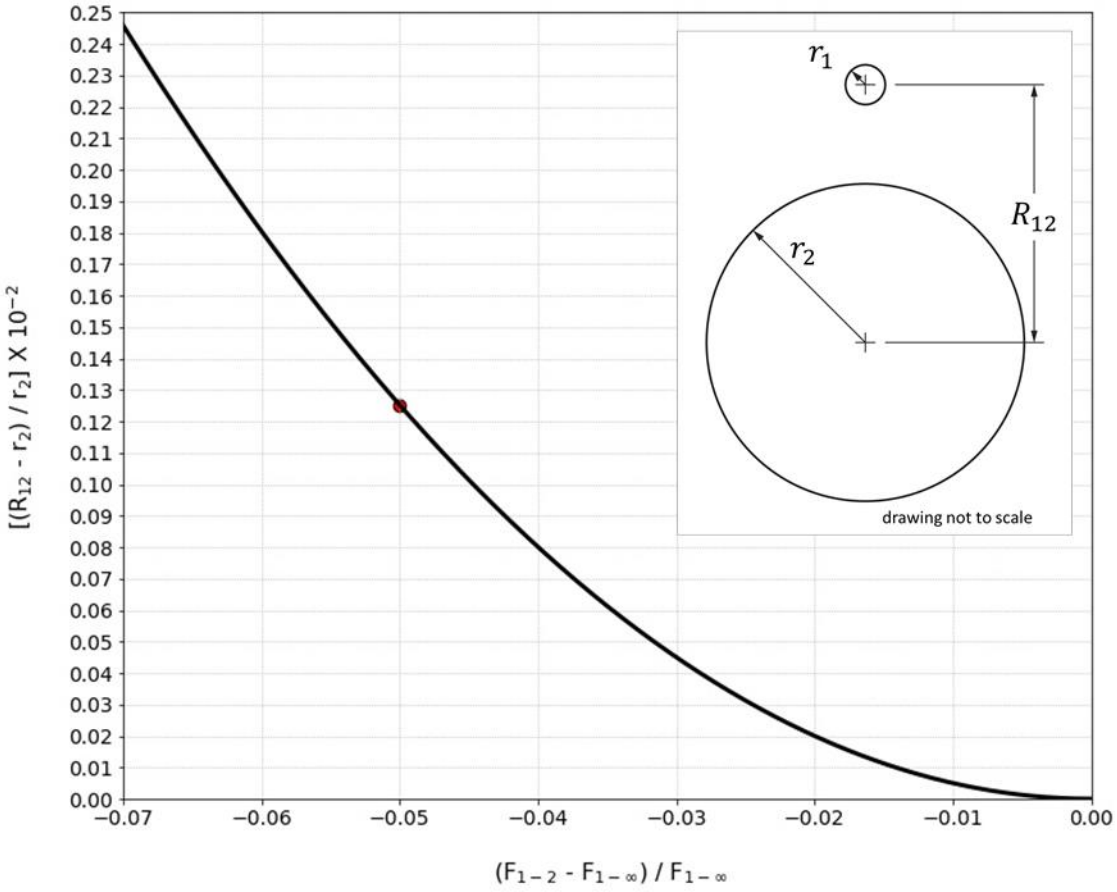

FIGURE 9.4.1-1: NORMALIZED ALTITUDE AS A FUNCTION OF THE NORMALIZED DIFFERENCE BETWEEN F_{1-2} AND $F_{1-\infty}$.

9.4.2 Simplified Flat Plane Comparison to DSNE

Depending on the problem statement, for some early modeling phases of a mission it may be sufficient to model the lunar surface using simple Thermal Desktop elements. One of the more simple methods is to use a flat plate. This plate will need to be sized and discretized correctly to capture heating rates on the lander, and shadowing effects on the surface. One can output this plate temperature versus time and compare it to the time changing values shown in DSNE Section 3.4.6.3. Described below is an example of using a flat plate to capture the noon time maximum temperature near the pole.

The goal of this example was to create a flat plate that captures the noon time maximum temperature near the pole in a transient model. This model was used to calculate heat fluxes into a cryogenic tank. A large discretized adiabatic flat plate was created as shown in Figure 9.4.2-1. The emissivity and absorptivity properties of this plate, and environmental solar flux, were set to the hot case values as described elsewhere in this document, which points to the DSNE values.

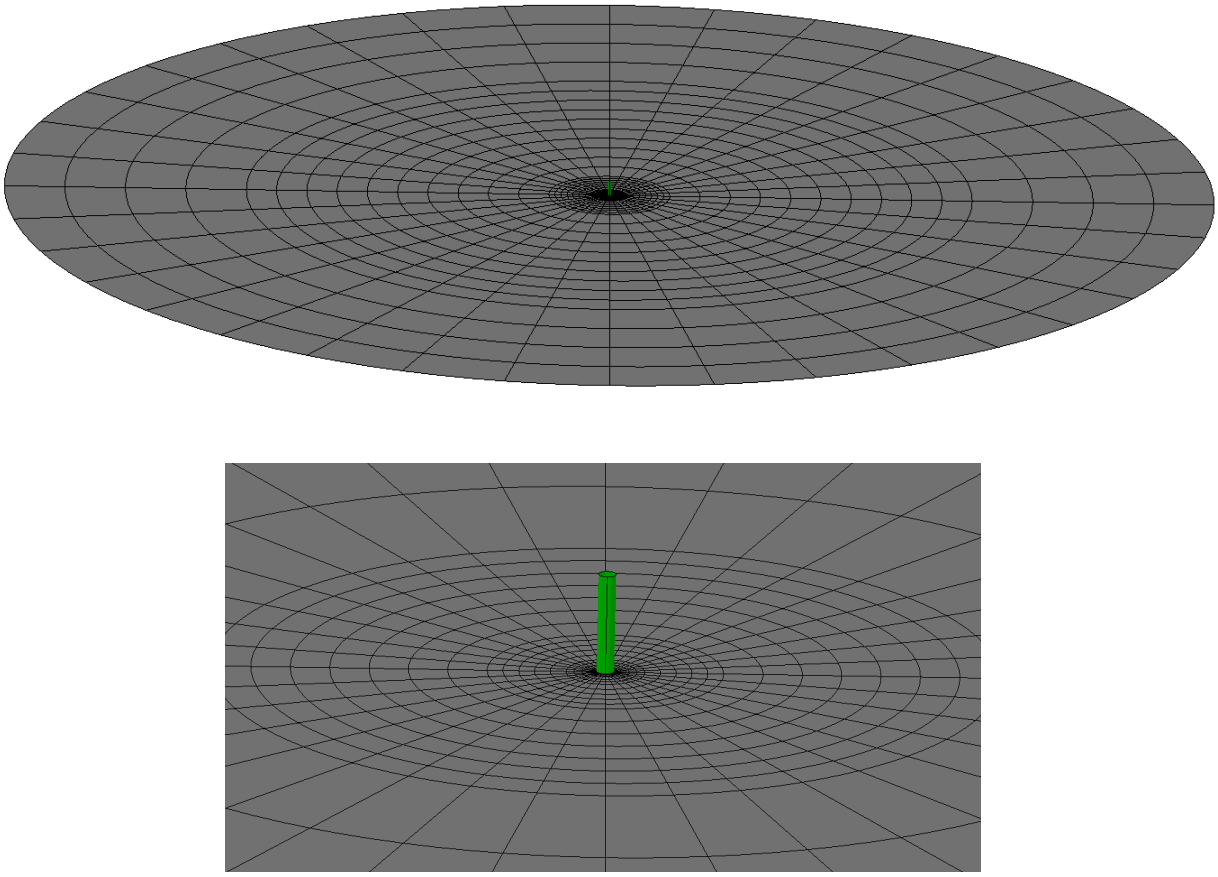

FIGURE 9.4.2-1: SIMPLE FLAT PLATE FOR SIMPLE ANALYSIS

In Section 3.4.6.3 of DSNE are figures from LRO DIVINER data for mean temperature and standard deviation for different latitudes on the Moon. The highest latitude given is 85°. This data can be compared to the simple flat plate in Thermal Desktop. Then the temperature of the flat plate be adjusted as needed for the problem statement.

Figure 9.4.2-2 shows the Thermal Desktop simple flat plate compared to extracted plot lines from the DSNE figures (through plot extraction, so not exact). The solid lines are the values pulled from DSNE, and the dotted lines are the Thermal Desktop surface results. Since the problem statement for this example was to model the hot case, the standard deviation line from the DSNE was only added to the mean. It can be seen as the standard deviation is added, the solid lines start to flatten out and form a plateau. The cause of this can be seen in the DSNE standard deviation plot, in that there are higher deviations in the morning and evening.

Adjusting the temperature of the Thermal Desktop flat plate was done by changing the latitude in the orbit manager, effectively “tilting” the model towards the Sun to increase the temperature. As shown here, in order to match the DSNE 2-sigma maximum value in Thermal Desktop the flat

plate was tilted by 9° (by setting the latitude in Orbit Manager to 76°). This maximum value is roughly 265K.

As can be seen from the figure, this setup of the simple flat plate model should not be used close to sunrise and sunset. The transient boundaries of this model were set within those bounds, then any results (i.e. heat loads into the tank) extracted from the model was done within an even tighter range to account for any initialization effects.

A quick check on the distribution of this 265 K 2-sigma hot value for 85° latitude on the lunar pole during lunar summer can be done using Quickmaps. As shown in Figure 9.4.2-3 from the contour plot, the 265 K value appears to be very well distributed across the lunar southern pole and not just isolated at the 85° line.

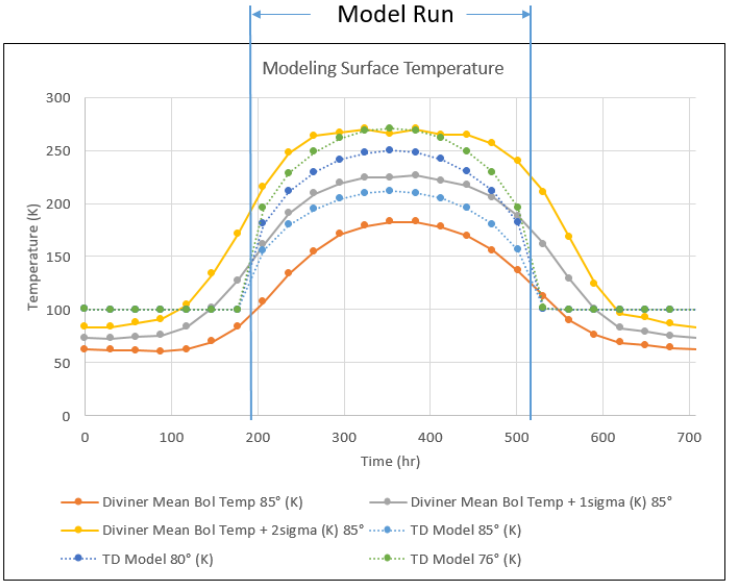

FIGURE 9.4.2-2: COMPARING AND ADJUSTING THERMAL DESKTOP SIMPLE FLAT PLATE TEMPERATURE TO DSNE DATA

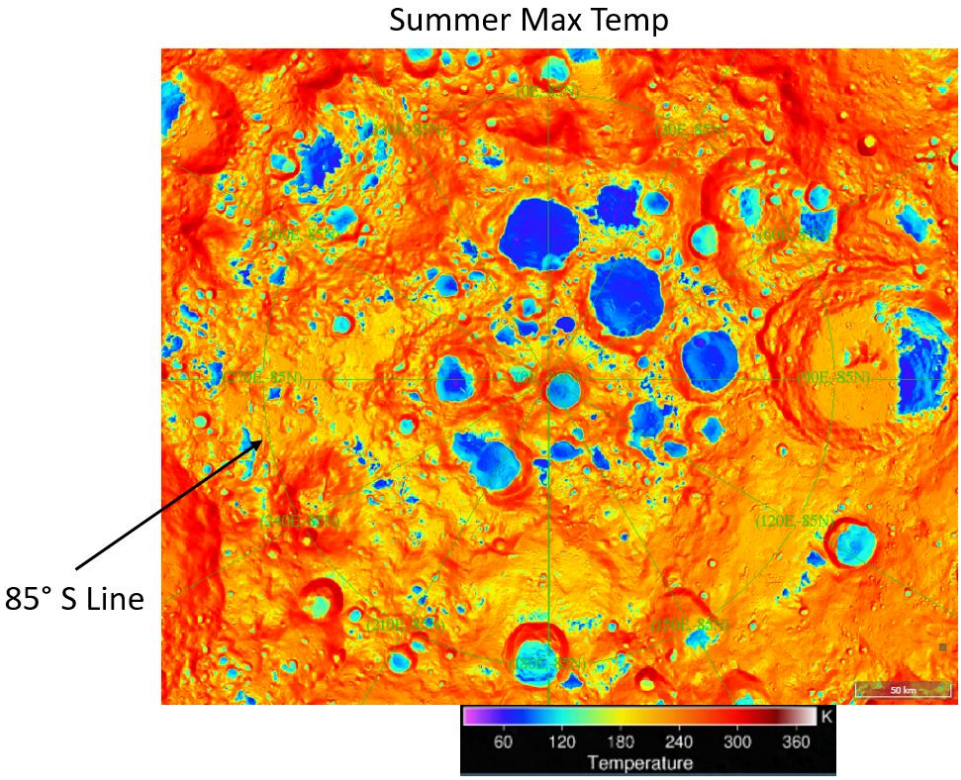

FIGURE 9.4.2-3: IMAGE FROM QUICKMAPS FOR SUMMER MAX TEMPERATURE AT LUNAR SOUTH POLE

References

[1] J. F. Gasbarre, R. M. Amundsen, S. Scola, F. B. Leahy, and J. R. Sharp, “Ground Plane and Near-Surface Thermal Analysis for NASA’s Constellation Programs,” p. 13, 2008.

[2] Howell, J.H. (2019) personal communication, 2019.09.30

Liskowsky, D.R., Seitz, W.W. (2014) Human Integration Design Handbook, NASA/SP-2010-3407/REV1, eds., Appendix B, p. 1167. (https://www.nasa.gov/sites/default/files/atoms/files/human_integration_design_handbook_revision_1.pdf)

[3] Feingold, A. and Gupta, K.G. (1970) "New analytical approach to the evaluation of configuration factors in radiation from spheres and infinitely long cylinders," *J. Heat Transfer*, vol. 92, no. 1, pp. 69-76, February. (http://www.thermalradiation.net/sectionc/C-125.html)

HI-SEAS, 2019, Hawai’I Space Exploration Analog and Simulator website (https://hi-seas.org/?p=1278)

[4] Lienhard IV, J.H., Lienhard V, J.H. (2019) *A Heat Transfer Textbook, 5th ed.,* Phlogiston Press, Cambridge, MA. p.558. (https://ahtt.mit.edu/)

[5] Martinez, I. (2019), Radiation View Factors, p.15 (http://webserver.dmt.upm.es/~isidoro/tc3/Radiation%20View%20factors.pdf)

[6] Sparrow, E.M.; Miller, G.B.; and Jonsson, V.K., 1962, "Radiative effectiveness of annular-finned space radiators, including mutual irradiation between radiator elements," *J. Aerospace Sci.,* vol. 29, no. 11, pp. 1291-1299. (http://www.thermalradiation.net/sectionc/C-77.html).

[7] Martinez, I. (2019) Radiative View Factors, p.13 (http://webserver.dmt.upm.es/~isidoro/tc3/Radiation%20View%20factors.pdf).

9.4.3 Far Field Terrain Modeling

The effects of far field lunar terrain with the potential to shadow or re-radiate onto a site of interest may be included in lunar surface thermal models via a projection technique. The far field terrain may be projected onto boundary elements around the perimeter of the local surface model. The potential for blockage (or shadowing) by far field lunar surface features may be first evaluated by the analytical technique described in section 9.4.3.

Rana, et al. [1] demonstrated this approach for the Luna 27 lander mission. The landing site was modeled as 30 meter radius disc with the lander positioned at the center. Concerns that several mountains in the region may shadow or radiate onto the lander led to the approach illustrated in Figure 9.4.3-1 with vertical elements on the perimeter to represent surface features 20-30 kilometers away. Analysis showed the effect of local mountains to be negligible in this case but the approach may be useful for scenarios where it is not possible to extend a local mesh to account for far field terrain.

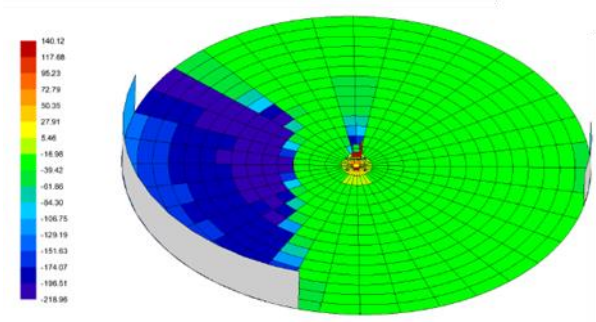

FIGURE 9.4.3-1: LUNA 27 FAR-FIELD BOUNDARY

Schunk, et al. [2] employed a similar technique to develop a projection of far-field terrain onto a two dimensional plane for shadowing considerations. Far-field geographical features within large data sets may be reduced to two angles (elevation and azimuth) relative to a specific site of interest on the lunar surface as shown in Figure 9.4.3-2.

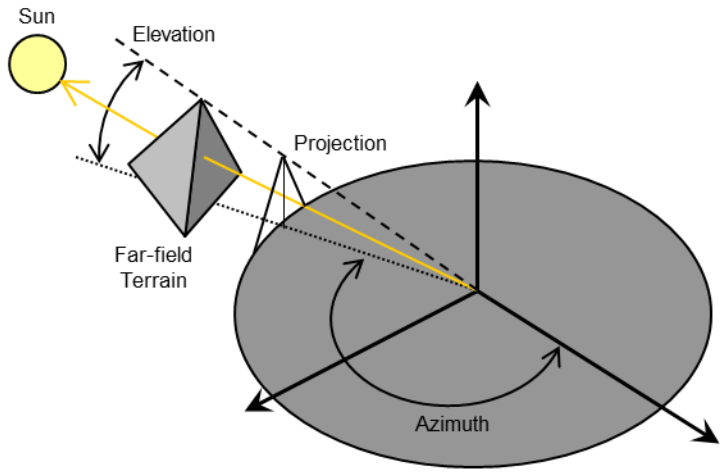

FIGURE 9.4.3-2: FAR FIELD BOUNDARY PROJECTION

Typical monthly Sun tracks superimposed on projected lunar terrain are shown in Figure 9.4.3-3. The terrain is referenced as an elevation angle relative to the local vertical with a 360° field of view (azimuth). The reference point is the Lunar South Pole at 0 meter elevation relative to the mean lunar radius. Terrain shadowing is evident at various times of the year. The Sun tracks were obtained from the Jet Propulsion Laboratory (JPL) Horizons Ephemeris with the lunar terrain from a United States Geographical Survey Lunar data set (circa 2007).

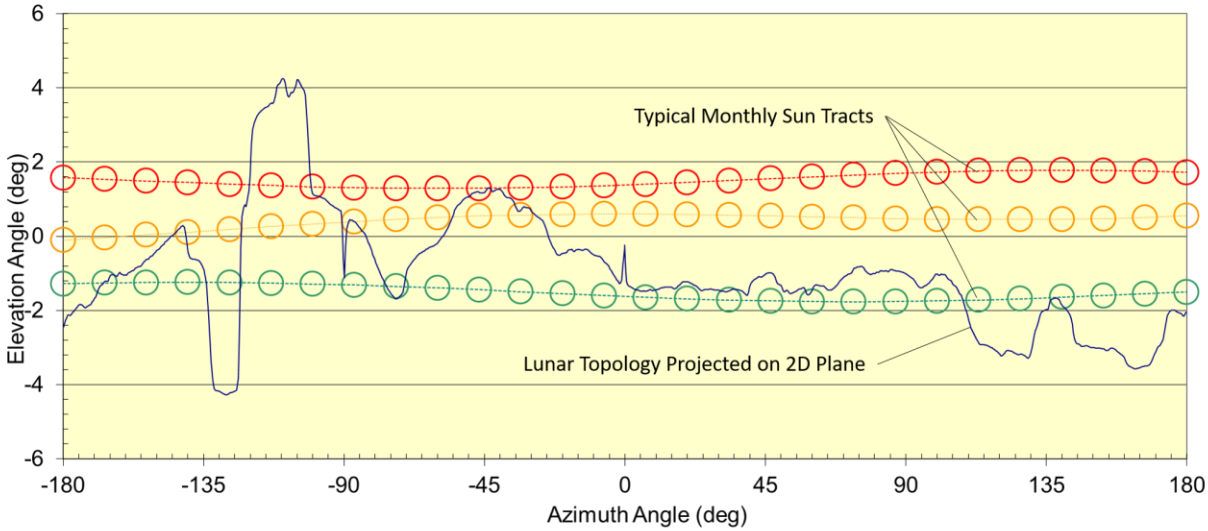

FIGURE 9.4.3-3: TWO DIMENSIONAL LUNAR TOPOLOGY PROJECTION WITH SUPER-IMPOSED SUN TRACKS

[1] H. Rana, V. Laneve, P. Hager, and T. Tirolien, “Thermal Modelling of Luna 27 Landing Site,” p. 10, 2017.

[2] G. Schunk, S. Sutherlin and O. Kornberg, “Constellation Thermal Overview-Altair”, Thermal and Fluid Analysis Workshop (TFAWS), MSFC, 2009.

9.5 DETAILED TERRAIN MODELING

9.5.1 Accessing, importing and utilizing LRO digital Lunar Surface Data

In order to create a thermal model with a detailed representation of the lunar surface, a mesh of the lunar surface must be constructed. Lunar surface meshes can be constructed using digital elevations models (DEMs) of the surface. A DEM specifies an average elevation for squares (e.g. 100m by 100m) on the lunar surface. DEMs have been created using elevations measured from Lunar Orbiter Laser Altimeter (LOLA) instrument on the Lunar Reconnaissance Orbiter [1,2]. An example DEM is pictured in Figure 9.5.1-2. At full resolution, each pixel gives an elevation corresponding to an x and y coordinates on a mapped simple cylindrical or polar stereographic projection of the surface. There are several methods for creating meshes of the surface from DEMs.

Mesh generation from LROC QuickMap website

The LROC QuickMap website (https://quickmap.lroc.asu.edu) is a public website that displays 3D, cylindrical and polar stereographic projections of the Moon. Heat maps for various LRO data sets can be viewed on the surface. Elevation vs. distances can be extracted for paths drawn on the lunar surface. Additionally, triangular 3D meshes of drawn sections of the lunar surface can be generated and downloaded as .stl files. These meshes are created using 100m by 100m DEMs.

To obtain a .stl files of the lunar surface on the QuickMap websites:

- Navigate to the Draw/Search menu
- Draw a rectangular polygon of the surface
- In the Search for Products dropdown select 3D Printing & Viewer and then select Export 3D model.
- Select the number of .stl files to generate that represent the surface.

The .stl files will be downloaded in a .zip file that contains a legend.png image that states the download region's location, dimensions, and minimum and maximum altitudes. The resulting mesh will likely need to be simplified before use in a thermal model, since it will include ~261 thousand vertices. Additionally, the mesh will include a base with engraved label. Mesh reduction methods are discussed in section 9.5.1.4.

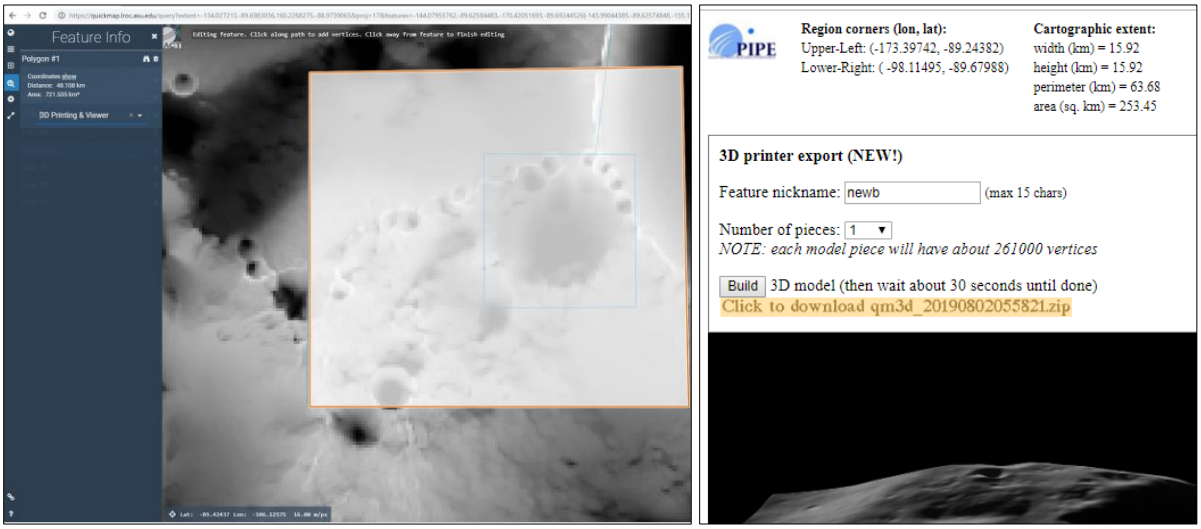

FIGURE 9.5.1-1: QUICKMAP WEBSITE WINDOWS SEEN WHEN SELECTING AND DOWNLOADING .STL FILES

Downloading DEMs from LRO websites

There are several LRO data products that provided lunar surface elevation information. Gridded data records (GDRs) contain elevations DEMs of polar or cylindrical projections.

LOLA GDRS can be downloaded from several LRO data websites.

- J. Wang, D. Scholes, and F. Zhou, "LOLA Gridded Data Record (GDR)," Planetary Data System (PDS) Geosciences Node Orbital Data Explorer Version 3.4.6 User's Manual, Oct-2019. [Online]. Available: https://ode.rsl.wustl.edu/moon/pagehelp/quickstartguide/index.html?diviner_GDR_L3.htm . [Accessed: 14-Jan-2020].
- "LOLA PDS Data Node," Sep-2019. [Online]. Available: http://imbrium.mit.edu/. [Accessed: 14-Jan-2020].
- "LRO: Frequently Asked Questions About LOLA Data," *PDS Geosciences Node, Washington University in St. Louis*, Aug-2019. [Online]. Available: https://pds-geosciences.wustl.edu/missions/lro/lola_faq.htm. [Accessed: 14-Jan-2020].

Note: jpegs of DEMS can be found on the second website by selecting to Browse "LOLA_GDR".

GDRs can be encoded as binary .image files or compressed image .jp2 files. Each file has an associated label file (with a .lbl extension) that describes the data product and how it's encoded. To give an example, look at ldem_85s_40m_float.lbl from (https://pds-geosciences.wustl.edu/lro/lro-l-lola-3-rdr-v1/lrolol_1xxx/DATA/LOLA_GDR/polar/). The objects SAMPLE_TYPE = PC_REAL and SAMPLE_BITS = 32 indicate the binary file samples should be extracted as 32-bit floating point numbers. In MATLAB® elevation data can be read into an array with ysize columns and xsize rows using the following command: M=fread(fid, [ySize,xSize],encoding);. In Python 2.7 the data can read with the struct.unpack_from() function and values can be parsed sequentially. Once an array of elevation data is formed it may need to be scaled according to a SCALING_FACTOR specified in the .lbl file.

Generating a point cloud that gives an (x, y, z), for each sample (xsample, ysample, elevation) in the DEM is a three step process. First, (xsample, ysample, elevation) is converted to the DEM coordinates: (x_on_map, y_on_map, radius from center of map, elevation). Second, the DEM coordinates is converted to spherical coordinates: (latitude, longitude, radius). Third, the spherical coordinates are converted to (x,y,z). This process accounts for the curvature of the Moon when generating the point cloud.

Instructions for the conversion process are provided in the catalog directory of the online GDR data (https://pds-geosciences.wustl.edu/lro/lro-l-dlre-4-rdr-v1/lrodlr_1001/catalog/) in 'dsmap_polar.cat' and 'dsmap.cat'. Additional information is also provided in the "LROC RDR Data Products Software Interface Specification (SIS)" (Bowman-Cisneros 2011)[5]. The exact steps of the conversion vary based on if the DEM was a simple cylindrical projection or a polar stereographic projection.

The following outlines an example process for creating a point cloud from a polar stereographic projection DEM of the Moon's South Pole. The DEM coordinates, as seen on Figure 9.5.1-2, can be determined by either of the flowing methods:

Definitions:

```
I = row index, which ranges from 1 to LINE_SAMPLES given in the .lbl file.
J = column index, which ranges from 2 to LINES given in the .lbl file
N = total number of lines = total samples per line (image is square).
MAP_SCALE = size of square in DEM in meters given in the .lbl file.
R_on_map = radius of circle from map's center to pixel at index I, J.
so = LINE_PROJECTION_OFFSET given in the .lbl file.
lo = SAMPLE_PROJECTION_OFFSET given in the .lbl file.
```

Method 1 [from dsmap_polar.cat]:

```
x_on_map=(I-N/2-0.5)*MAP_SCALE;
y_on_map =(J-N/2-0.5)*MAP_SCALE;
R_on_map=sqrt(x_on_map ^2+y_on_map^2);
```

Method 2 [3]:

```
x_on_map = (I-so-1)*MAP_SCALE;
y_on_map = (-1-lo+J)*MAP_SCALE;
R_on_map = sqrt(x_on_map ^2+y_on_map^2);
```

Latitude and Longitude in degrees can be determined by the following equations.

```
LON=90+atan2(y_on_map,x_on_map)*180/pi;
LAT=-90+180/pi*2*atan(0.5* R_on_map/1737400); % (southern hemisphere only)
% LAT = 90 - 180/PI * 2*ATAN(0.5 * R_on_map/1737400) (northern hemisphere)
```

[5] A couple of typos were found in the LROC RDR SIS for polar stereographic projections. The equation for y should be: y = (-1 - LINE_PROJECTION_OFFSET + LINE)* MAP_SCALE, in order to match the bounds of the DEM and dsmap_polar.cat. Also the equation for c should be: $c = 2\arctan(\rho/(2R))$. This corresponds to equation (21-15), with a ko=1 in J. Syder, Map Projections - A Working Manual. US Geological Surfey Professional Paper 1395, 1987.

Additionally, elevation in spherical coordinates, which includes the Moon's radius, is the following equation. The value is multiplied by 1000 to convert from km to meters.

```
ro=(M(I,J)*SCALING_FACTOR+OFFSET)*1000;
```

The x,y,z coordinates for the point cloud can be determined by standard math rules for converting from spherical coordinates to Cartesian coordinates. The units are meters.

```
x = ro * cos((LAT) * pi/180) * cos(LON * pi/180);
y = ro * cos((LAT) * pi/180) * sin(LON * pi/180);
z = ro * sin((LAT) * pi/180);
```

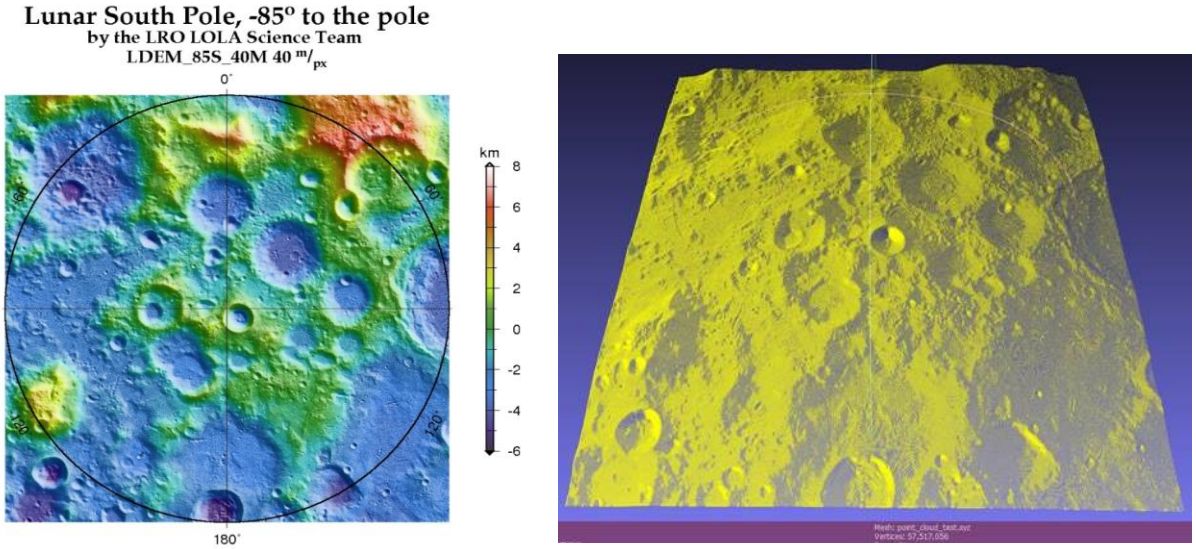

FIGURE 9.5.1-2: EXAMPLE DEM -85N TO THE SOUTH POLE (LEFT) AND POINT CLOUD GENERATED WITH THE ABOVE PROCESS (RIGHT). SOURCE: 'LDEM_85S_40M_FLOAT.IMG' (HTTP://IMBRIUM.MIT.EDU/BROWSE/LOLA_GDR/POLAR/SOUTH_POLE/)

Additional helpful information may be found at PDS Geosciences Node Community website: https://geoweb.rsl.wustl.edu/community/ .Linux and /Mac users might find the Integrated Software for Imagers and Spectrometers https://isis.astrogeology.usgs.gov/ useful for reading DEMS. Additionally, coordinate transformations could be performed using gdal https://gdal.org/programs/gdaltransform.html.

If only a section of the DEM is desired to be outputted to a point cloud as a .xyz files, excess points can be cut out. For example, say a box with each corner defined by a latitude and a longitude is desires, `box = [top_left, bottom_left, top_right, bottom_right]`. Without knowing the elevation, the box's corners in (x,y,z) can be approximated by the spherical to Cartesian coordinates above where `ro` equals the Moon's radius. Then when generating the .xyz file all points outside the box can be left out.

9.5.1.1 Mesh Generation

The PDS-released LOLA gridded DEMs are created by taking the median of elevation values at a particular pixel scale (using GMT's "blockmedian") and then interpolating a surface between these data using GMT's "surface". This builds a regular mesh between pixel (x,y,z) values. For software packages that allow irregular meshes, an alternative approach would be to create an uneven mesh between the pixels constrained only by where LOLA took observations (i.e. using the raw LOLA observation shots in the RDR data products). In practice, this is seldom done, because polar LOLA data has such high data density, and improving the LOLA raw observations by applying crossover corrections between different orbits is highly technical. Point clouds from high density DEMs can be converted to a mesh using a mesh triangulation technique such as Delauney triangulation or screened Poisson surface reconstruction.

Poisson surface reconstruction can be performed in MeshLab with the following steps:

- Compute normal vectors for mesh vertices that will be made from the xyz points by selecting: Filters > Point Set > Compute normals for point sets.
- Construct the mesh by selecting: Filters > Remeshing, Simplification, and Reconstruction > Screened Poisson Surface. Adjust the Reconstruction Depth to change the detail of the mesh. For example, when building a mesh from a 40m DEM, a value of 10 will result in elements roughly 100m wide, and a value of 12 will result in elements roughly 40m wide.
- Extra surfaces may be made if the point cloud was rectangular in shape. To remove them, select Filters > Selection > Select Faces with edges longer than ..... and choose a distance (e.g. 200 m), and then delete these surfaces.
- Clean up the edges by selecting Filters > Cleaning and Repairing > Remove isolated pieces (wrt Face Num.)

Note that because a DEM gives an average elevation per each square, illumination analysis (e.g. for power systems) is more accurate if the DEM is not interpolated into a mesh. In 3D this approach would create a "block world."

Alternative approaches can also be taken to create lunar surface meshes. For example Nash et al, first created a triangular mesh of the Moon as a sphere, then vertically adjusted the height of the vertices to match heights found by interpolating as DEM. The DEM was interpolated using Delaunay Triangulation [4].

9.5.1.2 Grid Size Guidance

Grid size impacts model workability, run times, and disk space. Following the method in section 9.5.1.3, importing and editing a lunar mesh with ~40k faces into Thermal Desktop is extremely slow. Meshes with ~5k to ~20k faces are much easier to work with on a workstation class computer. In AutoCAD®, workability can be improved by: 1) viewing the mesh with "Wireframe" or "Hidden" instead of the shaded views, and 2) turning off the option to highlight selected surfaces (in the AutoCAD® command prompt type "Highlight" then 0).

To give an rough idea of model run times and disk usage, below are statistics for 2 detailed lunar surface models ran on a workstation computer with 64GB of ram and two Intel Xeon Silver 4214 @ 2.20GHz.

Mode 1:

- Terrain Size: 100 km × 28 km
- Model Size: 10,093 surface nodes / 80,744 subsurface nodes / 19,962 faces
- Time for 2 year transient run: 3.5 hours
- Heat Rate Calculations: 500 rays shot per node / 2190 orbital positions
    - Compute time with a max oct-tree subdivision of 7 (default): 4 hours
    - Compute time with a max oct-tree subdivision of 15: 2.1 hours
    - Disk space used: 466 GB (Surface IR calculations used 397MB)

Model 2:

- Terrain Size: 76 km × 46 km
- Model Size: 4,647 surface nodes / 37,716 subsurface nodes / 11,965 faces
- Time for 2 year transient run: 1.2 hours
- Heat Rate Calculations: 500 rays shot per node / 2190 orbital positions
    - Compute time with a max oct-tree subdivision of 7 (default): 2 hours
    - Disk space used: 99 GB

Computation times will vary based on the computer specs, resource usage from other tasks, and model configurations. For example, run times can improve if the frequency of writes to the .sav file is decreased. (This is controlled by setting the Thermal Output Increment in the Case Set Manager's Output Tab). Additionally, ray tracing times increase as the number of rays shot per node is increase. Ray tracing times also improve, to a point[6], as the max number of oct-tree subdivisions is increased. (This parameter is set in the Advanced Control tab of the Radiation Analysis Data dialog box for a given radiation task).

Overall, a good technique is to create a grid/mesh that is tight close to the vehicle and less and less tight further away from the vehicle. The graded approach enables larger regions of the surface to be modeled. For example, this allows a mountain 50 km away from a vehicle to be included in the model. Moreover, a tight grid near the vehicle is important for predicting hot/cold spots on vehicle sub-components from reflected/shaded sunlight.

The shape of the vehicle's shadow on the lunar surface, indicated by the temperature gradient of the surface, is a good indication of if the grid is tight enough. Gasbarre et al.'s method [1] is useful for estimating a maximum size and grid density of the region nearest a vehicle. This method is

[6] See the "Optimize Cells" section of the Thermal Desktop Manual.

based on comparing the change in average temperature of a cylinder, which represents a vehicle, due to grid density.

For simple terrain models, past work has used the following grid sizes. To analyze cryogenic propellant and life support tanks, Christie et al. used a dense center region (10 m x 10 m with 1.25 m x 1.15 m elements) surrounded by a less dense region (100 m x 100 m with 5 m x 5 m elements) [2]. To analyze a small lander, represented by a $1m^3$ cube, Tae-Yong et al. used a dense cross-shaped region (10 m wide with 0.3 m x 0.3 m elements) in a 100 m x 100 m rectangle with less dense corners (with 10 m x 10 m elements) [3]. To analyze a spacesuit radiator, Ochoa et al. used a dense center region (46 m x 46 m with 1 m x 1 m elements) placed in the center of 8 blocks, each (166 m-46 m)/3 wide and long [4]. The center region accounts for 92.7% of the total energy from a differential element at a height of 1.47 m to a rectangular infinite plane (i.e. $F_{dA1-center}$=0.927 x (.245)).

[1] J. F. Gasbarre, R. M. Amundsen, S. Scola, F. B. Leahy, and J. R. Sharp, “Ground Plane and Near-Surface Thermal Analysis for NASA’s Constellation Programs,” p. 13, 2008.

[2] D. A. Ochoa, B. M. Miranda, B. C. Conger, and L. A. Trevino, “Lunar EVA Thermal Environment Challenges,” *SAE Transactions*, vol. 115, pp. 492–505, 2006.

[3] R. Christie, D. Plachta, and M. Hasan, “Transient Thermal Model and Analysis of the Lunar Surface and Regolith for Cryogenic Fluid Storage,” Aug. 2008.

[4] T.-Y. Park, J.-J. Lee, J.-H. Kim, and H.-U. Oh, “Preliminary Thermal Design and Analysis of Lunar Lander for Night Survival,” 2018.

9.5.1.3 Importing Meshes

Building Detailed Lunar Surface Models in Thermal Desktop

There are many approaches to importing meshes into Thermal Desktop. Since lunar surface meshes are quite large the method presented here was aimed at making the importing process quick. Other methods are possible leveraging OpenTD features new to version 6.1.

Since, Thermal Desktop is built off of AutoCAD® the AutoCAD® `Add3Face` command can be used to create an AutoCAD® mesh element given x, y, and z components of vectors that describe either a triangular or quadratic mesh elements. These elements then can be converted into Thermal Desktop surfaces.

One method for generating x, y, and z vector components is to use numpy.stl library [5]. Sample Python 2.7 code for doing this is provided in the appendix in the function titles `generate_xyz_for_autocad_import(inputfile)`. The overall technique is to use the library call `mesh.Mesh.from_file(inputfile)` to import a mesh from an existing .stl file. Then the mesh vectors can be accessed and written to an output file. For a mesh titled `s_mesh`, the object `s_mesh.vectors` contains a list of all mesh vectors. An individual vector can be accessed with the object `s_mesh.vectors[i][j][k]`.

In AutoCAD®, sequential calls to the `Add3Face` command can be automated in a Visual Basic for Applications (VBA) module [6]. Sample code for such a module is included in Appendix A. To be used the Microsoft VBA module must first be download from the Autodesk® website. Once installed, the Visual Basic editor can be accessed by typing the following into the AutoCAD® command line: `VBAMAN`, then selecting the "Visual Basic Editor" button in the "VBA Manager" window. The desired VBA module can then be saved in the AutoCAD® file by selecting to embed it into the .dwg.

To convert the resulting mesh to TD surfaces go to Thermal>FD/FEM Network> and select Convert AutoCAD® Surface to Node/Elements. Next select the surface and merge nodes. To speed up this second step, first type Highlight into the AutoCAD® command line and enter 0 as the new value for HIGHLIGHT. This will turn off the highlighting of selected objects. The default setting for HIGHLIGHT is 1.

Now that a surface mesh exists in Thermal Desktop its thermophysical and optical properties can defined. Subsurface layers can be easily created by first defining a Material Stack of lunar regolith and adding the stack beneath the surface mesh as insulation (see section 9.2.1). Then a heat load can be added beneath the surface, and the radiative environment can be defined (see section 9.1). Lastly, the surface may need to be moved, since the orbit is defined with respect to the world coordinate system. In that case, attach an assembly (i.e. articulator to the surface and all objects on it) to move everything together.

If desired, sections of the mesh in Thermal Desktop can be refined using the Refine Element's command located in the Thermal dropdown menu under Modeling Tools > Refine Elements.

9.5.1.4 Mesh Reduction Techniques

Often, meshes produced directly from LOLA DEMs or using the QuickMap website will need to be simplified. Various approaches could be taken to reduce the mesh, depending on the user's preferred software. This section will give an example approach that 1) manipulates .stl file using the Python numpy-stl library [7], and 2) simplifies the mesh using a free software called MeshLab [8].

The general technique here is to simplify lunar surface elements located further from the object's location. Removing as much ground as possible helps speed up runtime when lunar surface temperatures are calculated in Thermal Desktop.

Manipulating .stl file using the Python numpy-stl library.

One way to reduce a surface mesh is to remove everything below a threshold elevation. Therefore, low lying areas, such as the bottom of Shackleton crater, that do not see the vehicle or terrain around it, can be removed.

Sample Python 2.7 code for removing mesh elements below a certain threshold with the numpy-stl library [7] this is provided in the appendix in the function:

```
cut_extra_vectors(surface_mesh,z_threshold,newstlfilename).
```

The overall technique consists of the following steps

- Import a mesh, `s_mesh`, from the surface .stl file by calling `mesh.Mesh.from_file(inputfile)`
- Loop through the s_mesh's list of mesh vectors `s_mesh.vectors`, and for each vector check if its z component, `s_mesh.vectors[i][j][2]`, is below a specified threshold elevation.
- Copy the vectors above the threshold into a new list `data` (initialized with `data = np.zeros(num_vectors, dtype=mesh.Mesh.dtype)`) using the numpy `copyto()` function.
- Build a new mesh, `new_surf`, containing mesh vectors by calling `mesh.Mesh(data)`
- Regenerate mesh with remaining mesh vectors by calling `new_surf= mesh.Mesh(data)`

Additionally, if multiple .stl files were generated with the QuickMap website, they can be combined. An example for combining .stl files is given on the library's documentation website (https://numpy-stl.readthedocs.io/en/latest/usage.html#modifying-mesh-objects).

Reducing mesh using MeshLab using the GUI

In MeshLab there is no undo button, so meshing and saving in increments saves time. Documentation for the techniques used by the software is available on its website. There are also multiple tutorials for using the software on the internet.

Below are some basic steps for mesh reduction that we have found to be helpful.
Note that we used a copy of MeshLab download in 2019.

- (To Open) Select File> Import Mesh
- (Cleanup Mesh) Select Filters tab > Cleaning and Repairing > Remove Duplicate Faces
  - There should be none for a QuickMap generated .stl
- (Cleanup Mesh) Select Filters tab > Cleaning and Repairing > Remove Duplicate Vertices
  - There should be none for a QuickMap generated .stl
- (A Simplification Method) Select Filters tab > Remeshing, Simplification, and Reconstruction > Simplification Clustering Decimation
  - This option can be useful as a first step for mesh reduction. It retains the clean shape of the QuickMap generated mesh elements.
  - The "Affect only selected faces" option did not function in the version we downloaded.
  - The size of the re-meshed cells can be adjusted with the up and down arrows under *world unit*. Larger values produce larger cells.
- (A Simplification Method) Select Filters tab > Remising, Simplification, and Reconstruction > Quadratic Edge Collapse Decimation
  - The default quality threshold is 0.3 closer to 0 is better quality closer to 1 is worse.
  - Using this method a section of the mesh could be highlighted and the "Affect only selected faces" box selected, in order to selectively simplify sections of the mesh.
  - There are additional options available as well, including preserving topology or preserving the boundary of the mesh.
- (Save) To save select File> Export Mesh As.
  - Can choose to unselect "Materialize Color Encoding"
- (Fixing Errors)

- Sometimes simplifying the mesh results overlapping faces. In that case try the following:
- Select the violating area of interest then Filters tab > Cleaning and Repairing > Remove Faces from Non Manifold Edges
- Select violating face and then Filters tab > Remising, Simplification, and Reconstruction > Remove holes

References

[1]M. K. Barker, E. Mazarico, G. A. Neumann, M. T. Zuber, J. Haruyama, and D. E. Smith, "A new lunar digital elevation model from the Lunar Orbiter Laser Altimeter and SELENE Terrain Camera," *Icarus*, 2015.

[2] D. E. Smith *et al.*, "The Lunar Orbiter Laser Altimeter Investigation on the Lunar Reconnaissance Orbiter Mission," 2008.

[3] E. Bowman-Cisneros and E. Eliason, "LROC RDR Data Products Software Interface Specification." Arizona State University, 08-Mar-2011. http://lroc.sese.asu.edu/data/LRO-L-LROC-5-RDR-V1.0/LROLRC_2001/DOCUMENT/RDRSIS.PDF

[4] E. Sefton-Nash *et al.*, "Evidence for ultra-cold traps and surface water ice in the lunar south polar crater Amundsen," *Icarus*, vol. 332, pp. 1–13, Nov. 2019.

[5] Rick van Hattem, "numpy-stl 2.10.1" [Online]. March 2019, Available: https://pypi.org/project/numpy-stl/.

[6] "Download the Microsoft VBA Module for AutoCAD® | AutoCAD® 2017 | Autodesk® Knowledge Network." [Online]. Available: https://knowledge.autodesk.com/support/autocad/troubleshooting/caas/downloads/content/download-the-microsoft-vba-module-for-autocad.html. [Accessed: 17-Jan-2020].

[7] Rick van Hattem, "numpy-stl 2.10.1" [Online]. March 2019, Available: https://pypi.org/project/numpy-stl/.

[8] P. Cignoni, M. Callieri, M. Corsini, M. Dellepiane, F. Ganovelli, G. Ranzuglia, "MeshLab: an Open-Source Mesh Processing Tool," *Sixth Eurographics Italian Chapter Conference*, page 129-136, 2008. Available: http://www.meshlab.net/.

9.6 MODELING EXAMPLE

Reserved.

9.6.1 Comparison to LRO Diviner Temperature Data

Reserved.

10.0 ACCOUNTING FOR LUNAR DUST IMPACTS

Lunar dust can have a significant impact on thermal analysis due to its contamination effects, among them the effect on thermo-optical properties on radiator surfaces. Dust transport mechanisms may be due to vehicle-based forces or electrostatic forces. Examples of the former include rover wheel motion, vehicle engine plumes and other expellants. Such disturbances may be analyzed with ballistic-based methods or, in the case of plumes, with computational fluid dynamic and particle entrainment codes that may involve both the continuum and molecular regimes. Specific attention should be paid to multi-engine landers that can induce unexpected re-circulation zones.

If such analysis shows that radiator surfaces are subject to dust deposition originating from vehicle-based forces, regolith optical properties may be assumed for those surfaces. The same is assumed for those radiator surfaces that may be subject to falling debris due to a rover driving, such as when driving into pits or near terrain features that will overhang these surfaces. If the dust coverage is thick enough (i.e. more than a mono-layer) then heat must first be conducted through the dust before it is radiated to space. Often, this results in effective environmental sink temperatures that are too extreme and the need for mitigation measures in order for the thermal design to close.

Assuming mitigation measures have been implemented (e.g., articulated covers that protect radiator surfaces; dust removal tools; electrodynamic dust shields), or if a stationary lander is shown to not cause significant dust deposition, then the surface may be assumed to be subject to dust accumulation via electrostatic forces, and the radiator is assumed to have a monolayer of dust coverage. The optical depth of a monolayer results in a change in radiator surface thermo-optical properties that trend somewhere in between the coating's pristine value and that of the regolith. This change also depends on the type of radiator coating used. How much of the radiator surface is assumed to be covered with a mono-layer of dust may be determined by discussion with a project and its risk tolerance. It is highly recommended that projects assume 100% monolayer coverage, unless a lesser percentage seems justified based on the specific architecture and application.

Dr. James Gaier, and his team, have done many studies on the effects of lunar dust on typical radiator surfaces, and a thermal engineer who must deal with dust should read his papers to become familiar with his work. One thing to keep in mind is that simulant is different from lunar regolith.[2]

Gaier, et al.[3] 2010 paper shows the results of the effect of simulant on two typical radiator coatings: AZ-93 White Paint, and a second surface silver coated Teflon - Ag/FEP. Some conclusions from that paper are:

- Even a "sub-monolayer" of simulated lunar dust can significantly degrade the performance of both coatings. As little as 12% dust coverage can degrade the solar absorptivity (α) by as much as 50%. A copy of this is shown in Figure 10.0-1 and Figure 10.0-2 below.

- Dust has an effect on hemispherical emissivity (ε) also. AZ-93 may be degraded by as much as 16% with 54% dust coverage; Ag/FEP may be improved by as much as 11% for 35% coverage. A copy of this is shown in Figure 10.0-3 and Figure 10.0-4 below.

- A sub-monolayer of dust does not significantly change the steady-state temperatures at which a shadowed surface radiates. (As mentioned earlier, this would not be true if there is more than a mono-layer because the heat must conduct through the low conductivity regolith layer before it can be radiated to space.) Although ε is altered by the dust, the radiative power is not diminished. The major effect is the change in α. Therefore a dusted radiator that is in the Sun will have a much higher sink temperature. A plot of the change in α/ ε is shown in Figure 10.0-5.

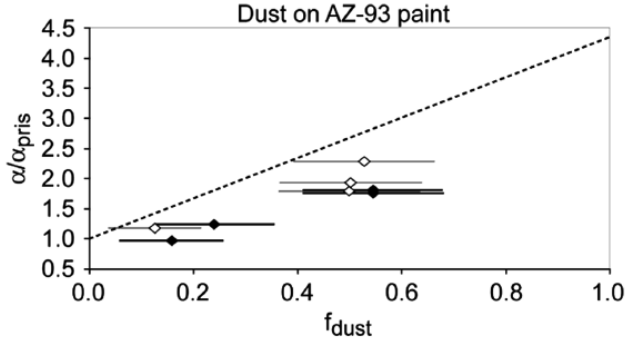

Fig. 6 Plot of α/α_{pris} as a function of f_{dust} for the AZ-93 painted aluminum (◇), composite (◆), and the rule of mixtures (——).

FIGURE 10.0-1: EFFECT OF SIMULANT DUST ON AZ-93 SOLAR ABSORPTIVITY FROM GAIER, ET AL.,[3]

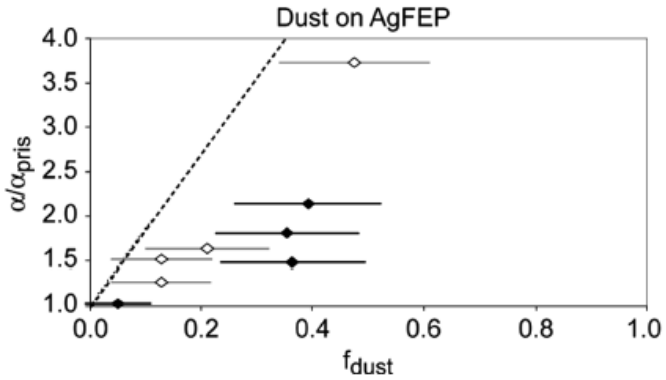

Fig. 9 Plot of α/α_{pris} as a function of f_{dust} coverage for the AgFEP applied to aluminum (◇), composite (◆), and the rule of mixtures (——).

FIGURE 10.0-2: EFFECT OF SIMULANT DUST ON AG-FEP SOLAR ABSORPTIVITY FROM GAIER, ET AL.,[3]

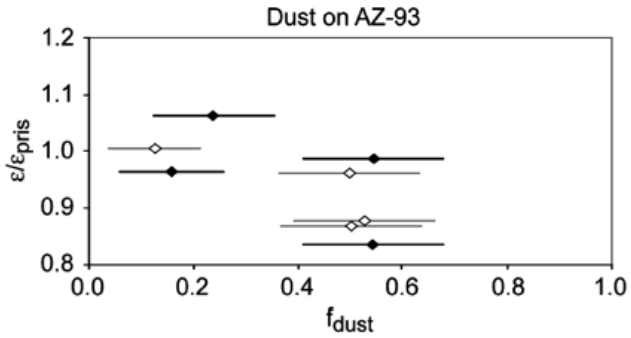

Fig. 8 Plot of $\varepsilon/\varepsilon_{pris}$ as a function of f_{dust} for the AZ-93 painted on aluminum (◇) and composite (◆) substrates.

FIGURE 10.0-3: EFFECT OF SIMULANT DUST ON AZ-93 EMISSIVITY FROM GAIER, ET AL.,[3]

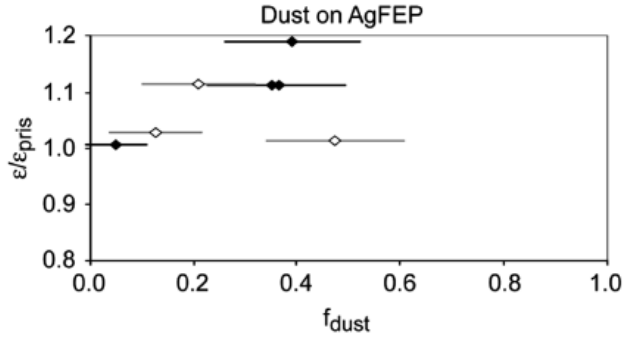

Fig. 10 Plot of $\varepsilon/\varepsilon_{pris}$ as a function of f_{dust} for the AgFEP on aluminum (◇) and composite (◆) substrates.

FIGURE 10.0-4: EFFECT OF SIMULANT DUST ON AG-FEP EMISSIVITY FROM GAIER, ET AL.,[3]

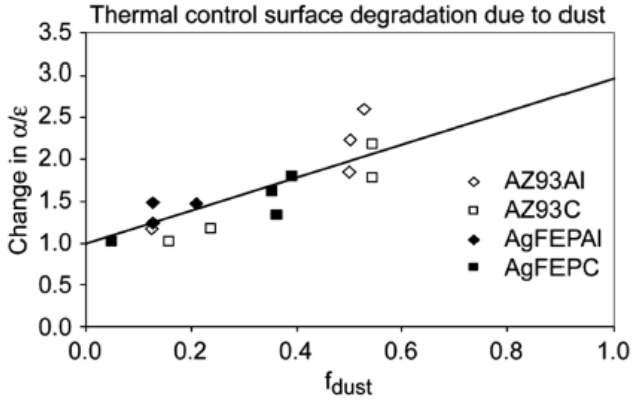

Fig. 11 The total change in α/ε as a function of f_{dust}.

FIGURE 10.0-5: EFFECT OF SIMULANT DUST ON AG-FEP AND AZ-93 A/ E FROM GAIER, ET AL.,[3]

Gaier, et al.[4] 2013 paper gives plots of the effect on optical properties of typical radiator materials with testing different regolith simulants that have varying optical properties that are more encompassing of the lunar variation. A plot is shown in Figure 10.0-6 below.

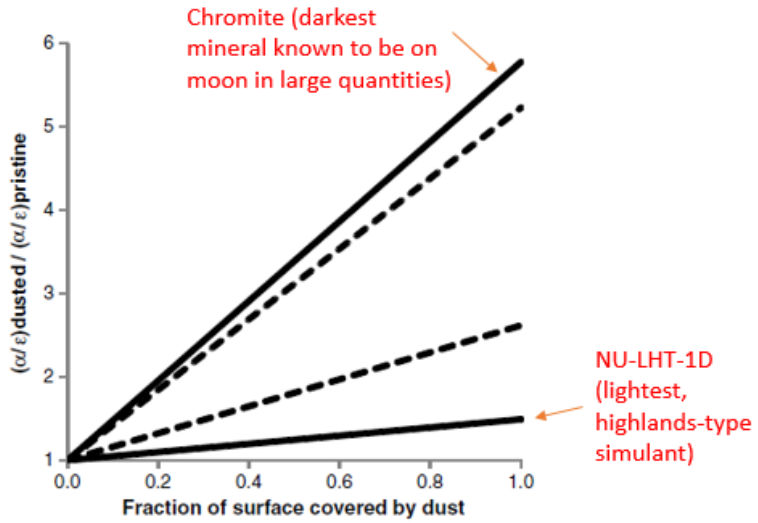

Fig. 4 The change in the α/ε as dust accumulates on AgFEP (solid lines) or AZ93 (dashed lines).

FIGURE 10.0-6: EFFECT OF VARYING SIMULANT DUST ON AG-FEP AND AZ-93 A/ E FROM GAIER, ET AL.,[4] WITH ANNOTATIONS IN RED.

As described earlier, for a sub-monolayer of dust one may conservatively assume that the change in α/ ε for typical low- α, high-ε radiator materials is completely done by the solar absorptivity. However this would not be true for surfaces with low-ε properties, such as specular shield. The size of lunar dust particles are large enough that it cannot be considered IR transparent. Therefore, the effects of lunar dust on both emissivity and specularity will require characterization testing for the given surface and regolith type.

[1] P. Hager, U. Walter, and D. M. Klaus, “Impact of lunar dust on radiator design for Moon bases and rovers,” in *43rd International Conference on Environmental Systems*, American Institute of Aeronautics and Astronautics.

[2] J. Gaier, S. Ellis, and N. Hanks, “Thermal Optical Properties of Lunar Dust Simulants and Their Constituents,” in *3rd AIAA Atmospheric Space Environments Conference*, Honolulu, Hawaii, 2011.

[3] J. R. Gaier, J. Siamidis, and E. M. G. Larkin, “Effect of Simulated Lunar Dust on the Properties of Thermal Control Surfaces,” *Journal of Spacecraft and Rockets*, vol. 47, no. 1, pp. 147–152, 2010.

[4] James R. Gaier, “Studies of Simulated Lunar Dust on the Properties of Thermal-Control Surfaces,” *Journal of Spacecraft and Rockets* 50, no. 4 (July-August 2013): 848.

Additional Reading Not Referenced Above:

[-] R. Durkee and J. Harris R., “Lunar dust deposition effects on the solar absorptance of thermal control materials,” in *6th Thermophysics Conference*, 0 vols., American Institute of Aeronautics and Astronautics, 1971.

[-] Ashwin R Vasavada, Joshua :. Bandfield, Benjamin T. Greenhagen, Paul O. Hayne, Matthew A. Seigler, Jean-Pierre Williams, and David A. Paige, “Lunar equatorial surface temperatures and regolith properties from Diviner Lunar Radiometer Experiment.” Journal of Geophysical Research, Vol. 117,2012.

11.0 SPECIAL CONSIDERATIONS FOR PSRS

11.1 EARTH SHINE

Perpetually Shaded Regions (PSRs) of the lunar polar craters may experience non-negligible thermal radiation and reflected solar radiance from the Earth. Peak broadband earthshine may exceed 150 mW/m^2 for localized regions [1]. The hemispherical earthshine at the lunar surface may be approximated by:

$$Q = \left(\frac{R_{Earth}}{R_{Earth-Moon}}\right)^2 (S_o A\gamma + \sigma T^4)$$

where S_o is the solar flux, A is the Earth’s albedo, γ is the fraction of the illuminated Earth disk (100% for peak) and T is the black body temperature of the Earth. Using the expression above, the infrared contribution is estimated to be 56 mW/m^2 while the reflected solar is 100 mW/m^2 with typical values for solar flux, albedo, black body temperature and peak illumination. Using the JPL ephemeris (see Section 9.1.2) it is possible to obtain the Earth elevation angle (unobstructed by local terrain) and the fraction of the Earth’s disk illuminated by the Sun as shown in Figure 11.1-1 and Figure 11.1-2 for a location at 85ºN latitude on the lunar surface. By considering the elevation angle over an entire calendar year, the longitude of the specific location can be neglected. Much like the Sun, the Earth will set below the horizon as indicated by a negative elevation angle. The ephemeris calculation of the illuminated fraction of the Earth’s disk does not account for blockage by the observer body (i.e. the Moon). If the Earth is set below the horizon it is not visible on the Moon regardless of the illuminated fraction.

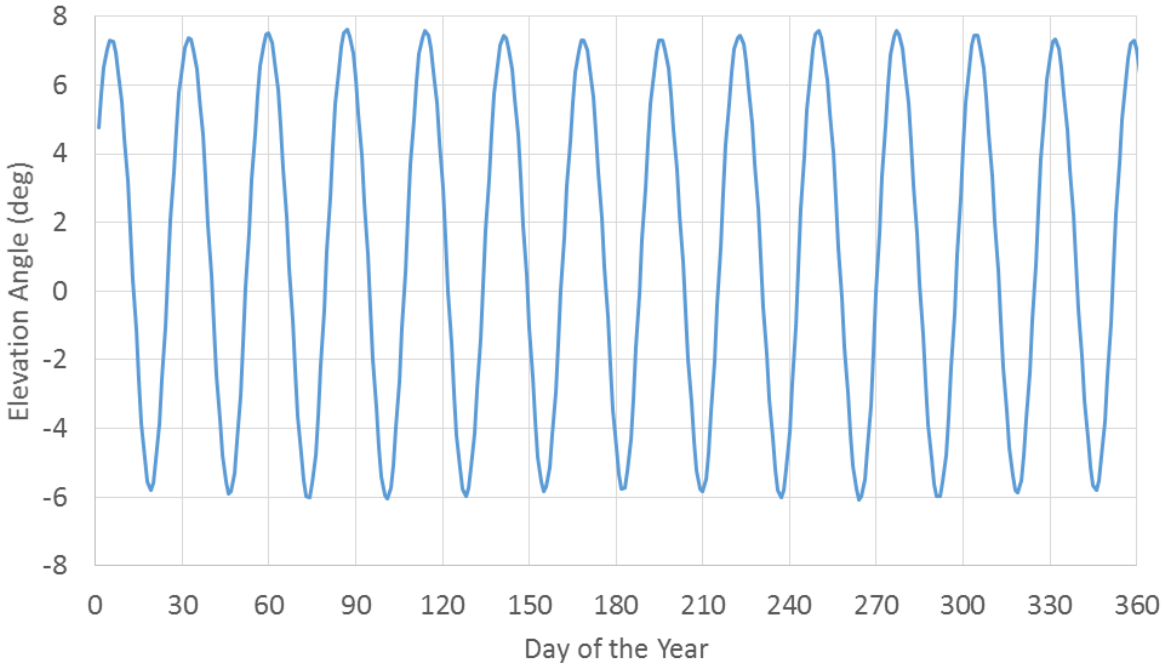

FIGURE 11.1-1: YEARLY VARIATION IN SOLAR ELEVATION ANGLE FOR LOCATION ON THE LUNAR SURFACE (85°N LATITUDE)

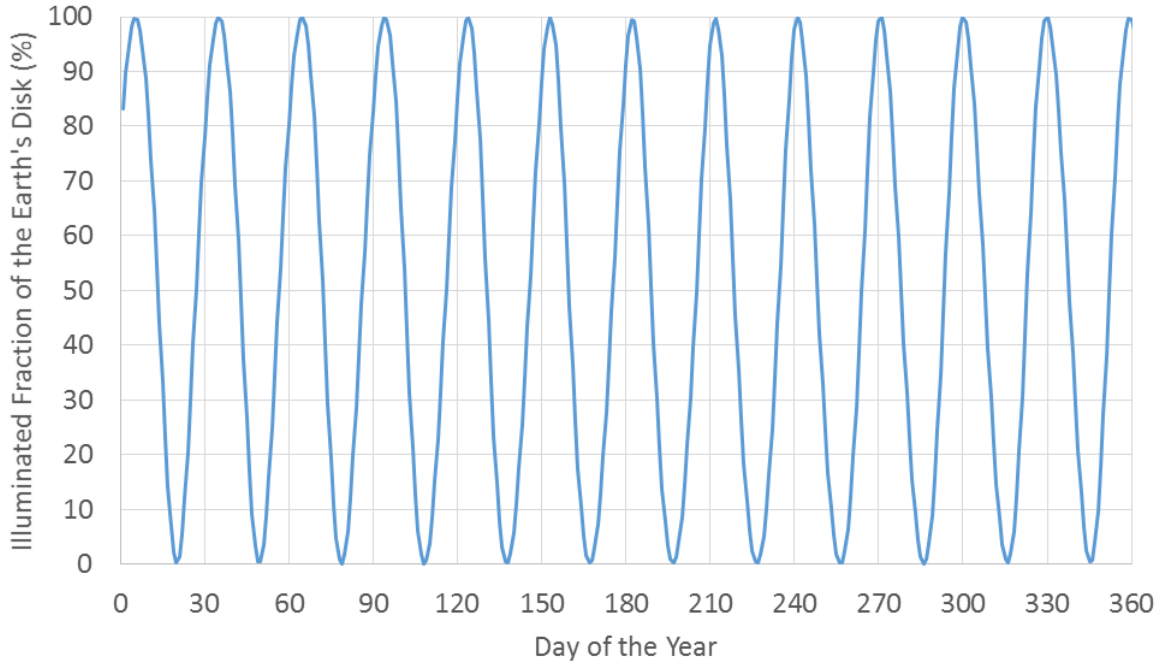

FIGURE 11.1-2: ILLUMINATED FRACTION OF THE EARTH'S DISK FOR OBSERVER ON LUNAR SURFACE (85°N LATITUDE)

The elevation angle is relative to a plane perpendicular to the Moon's spherical envelope. To compute an incident flux upon a surface from earthshine the inclination of the local surface must

be summed with the elevation angle as shown in the equation below. The geometric relationship is illustrated in Figure 11.1-3. Surfaces tilted toward the equator will be the most affected as solar azimuth angles typically range between 170° and 190° for polar locations.

$$Q = \left(\frac{R_{Earth}}{R_{Earth-Moon}}\right)^2 (S_o A\gamma + \sigma T^4)\sin(\theta_A + \theta_S)$$

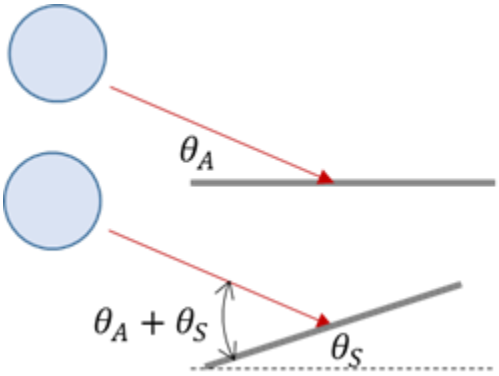

FIGURE 11.1-3: SURFACE INCLINATION AND SOLAR ELEVATION ANGLE

A typical yearly variation of Earthshine is shown for a lunar location at 85°N latitude with a surface tilt of 15° in Figure 11.1-4. The flux is zero for when the Earth sets below the horizon as shown in the figure. The variation and peaks of the reflected solar are greater than the infrared contribution.

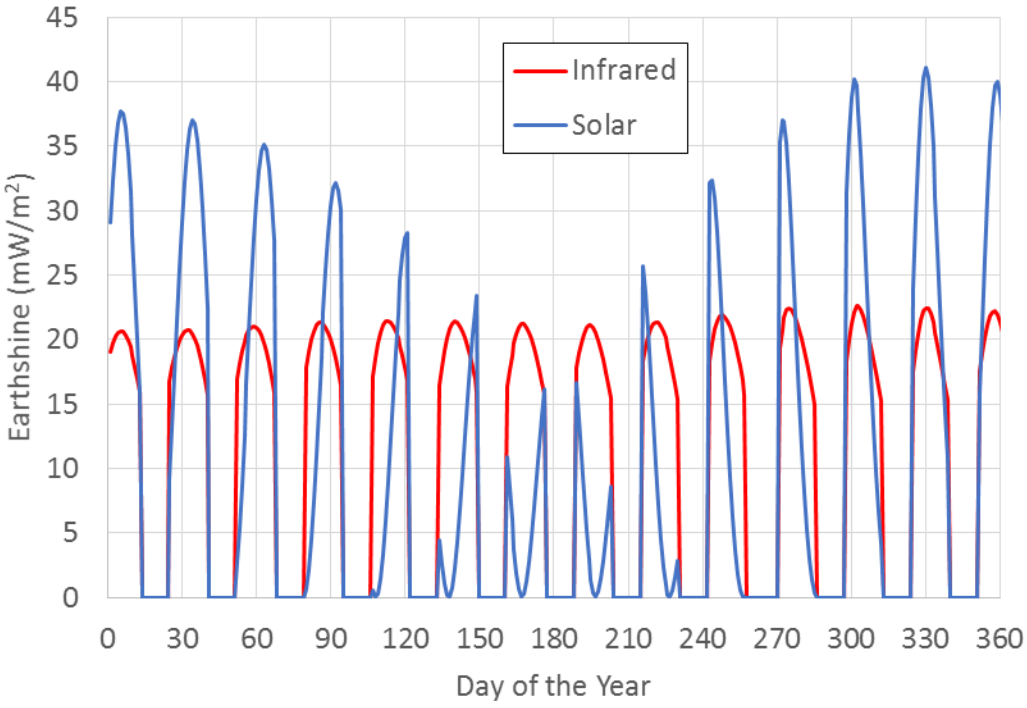

FIGURE 11.1-4: TYPICAL EARTHSHINE FOR LUNAR LOCATION (85°N, TILT=15°)

[1] David A. Glenar, et. al., “Earthshine as an Illumination Source at the Moon”, Icarus, Volume 321, p. 841-856, March 2019.

11.2 LUNAR SURFACE TEMPERATURE FOR COLD CASE ANALYSIS

Detailed thermal analysis combining thermo-physical properties of the Lunar surface and subsurface with the ground heat flow (see Section 5.4) result in surface temperature predictions approaching -428 F (18 K) for regions considered to be “permanently shaded” [1]. The floor of craters near the Lunar poles can experience reflected solar flux from the crater walls which increase the surface temperature to approximately -370 F (50 K) without direct solar flux impingement.

Most surface assets are non-cryogenic and the primary mode of heat transfer with the surface is radiative. Therefore, for such cases, it is a conservative thermal modeling approach to treat the surface temperature as a boundary condition within this temperature range -428 to -370 F (18 to 50 K). The Lunar surface temperatures will typically increase near the surface asset analyzed. Maintaining the surface temperature at the lower boundary conditions avoids the analytical overhead needed to accurately calculate surface temperatures on a detailed grid.

[1] D. A. Paige and M. A. Siegler, “New Constraints on Lunar Heat Flow Rates from LRO Diviner Lunar Radiometer Experiment Polar Observations,” vol. 47, p. 2753, Mar. 2016.

12.0 REFERENCES

The following documents contain supplemental information to guide the user in the application of this document. References are also included in the relevant document sections.

For lunar landing site specific geomorphology and lighting conditions data from numerous lunar orbiting spacecraft measurements and analysis can be found on the Planetary Data System (http://imbrium.mit.edu/DATA/SLDEM2015_SLOPE/) or can be visualized with QuickMap or JMars.

A Dollfus and E. Bowell, “Polarimetric Properties of the Lunar Surface and its Interpretation”, Astronomy and Astrophysics 10, 29-53, 1971.

A. E. Wechsler and P. E. Glaser, “Pressure effects on postulated lunar materials,” Icarus, vol. 4, no. 4, pp. 335–352, Sep. 1965.

A. R. Vasavada et al., “Lunar equatorial surface temperatures and regolith properties from the Diviner Lunar Radiometer Experiment:,” J. Geophys. Res., vol. 117, no. E12, p. n/a-n/a, Dec. 2012, doi: 10.1029/2011JE003987.

A. Vasavada, D. Paige, and S. Wood, “Near-Surface Temperatures on Mercury and the Moon and the Stability of Polar Ice Deposits,” Icarus, vol. 141, no. 2, pp. 179–193, Oct. 1999.

B. O’Connor and E. Abel, “Radiator Study for Stationary Lunar Landers,” NESC Thermal Fluids and Analysis Workshop, 2018.

Bertrand Baudouy, “Heat Transfer and Cooling Techniques at Low Temperature”, CEA Saclay, France, January 2015.

C. J. Cremers and H. S. Hsia, “Thermal conductivity and diffusivity of Apollo 15 fines at low density,” Lunar and Planetary Science Conference Proceedings, vol. 4, p. 2459, 1973.

C. J. Cremers and H. S. Hsia, “Thermal conductivity of Apollo 16 lunar fines,” Lunar and Planetary Science Conference Proceedings, vol. 3, p. 2703, 1974.

C. J. Cremers and R. C. Birkebak, “Thermal conductivity of fines from Apollo 12,” Lunar and Planetary Science Conference Proceedings, vol. 2, p. 2311, 1971.

C. J. Cremers, “Heat Transfer Within the Lunar Surface Layer,” in Advances in Heat Transfer, vol. 10, J. P. Hartnett and T. F. Irvine, Eds. Elsevier, 1974, pp. 39–83.

C. J. Cremers, “Thermal conductivity of Apollo 14 fines,” Lunar and Planetary Science Conference Proceedings, vol. 3, p. 2611, 1972.

C. J. Cremers, R. C. Birkebak, and J. E. White, “Thermal characteristics of the lunar surface layer,” International Journal of Heat and Mass Transfer, vol. 15, no. 5, pp. 1045–1055, May 1972.

D. A. Ochoa, B. M. Miranda, B. C. Conger, and L. A. Trevino, “Lunar EVA Thermal Environment Challenges,” SAE Transactions, vol. 115, pp. 492–505, 2006.

D. A. Paige and M. A. Siegler, “New Constraints on Lunar Heat Flow Rates from LRO Diviner Lunar Radiometer Experiment Polar Observations,” vol. 47, p. 2753, Mar. 2016.

D. A. Paige et al., “Diviner Lunar Radiometer Observations of Cold Traps in the Moon’s South Polar Region,” Science, vol. 330, no. 6003, pp. 479–482, Oct. 2010.

D. E. Lee, “Gateway Destination Orbit Model: A Continuous 15 year NRHO Reference Trajectory”, NTRS 20190030294, Aug. 2019

D. E. Smith et al., “The Lunar Orbiter Laser Altimeter Investigation on the Lunar Reconnaissance Orbiter Mission,” 2008.

D. G. Gilmore, and R Collins. “Thermal Design Analysis.” Chapter 15, Spacecraft Thermal Control Handbook, 2nd ed. El Segundo, Calif. : Reston, Va.: Aerospace Press ; American Institute of Aeronautics and Astronautics, 2002.

David A. Glenar, et. al., “Earthshine as an Illumination Source at the Moon”, Icarus, Volume 321, p. 841-856, March 2019.

E. Bowman-Cisneros and E. Eliason, “LROC RDR Data Products Software Interface Specification.” Arizona State University, 08-Mar-2011. http://lroc.sese.asu.edu/data/LRO-L-LROC-5-RDR-V1.0/LROLRC_2001/DOCUMENT/RDRSIS.PDF

E. Sefton-Nash et al., “Evidence for ultra-cold traps and surface water ice in the lunar south polar crater Amundsen,” Icarus, vol. 332, pp. 1–13, Nov. 2019.

Feingold, A. and Gupta, K.G. (1970) "New analytical approach to the evaluation of configuration factors in radiation from spheres and infinitely long cylinders," J. Heat Transfer, vol. 92, no. 1, pp. 69-76, February. (http://www.thermalradiation.net/sectionc/C-125.html)

G. Heiken, D. Vaniman, and B. French, Lunar sourcebook: A user's guide to the Moon. New York: Cambridge University Press, 1991.

G. Schunk, S. Sutherlin and O. Kornberg, "Constellation Thermal Overview-Altair", Thermal and Fluid Analysis Workshop (TFAWS), MSFC, 2009.

G. Wei, X. Li, and S. Wang, "Inversions of subsurface temperature and thermal diffusivity on the Moon based on high frequency of Chang'E-1 microwave radiometer data," Icarus, vol. 275, pp. 97–106, Sep. 2016.

G. Wei, X. Li, and S. Wang, "Thermal behavior of regolith at cold traps on the Moon′ s south pole: Revealed by Chang′E-2 microwave radiometer data," Planetary and Space Science, vol. 122, pp. 101–109, Mar. 2016.

Giorgini, Jon, et al., "HORIZONS user Manual" Version 4.50, December 2019. (https://ssd.jpl.nasa.gov/?horizons_doc)

H. Rana, V. Laneve, P. Hager, and T. Tirolien, "Thermal Modelling of Luna 27 Landing Site," p. 10, 2017.

HI-SEAS, 2019, Hawai'I Space Exploration Analog and Simulator website (https://hi-seas.org/?p=1278)

Howell, J.H. (2019) personal communication, 2019.09.30

J. Gaier, S. Ellis, and N. Hanks, "Thermal Optical Properties of Lunar Dust Simulants and Their Constituents," in 3rd AIAA Atmospheric Space Environments Conference, Honolulu, Hawaii, 2011.

J. F. Gasbarre, R. M. Amundsen, S. Scola, F. B. Leahy, and J. R. Sharp, "Ground Plane and Near-Surface Thermal Analysis for NASA's Constellation Programs," p. 13, 2008.

J. Feng, M. A. Siegler, and P. O. Hayne, "New Constraints on Thermal and Dielectric Properties of Lunar Regolith from LRO Diviner and CE-2 Microwave Radiometer," Journal of Geophysical Research: Planets, vol. 125, no. 1, p. e2019JE006130, 2020, doi: 10.1029/2019JE006130.

J. Feng, M. A. Siegler, P. O. Hayne, and D. T. Blewett, "Lunar Regolith Properties Constrained by LRO Diviner and Chang'e-2 Microwave Radiometer Data," presented at the Lunar and Planetary Science Conference, 2019, vol. 50, p. 3176.

J. Feng, M. Siegler, and P. Hayne, "2786.pdf," presented at the 51st Lunar and Planetary Science Conference, 2020, Accessed: Apr. 28, 2020. [Online]. Available: https://www.hou.usra.edu/meetings/lpsc2020/pdf/2786.pdf.

J. L. Linsky, "Models of the lunar surface including temperature-dependent thermal properties," Icarus, vol. 5, no. 1, pp. 606–634, Jan. 1966.

J. P. Williams et al, “The Global Surface Temperatures of the Moon as Measured by the Diviner Lunar Radiometer Experiment”, Icarus, Elsevier, 2016.

J. P. Williams, et al, “Seasonal Variations in South Polar Temperatures on the Moon”, 50th Lunar and Planetary Science Conference 2019, LPI Contribution #2132, 2019.

J. R. Gaier, J. Siamidis, and E. M. G. Larkin, “Effect of Simulated Lunar Dust on the Properties of Thermal Control Surfaces,” Journal of Spacecraft and Rockets, vol. 47, no. 1, pp. 147–152, 2010.

J. R. Smith. “Gateway Passive Thermal Guidelines and Model Utilization – IAC4”, Oct. 2019

James R. Gaier, “Studies of Simulated Lunar Dust on the Properties of Thermal-Control Surfaces,” Journal of Spacecraft and Rockets 50, no. 4 (July-August 2013): 848.

K. Watson, “I. The thermal conductivity measurements of selected silicate powders in vacuum from 150°-350° K. II. An interpretation of the Moon’s eclipse and lunation cooling as observed through the Earth’s atmosphere from 8-14 microns,” phd, California Institute of Technology, 1964.

Lienhard IV, J.H., Lienhard V, J.H. (2019) A Heat Transfer Textbook, 5th ed., Phlogiston Press, Cambridge, MA. p.558. (https://ahtt.mit.edu/)

Liskowsky, D.R., Seitz, W.W. (2014) Human Integration Design Handbook, NASA/SP-2010-3407/REV1, eds., Appendix B, p. 1167. (https://www.nasa.gov/sites/default/files/atoms/files/human_integration_design_handbook_revision_1.pdf)

M. B. K. Langseth, “In-situ measurements of lunar heat flow,” 1977.

M. G. Langseth, S. J. Keihm, and K. Peters, “Revised lunar heat-flow values.,” Lunar and Planetary Science Conference Proceedings, vol. 3, p. 3143, Apr. 1976.

M. K. Barker, E. Mazarico, G. A. Neumann, M. T. Zuber, J. Haruyama, and D. E. Smith, “A new lunar digital elevation model from the Lunar Orbiter Laser Altimeter and SELENE Terrain Camera,” Icarus, 2015.

M. Kharseh, “Solar Radiation Calculation,” Jun-2018, doi: http://dx.doi.org/10.13140/RG.2.2.34480.05129.

M. Langseth, S. Keihm, and J. Chute Jr., “Heat-flow experiment. In Apollo 17 Preliminary Science Report.,” NASA SP-330.

M. Siegler and D. Paige, “Lunar Global Heat Flow: Predictions and Constraints,” presented at the Lunar Science for Landed Missions Workshop, NASA Ames, 2018.

M. Siegler, D. Paige, J.-P. Williams, and B. Bills, “Evolution of lunar polar ice stability,” Icarus, vol. 255, pp. 78–87, Jul. 2015.

M.G. Langseth Jr., S.J. Keihm, and J.L. Chute Jr. (1973) “Heat-flow experiment. In Apollo 17

Martinez, I. (2019) Radiative View Factors, p.13 (http://webserver.dmt.upm.es/~isidoro/tc3/Radiation%20View%20factors.pdf).

Max Planck, “The Theory of Heat Radiation”, P. Blakiston’s Son and Co., Philadephia, 1914, pages 86 and168.

P. B. Hager, “Dynamic thermal modeling for moving objects on the Moon,” Technische Universität München, Germany, 2013.

P. Cignoni, M. Callieri, M. Corsini, M. Dellepiane, F. Ganovelli, G. Ranzuglia, “MeshLab: an Open-Source Mesh Processing Tool,” Sixth Eurographics Italian Chapter Conference, page 129-136, 2008. Available: http://www.meshlab.net/.

P. Hager, U. Walter, and D. M. Klaus, “Impact of lunar dust on radiator design for Moon bases and rovers,” in 43rd International Conference on Environmental Systems, American Institute of Aeronautics and Astronautics.

P. Metzger, S. Anderson, and A. Colaprete, “Experiments Indicate Regolith is Looser in the Lunar Polar Regions than at the Lunar Landing Sites,” presented at the Earth & Space 2018 Conference (ASCE), 2018.

P. O. Hayne et al., “Global Regolith Thermophysical Properties of the Moon from the Diviner Lunar Radiometer Experiment: Lunar Regolith Thermophysical Properties,” J. Geophys. Res. Planets, vol. 122, no. 12, pp. 2371–2400, Dec. 2017.

P. Reiss, “In-Situ Thermal Extraction of Volatiles from Lunar Regolith,” Technical University of Munich, 2018.

Paul O. Hayne, et al, “Global regolith thermophysical properties of the Moon from the Diviner Lunar Radiometer Experiment”, 2017.

Planetary Fact Sheet, NSSDCA-NASA, https://nssdc.gsfc.nasa.gov/planetary/factsheet/moonfact.html

Preliminary Science Report”, NASA SP-330, pp. 9-1 to 9-24, 1973.

R. A. Schowengerdt, Remote Sensing: Models and Methods for Image Processing. Chapter 2 “Optical Radiation Models” p. 52. Elsevier, 2006.

R. C. Birkebak, “Thermal Radiation Properties of Lunar Materials from the Apollo Missions,” in Advances in Heat Transfer, vol. 10, J. P. Hartnett and T. F. Irvine, Eds. Elsevier, 1974, pp. 1-37.

R. Christie, D. Plachta, and M. Hasan, “Transient Thermal Model and Analysis of the Lunar Surface and Regolith for Cryogenic Fluid Storage,” Aug. 2008.

R. Durkee and J. Harris R., “Lunar dust deposition effects on the solar absorptance of thermal control materials,” in 6th Thermophysics Conference, 0 vols., American Institute of Aeronautics and Astronautics, 1971.

R. Woods-Robinson, M. A. Siegler, and D. A. Paige, “A Model for the Thermophysical Properties of Lunar Regolith at Low Temperatures,” Journal of Geophysical Research: Planets, vol. 124, no. 7, pp. 1989–2011, 2019.

Richard C. Birkebak, “Thermophysical Properties of Lunar Materials: Part I Thermal Radiation Properties of Lunar Materials from the Apollo Missions”, Advances in Heat Transfer, Vol. 10, Academic Press, 1974.

Rick van Hattem, “numpy-stl 2.10.1” [Online]. March 2019, Available: https://pypi.org/project/numpy-stl/.

S. Nagihara, W. S. Kiefer, P. T. Taylor, D. R. Williams, and Y. Nakamura, “Examination of the Long-Term Subsurface Warming Observed at the Apollo 15 and 17 Sites Utilizing the Newly Restored Heat Flow Experiment Data From 1975 to 1977,” Journal of Geophysical Research: Planets, vol. 123, no. 5, pp. 1125–1139, May 2018.

Sparrow, E.M.; Miller, G.B.; and Jonsson, V.K., 1962, "Radiative effectiveness of annular- finned space radiators, including mutual irradiation between radiator elements," J. Aerospace Sci., vol. 29, no. 11, pp. 1291-1299. (http://www.thermalradiation.net/sectionc/C-77.html).

Stephen J. Keihm, “Interpretation of the Lunar Microwave Brightness Temperature Spectrum: Feasibility of Orbital Heat Flow Mapping”, Icarus 60, p. 568-589, 1984.

Stuart Ross Taylor, “Lunar Science: a Post-Apollo View”, Lunar Science Institute, Pergamon Press, New York, p. 64. ISBN 978-0080182742, 1975. http://articles.adsabs.harvard.edu//full/1975lspa.book.....T/0000001,004.html

T. J. Warren, O. King, N. E. Bowles, E. Sefton-Nash, R. Fisackerly, and R. Trautner, “The Oxford 3D Thermophysical Model with Application to the Lunar PROSPECT Mission,” Lunar and Planetary Science Conference, p. 2040, Mar. 2019.

T.-Y. Park, J.-J. Lee, J.-H. Kim, and H.-U. Oh, “Preliminary Thermal Design and Analysis of Lunar Lander for Night Survival,” 2018.

Timothy D. Panczak, Steven G. Ring, Mark J. Welch, David Johnson, Brent A. Cullimore, and Douglas P. Bell, “Thermal Desktop User’s Manual, CAD Thermal Analysis and Design Version 6.0.” C&R Technologies, Inc. (“CRTech”), 2017.

W. F. Fountain, et.al, “Observational and Theoretical Temperatures for a Total Lunar Eclipse”, “The Moon”, p421-437, 1976]

W. Zhang, “Lunar subsurface temperature profile modelling based on CE-1 and CE-2,” OGS / Bollettino di Geofisica Teoricae Applicata, vol. 60, p. 489-516, Sep. 2019.

APPENDIX A
ACRONYMS AND ABBREVIATIONS AND GLOSSARY OF TERMS

A1.0 ACRONYMS AND ABBREVIATIONS

TABLE A1-1 ACRONYMS AND ABBREVIATIONS

AU	Astronomical Unit
CR	Change Request
D	diameter
deg	Degrees
DEM	Digital Elevation Model
DSNE	Design Specification for Natural Environments
F	Fahrenheit
FD	Finite Difference
FEM	Finite Element Model
FWD	Forward Work
GDR	Gridded Data Record
GMT	Greenwich Mean Time
GRC	Glenn Research Center
GUI	Graphical User Interface
HLS	Human Landing System
HR	Heat Rate
IR	Infrared
JPL	Jet Propulsion Laboratory
JSC	Johnson Space Center
K	Kelvin
km	kilometer
LEM	Lunar Excursion Module
LLO	Low Lunar Orbit
LOLA	Lunar Orbiter Laser Altimeter

TABLE A1-1 ACRONYMS AND ABBREVIATIONS

LRO	Lunar Reconnaissance Orbiter
LROC	Lunar Reconnaissance Orbiter Camera
LRV	Lunar Rover Vehicle
L-TAG	Lunar Thermal Analysis Guidebook
L-TETT	Lunar Thermal Environments Task Team
LWIR	Long-wave Infrared Radiation
m	meter
MSFC	Marshall Space Flight Center
NRHO	Near Rectilinear Halo Orbit
OLR	Outgoing Long-wave Radiation
OPR	Office of Primary Responsibility
PDS	Planetary Data System
PSR	Permanently Shaded Region
PSR	Perpetually Shaded Region
R	radius
RA	Right Ascension
RAAN	Right Ascension of Ascending Node
RAS	Right Ascension of the Sun
RDR	Reduced Data Record
SHOE	Shadow Hiding Opposition Effect
SLS	Space Launch Systems
SPEC	Specification
TBD	To Be Determined
TBR	To Be Resolved
TD	Thermal Desktop
TFAWS	Thermal and Fluids Analysis Workshop

TABLE A1-1 ACRONYMS AND ABBREVIATIONS

UG	User's Guide
VBA	Visual Basic for Applications
WCS	World Coordinate System

A2.0 GLOSSARY OF TERMS

Term	Description
Flight	This is the sequence of events that takes place between liftoff and landing of a transportation vehicle.

APPENDIX B
OPEN WORK

B1.0 TO BE SPECIFIED

The table To Be Specified Items lists the specific To Be Specified (TBS) items in the document that are not yet known. The TBS is inserted as a placeholder wherever the required data is needed and is formatted in bold type within carets. The TBS item is numbered based on the document number (i.e., **<TBS-xxxx-00x-00x>** is the first undetermined item assigned in the document). As each TBS is resolved, the updated text is inserted in each place that the TBS appears in the document and the item is removed from this table. As new TBS items are assigned, they will be added to this list in accordance with the above described numbering scheme. Original TBSs will not be renumbered.

TABLE B1-1 TO BE DETERMINED ITEMS

TBD	Section	Description
TBS-xxxx-00x-001		

B2.0 FORWARD WORK

The table Forward Work lists the specific Forward Work (FWD) issues in the document that are not yet known. The FWD is inserted as a placeholder wherever the required data is needed and is formatted in bold type within carets. The FWD issue is numbered based on the document number (i.e., **<FWD-xxxx-00x-00x>** is the first forward work assigned in the document). As each FWD is resolved, the updated text is inserted in each place that the FWD appears in the document and the issue is removed from this table. As new FWD issues are assigned, they will be added to this list in accordance with the above described numbering scheme. Original FWDs will not be renumbered.

TABLE B2-1 FORWARD WORK ITEMS

TBR	Section	Description
FWD-xxxx-00x-001		

APPENDIX C
EXAMPLE MODELS/CASE STUDIES

APPENDIX D
DERIVATIONS

APPENDIX E
ASCENT/DESCENT ATTITUDE COMPUTER CODE

Ascent/Descent

The following MATLAB® script is referenced Section 8.3 of this document. Note that this script has not been checked out by an independent user on an independent model, and may contain errors.

MATLAB® Script for Ascent/Descent Section

```
%%Import the longitude, latitude, altitude, and time data from you source.

%Pulling the cartesian cooridinates of the Sun from the Moon's perspective
%These coordinates are only used to find initial location of Sun
cart = xlsread();
%Pulling the time, lat, long, and altitude of the lander.
sphereical = xlsread);

%% Clearing everything but the data called out above
clc; clearvars -except cart sphereical;

%%
% converting cartesian coordinates to sphereical for Sun's location from
% Moon perspective
%This is used to calculated the right ascension and declination of Sun

%The code below is used because the RA angle depends on what quadrant of
%sky the Sun is in. An image is included in the report that helps
%demonstrate this.
if cart(1,1) > 0 && cart(1,2) > 0;
   RA_prime_meridian = atand(cart(1,2)/cart(1,1));
elseif cart(1,1) < 0 && cart(1,2) > 0;
   RA_prime_meridian = atand(cart(1,1)/cart(1,2))+90;
elseif cart(1,1) < 0 && cart(1,2) < 0;
   RA_prime_meridian = atand(cart(1,2)/cart(1,1))+180;
else cart(1,1) > 0 && cart(1,2) < 0;
   RA_prime_meridian = atand(cart(1,1)/cart(1,2))+270;
end

RA_sun = atand(cart(1,3)/(sqrt(cart(1,1)^2+cart(1,2))));

%Adjusting the RA prime meridian (RA PM) in thermal desktop offsets the
%vernal equinox (x-axis) clockwise from the lat/long origin (0,0). If the
%RA PM is set to 50deg, then the vernal equinox will be 50deg clockwise
%from a satelite (0,0) origin point. If the RA Sun is set to zero, then the
%subsolar point will be on the vernal equinox. Be aware that the RA Sun in
%thermal Desktop is not the same as declination.

%% Separating out the components of the descent into individual variables
Timelong = sphereical(:,1);
Latlong = sphereical(:,2)*(180/pi);
Longlong = sphereical(:,3)*(180/pi);
Altlong = sphereical(:,4)-sphereical(end,4);

%Downsizing the data size to a managable amount of points
Downsize = 2328;
Time2 = downsample(Timelong,Downsize,1);
Lat2 = downsample(Latlong,Downsize,1);
Long2 = downsample(Longlong,Downsize,1);
```

```
Alt2 = downsample(Altlong,Downsize,1);


%doing this cause there is an error at end of landing. Technically the
%longitude changes as the lander has touched down and it causes the second
%to last time step to be out of wack. If still curious look at longitude
%time graph and zoom in to last 30 seconds on x and .00045 range on y

if (Time2(end,1)-Timelong(end,1)) > 30

   Time2(end+1,:) = Timelong(end,1);
   Lat2(end+1,:) = Latlong(end,1);
   Long2(end+1,:) = Longlong(end,1);
   Alt2(end+1,:) = Altlong(end,1);

end
% Converting altitude from meters to kilameters
Alt2(:) = Alt2/1000;
%Re-compiling all the components of descent to enter into TD
data2 = [Time2(:),Lat2(:),Long2(:),Alt2(:)];

%%
clearvars LatDiff LongDiff
%Starting to calculate the X-rotation. Need to know the change in latitude
%and longitude between each timestep
switch1 = 1;

%This code is used to convert the longitude into a constant
%increase/decrease in the numbers. Longitude can be represented two ways
%(180 = -180) This makes sure that when calculating the difference, there
%are no misleading numbers. e.g. in terms of longitude, 180 is only 10
%degrees away from -170, but taking the straight difference will give a
%value of 350 which would be misleading. This code adds 360 to any negative
%longitude values

for i = 1:length(Long2);
   if Long2(i) > 0 && switch1 == 1;
      Long3(i,:) = Long2(i);
   else
      Long3(i:length(Long2),:) = Long2(i:end)+360;
      switch1 = 0;
   end
end


for i = 1:length(Lat2)-1;
   LatDiff(i,:) = Lat2(i+1) - Lat2(i);
   LongDiff(i,:) = Long3(i+1) - Long3(i);
end

%done to keep the arrays the same size
LatDiff(end+1) = LatDiff(end);
LongDiff(end+1) = LongDiff(end);

clearvars i switch1
%%

%For this section to work, ensure that the axis that needs to face the
%surface of the Moon is indeed facing the Moon. This section calculates the
%X-axis rotation to ensure that the Z-axis faces the velocity vector

Xrot(:,2) = Time2(:);
```

```
for j = 1:length(LatDiff);
   if LongDiff(j) > 0 && LatDiff(j) > 0;
      Xrot(j,1) = atand(abs(LongDiff(j)/LatDiff(j)));
   elseif LongDiff(j) > 0 && LatDiff(j) < 0;
      Xrot(j,1) = atand(abs(LatDiff(j)/LongDiff(j)))+90;
   elseif LongDiff(j) < 0 && LatDiff(j) < 0;
      Xrot(j,1) = atand(abs(LongDiff(j)/LatDiff(j)))+180;
   elseif LongDiff(j) < 0 && LatDiff(j) > 0;
      Xrot(j,1) = atand(abs(LatDiff(j)/LongDiff(j)))+270;
   end
end
Xrot(end,1) = Xrot(end-1,1);

clearvars j
%%
% RA_prime_meridian = 0;
%This section of code is the rotation matrices. It can transform any number
%of rotations down to 3 base rotations.
%For Astro to have the x-axis facing the Moons surface with the Z-axis
%facing the velocity vector and having a 45deg tilt towards the surface.
%Current method rotates about Z,Y,X,Y axis to get the lander's Z axis
%pointing towards the velocity vector with a 45 degree tilt so the NDL can
%track the surface

%Below is the result of a 3X3 identity matrix multiplied by Z,Y,X rotation
%matrices in that order. Alpha is for X rotation, beta is for
%Y rotation and gamma is for Z rotation
% cos(gamma)cos(beta)   cos(gamma)sin(beta)sin(alpha)-sin(gamma)cos(alpha)
%          sin(gamma)sin(alpha)+cos(gamma)sin(beta)cos(alpha)
% sin(gamma)cos(beta)   cos(gamma)cos(alpha)+sin(gamma)sin(beta)sin(alpha)
%          sin(gamma)sin(beta)cos(alpha)-cos(gamma)sin(alpha)
%-sin(beta)            cos(beta)sin(alpha)
%          cos(beta)cos(alpha)


for i = 1:length(Time2);
   if i == length(Time2);
      Matrix(:,:,i) = eye(3)*rotmatz(Long2(i))*rotmaty(Lat2(i));
   else

      Matrix(:,:,i) = eye(3)*rotmatz(Long2(i)+RA_prime_meridian)*...
         rotmaty(-Lat2(i))*rotmatx(-Xrot(i))*rotmatz(180)*rotmaty(45);

   end

      %***Could be some errors when trying to use arcsin cause it has a
      %range of +-90 and will not work if angle is greater than 90. A
      %similar problem can come from using arccos cause it does not have
      %any negative values...

      %Solve arctan2 for the following
      beta(i,:) = asind(-Matrix(3,1,i));
      if Matrix(3,3,i) > 0;
         alpha(i,:) = atand(Matrix(3,2,i)/Matrix(3,3,i));
      elseif Matrix(3,3,i) < 0 && Matrix(3,2,i) >= 0;
         alpha(i,:) = atand(Matrix(3,2,i)/Matrix(3,3,i))+180;
      elseif Matrix(3,3,i) < 0 && Matrix(3,2,i) < 0;
         alpha(i,:) = atand(Matrix(3,2,i)/Matrix(3,3,i))-180;
      elseif Matrix(3,3,i) == 0 && Matrix(3,2,i) > 0;
         alpha(i,:) = 90;
      elseif Matrix(3,3,i) == 0 && Matrix(3,2,i) < 0;
         alpha(i,:) = -90;
```

```
    end


    if Matrix(1,1,i) > 0;
       gamma(i,:) = atand(Matrix(2,1,i)/Matrix(1,1,i));
    elseif Matrix(1,1,i) < 0 && Matrix(2,1,i) >= 0;
       gamma(i,:) = atand(Matrix(2,1,i)/Matrix(1,1,i))+180;
    elseif Matrix(1,1,i) < 0 && Matrix(2,1,i) < 0;
       gamma(i,:) = atand(Matrix(2,1,i)/Matrix(1,1,i))-180;
    end

end
```

APPENDIX F
OTHER COMPUTER CODE

CONFIGURATION FACTORS

The following Python 3.7.3 code snippets were used to calculate the configuration factor data presented in section 9.3.1 and 9.3.2 of this document. Each function requires a 1-D ground plane radius array plus other input data as specified in the function.

Description: Ground plane to the outer surface of a cylinder (radius r_2, height h) at a distance L above a ground plane (a planar disk of radius r_1) – Configuration Factor $F_{1-2,3}$

```
def config(ndp,r1,r2,h,L):

    #input ************************************************************
    # ndp   number of data points
    # r1    ground plane radius array [m]
    # r2    cylinder radius [m]
    # h     cylinder height [m]
    # L     distance cylinder is displaced from ground plane [m]
    #output ***********************************************************
    # F123  configuration factor array [-]

    F12 = np.zeros(ndp)
    F13 = np.zeros(ndp)
    F123 = np.zeros(ndp)

    for i in range(ndp):
        # configuration factor: ground plane to spacecraft side
        # source: Howell, J.R., personal communication, 2019.09.30.
        R = r2/r1[i]
        H1 = L/r1[i]
        H2 = (h+L)/r1[i]
        A1 = (H1**2)+(R**2)-1.0
        A2 = (H2**2)+(R**2)-1.0
        B1 = (H1**2)-(R**2)+1.0
        B2 = (H2**2)-(R**2)+1.0

        C00 = 1.0/(2.0*np.pi)
        C11 = B1/(8.0*R*H1)
        C12 = np.arccos(A1/B1)
        C13 = (1.0/(2.0*H1))*np.sqrt((((A1+2)**2)/R**2)-4.0)* \
              np.arccos(A1*R/B1)
        C14 = (A1/(2.0*R*H1))*np.arcsin(R)
        F1 = C11+C00*(C12-C13-C14)

        C21 = B2/(8.0*R*H2)
        C22 = np.arccos(A2/B2)
        C23 = (1.0/(2.0*H2))*np.sqrt((((A2+2)**2)/R**2)-4.0)* \
              np.arccos(A2*R/B2)
        C24 = (A2/(2.0*R*H2))*np.arcsin(R)
        F2 = C21+C00*(C22-C23-C24)

        F12[i] = ((2.0*R)/(1.0-(R**2)))*(H2*F2 - H1*F1)

        # configuration factor: ground plane to spacecraft lower surface
        # source: Lienhard, Lienhard, A Heat Transfer Textbook, 5th ed.
        #         https://ahtt.mit.edu/
        R1 = r1[i]/L
        R2 = r2/L
        X = 1.0+((1.0+(R2**2))/(R1**2))
        F13[i] = 0.5*(X-np.sqrt((X**2)-(4.0*(R2/R1)**2)))

        F123[i] = F12[i] + F13[i]
    return F123
```

Description: Outer surface of a cylinder (radius r_2, height h) at a distance L above a ground plane (a planar disk of radius r_1) to the ground plane – Configuration Factor $F_{2,3-1}$

```
def config(ndp,r1,r2,h,L):

    #input ************************************************************************
    # ndp   number of data points
    # r1    ground plane radius array [m]
    # r2    cylinder radius [m]
    # h     cylinder height [m]
    # L     distance cylinder is displaced from ground plane [m]
    #output ***********************************************************************
    # F231  configuration factor array [-]

    A2 = 2.0*np.pi*r2*h
    A3 = np.pi*r2*r2
    A23 = A2 + A3

    Aratio123 = np.zeros(ndp)
    for i in range(ndp):
        Aratio123[i] = np.pi*r1[i]*r1[i]/A23

    F12 = np.zeros(ndp)
    F13 = np.zeros(ndp)
    F231 = np.zeros(ndp)

    for i in range(ndp):
        # configuration factor: ground plane to spacecraft side
        # source: Howell, J.R., personal communication, 2019.09.30.
        R = r2/r1[i]
        H1 = L/r1[i]
        H2 = (h+L)/r1[i]
        A1 = (H1**2)+(R**2)-1.0
        A2 = (H2**2)+(R**2)-1.0
        B1 = (H1**2)-(R**2)+1.0
        B2 = (H2**2)-(R**2)+1.0

        C00 = 1.0/(2.0*np.pi)
        C11 = B1/(8.0*R*H1)
        C12 = np.arccos(A1/B1)
        C13 = (1.0/(2.0*H1))*np.sqrt((((A1+2)**2)/R**2)-4.0)* \
              np.arccos(A1*R/B1)
        C14 = (A1/(2.0*R*H1))*np.arcsin(R)
        F1 = C11+C00*(C12-C13-C14)

        C21 = B2/(8.0*R*H2)
        C22 = np.arccos(A2/B2)
        C23 = (1.0/(2.0*H2))*np.sqrt((((A2+2)**2)/R**2)-4.0)* \
              np.arccos(A2*R/B2)
        C24 = (A2/(2.0*R*H2))*np.arcsin(R)
        F2 = C21+C00*(C22-C23-C24)

        F12[i] = ((2.0*R)/(1.0-(R**2)))*(H2*F2 - H1*F1)

        # configuration factor: ground plane to spacecraft lower surface
        # source: Lienhard, Lienhard, A Heat Transfer Textbook, 5th ed.
        #         https://ahtt.mit.edu/
        R1 = r1[i]/L
        R2 = r2/L
        X = 1.0+((1.0+(R2**2))/(R1**2))
        F13[i] = 0.5*(X-np.sqrt((X**2)-(4.0*(R2/R1)**2)))

        F123 = F12[i] + F13[i]
        F231[i] = Aratio123[i]*F123
    return F231
```

Description: Outer surface of a cylinder (radius r_1, height h) to the ground plane (a planar disk of radius r_2) – Configuration Factor F_{1-2}

```
def config(ndp,r1,r2,h):

    #input ***************************************************************
    # ndp   number of data points
    # r1    cylinder radius [m]
    # r2    ground plane radius array [m]
    # h     cylinder height [m]
    #output **************************************************************
    # F12   configuration factor array [-]

    F12 = np.zeros(ndp)

    for i in range(ndp):
        # configuration factor:
        # Outer surface of cylinder to annular disk at end of cylinder *******
        # source: Sparrow, Miller, Jonsson, J. Aero. Sci. 29:11, 1291-1299
        # source: http://www.thermalradiation.net/sectionc/C-77.html

        R = r1/r2[i]
        H = h/r2[i]
        A = (H**2)+(R**2)-1.0
        B = (H**2)-(R**2)+1.0

        C0 = B/(8.0*R*H)
        C1 = 1/(2.0*np.pi)
        C2 = np.arccos(A/B)
        C3 = (1.0/(2.0*H))*np.sqrt(((A+2)*(A+2)/(R*R))-4.0)*np.arccos(A*R/B)
        C4 = (A/(2.0*R*H))*np.arcsin(R)

        F12[i] = C0+C1*(C2-C3-C4)
    return F12
```

Description: Ground plane (a planar disk of radius r_2) to the outer surface of a cylinder (radius r_1, height h) – Configuration Factor F_{2-1}

```
def config(ndp,r1,r2,h):

    #input ***************************************************************
    # ndp   number of data points
    # r1    cylinder radius [m]
    # r2    ground plane radius array [m]
    # h     cylinder height [m]
    #output **************************************************************
    # F21   configuration factor array [-]

    F21 = np.zeros(ndp)
    A1 = 2.0*np.pi*r1*h

    for i in range(ndp):
        # configuration factor:
        # Outer surface of cylinder to annular disk at end of cylinder *******
        # source: Sparrow, Miller, Jonsson, J. Aero. Sci. 29:11, 1291-1299
        # source: http://www.thermalradiation.net/sectionc/C-77.html

        R = r1/r2[i]
        H = h/r2[i]
        A = (H**2)+(R**2)-1.0
        B = (H**2)-(R**2)+1.0

        C0 = B/(8.0*R*H)
        C1 = 1/(2.0*np.pi)
```

```
        C2 = np.arccos(A/B)
        C3 = (1.0/(2.0*H))*np.sqrt(((A+2)*(A+2)/(R*R))-4.0)*np.arccos(A*R/B)
        C4 = (A/(2.0*R*H))*np.arcsin(R)

        F12 = C0+C1*(C2-C3-C4)

        # reciprocity relation
        A2 = np.pi*(r2[i]**2-r1**2)
        Aratio = A1/A2
        F21[i] = Aratio*F12
    return F21
```

Description: Outer surface of a sphere located at a distance h above the ground plane to the ground plane (a planar disk of radius r_2) – Configuration Factor F_{1-2}

```
def config(ndp,h,r):

    #input ***************************************************************
    # ndp   number of data points
    # h     distance above the ground plane [m]
    # r     ground plane radius array [m]
    #output **************************************************************
    # F12   configuration factor array [-]

    F12 = np.zeros(ndp)

    # configuration factor: Sphere to coaxial disk
    # source: http://www.thermalradiation.net/sectionc/C-125.html
    F12 = np.zeros(ndp)
    C0 = 1.0/2.0
    for i in range(ndp):
        rr = r[i]/h
        xx = 1.0/np.sqrt(1.0 + rr**2)
        F12[i] = C0*(1.0 - xx)
    return F12
```

Description: Ground plane (a planar disk of radius r_2) to the outer surface of a sphere located at a distance h above the ground plane – Configuration Factor F_{2-1}

```
def config(ndp,h,rs,r):

    #input ***************************************************************
    # ndp   number of data points
    # h     distance above the ground plane [m]
    # r     ground plane radius array [m]
    #output **************************************************************
    # F21   configuration factor array [-]

    F21 = np.zeros(ndp)

    # configuration factor: Sphere to coaxial disk
    # source: http://www.thermalradiation.net/sectionc/C-125.html
    C0 = 1.0/2.0
    for i in range(ndp):
        rr = r[i]/h
        xx = 1.0/np.sqrt(1.0 + rr**2)
        F12 = C0*(1.0 - xx)

        A1 = 4.0*np.pi*rs*rs
        A2 = np.pi*r[i]*r[i]
        F21[i] = (A1/A2)*F12
    return F21
```

Description: Outer surface of a hemisphere (radius r_1) to the ground plane (a planar annular disk of radius r_2) – Configuration Factor F_{1-2}

```
def config(ndp,r1,r2):

    #input ***************************************************************
    # ndp   number of data points
    # r1    hemisphere radius [m]
    # r2    ground plane radius array [m]
    #output **************************************************************
    # F12   configuration factor array [-]

    F12 = np.zeros(ndp)

    # configuration factor: Hemisphere of radius r1 to a
    # concentric equatorial disc of radius r2, where r2>r1
    # source:
    # http://webserver.dmt.upm.es/~isidoro/tc3/Radiation%20View%20factors.pdf

    C0 = 1.0/4.0
    C1 = 1.0/(2.0*np.pi)
    for i in range(ndp):
        rr = r1/r2[i]
        xx = np.sqrt((1.0/rr**2)-1.0)
        F12[i] = C0 - C1*(xx - (xx**2 - 1.0)*np.arcsin(rr))
    return F12
```

Description: Ground plane (a planar annular disk of radius r_2) to the outer surface of a hemisphere (radius r_1) – Configuration Factor F_{2-1}

```
def config(ndp,r1,r2):

    #input ***************************************************************
    # ndp   number of data points
    # r1    hemisphere radius [m]
    # r2    ground plane radius array [m]
    #output **************************************************************
    # F12   configuration factor array [-]

    F21 = np.zeros(ndp)

    # configuration factor: Hemisphere of radius r1 to a
    # concentric equatorial disc of radius r2, where r2>r1
    # source:
    # http://webserver.dmt.upm.es/~isidoro/tc3/Radiation%20View%20factors.pdf
    C0 = 1.0/4.0
    C1 = 1.0/(2.0*np.pi)
    for i in range(ndp):
        rr = r1/r2[i]
        xx = np.sqrt((1.0/rr**2)-1.0)
        F12 = C0 - C1*(xx - (xx**2 - 1.0)*np.arcsin(rr))

        A1 = 2.0*np.pi*r1**2
        A2 = np.pi*(r2[i]**2-r1**2)
        F21[i] = (A1/A2)*F12
    return F21
```

Description: Outer surface of a sphere to an infinite ground plane (an infinite planar disk – Configuration Factor $F_{1-\infty}$

```
F1inf = 0.5
```

Description: Outer surface of a "small" sphere (radius r_1) to a "much larger" sphere (radius r_2) where the centers of the two spheres are separated by a distance h – Configuration Factor F_{1-2}

```
def config(ndp,h,r2):

    #input ************************************************************
    # ndp   number of data points
    # h     array: distance between the centers of the 2 spheres [m]
    # r2    radius of larger sphere [m]
    #output ***********************************************************
    # F12   configuration factor array [-]

    F12 = np.zeros(ndp)

    # configuration factor: small sphere to large sphere ****************
    # source:
    # http://webserver.dmt.upm.es/~isidoro/tc3/Radiation%20View%20factors.pdf
    for i in range(ndp):
        H = h[i]/r2
        F12[i] = 0.5*(1.0 - np.sqrt(1.0-(1.0/(H**2))))
    return F12
```

THERMAL DESKTOP MESH IMPORTING EXAMPLE

```
Sub Mesh_Auto_Add3DFace()
    'Create AutoCAD® Surfaces from on x y z vectors of a triangular mesh
    'read from an input file
    'The .txt input file has the following format:
    'x y z for point_1 of Face_n
    'x y z for point_2 of Face_n
    'x y z for point_3 of Face_n
    ' ....

    filename = "..\Process_stl\output\vectors\vector_points.txt"

    'Declarations
    Dim pt0(0 To 2) As Double
    Dim pt1(0 To 2) As Double
    Dim pt2(0 To 2) As Double
    Dim x As Double
    Dim y As Double
    Dim z As Double
    Dim mObj As Acad3DFace

    'Open file and read the three points corresponding to one face in a group
    Open filename For Input As #1
    Do While Not EOF(1)

        'First point of face mObj
        Input #1, x, y, z
        pt0(0) = x
        pt0(1) = y
        pt0(2) = z

        'Second point of face mObj
        Input #1, x, y, z
        pt1(0) = x
        pt1(1) = y
        pt1(2) = z


        'Third point of face mObj
        Input #1, x, y, z
        pt2(0) = x
        pt2(1) = y
        pt2(2) = z

        'Create Face
        Set faceObj = ThisDrawing.ModelSpace.Add3DFace(pt0, pt1, pt2, pt2)
        'creating triangular face requires 4th item to equal the third item
    Loop
    'Close input file
    Close #1

End Sub
```

PYTHON SCRIPT TO IMPORT AND PLOT STL FILE OF LUNAR SURFACE TOPOLOGY

```
------------------------
#!/usr/bin/env python
# -*- coding: utf-8 -*-
#
"""
Created on Wed Jun 12 11:14:13 2019

main.py

This script imports and plots a .stl file of the lunar surface topology from
the LROC quickmap website.
The LROC website's exported .stl files contian unneeded surfaces labeling
it's size location etc. This script is able to remove these surfaces.
The .stl files are imported and modified using the numpy-stl library.

References:
# Sample code available:
# https://numpy-stl.readthedocs.io/en/latest/usage.html?highlight=mpl_toolkits
# https://numpy-stl.readthedocs.io/en/latest/usage.html?highlight=x#initial-usage
# info about mesh class:
# https://numpy-stl.readthedocs.io/en/latest/stl.html#stl-mesh
# information about 3d plotting:
# https://jakevdp.github.io/PythonDataScienceHandbook/04.12-three-dimensional-
plotting.html
# Information about contour plotting:
# https://jakevdp.github.io/PythonDataScienceHandbook/04.04-density-and-contour-
plots.html
"""
__author__    = "Lisa Erickson"
__copyright__ = "Copyright © 2018 United States Government"
__email__     = "lisa.erickson@nasa.gov"

# Modules to import
import numpy as np
from stl import mesh
import stl
from mpl_toolkits import mplot3d
from matplotlib import pyplot as plt
import os

# Functions
def import_stl_mesh(inputfile):
    '''
    Generates a surface mesh from a .stl file using numpy-stl library

    Param[in] input_file:       name of .stl file to import
    Param[out] surface_mesh:    surface mesh created from input file
    '''
    inputfile='input/'+inputfile
    print 'Importing mesh from: ', inputfile
    surface_mesh = mesh.Mesh.from_file(inputfile)

    return surface_mesh

def grab_xyz_from_stl(surface_mesh,outputfile):
    '''
    Extracts x y and z points from a surface mesh
    writes these points (removing duplicates) to an output.txt file
    containing xyz data and resturns lists of the xyz data

    Param[in] surface_mesh:      surface mesh created from input file
    Param[out] x:                list of x data
    Param[out] y:                list of y data
    Param[out] z:                list of z data
    '''
    print 'Grabbing xyz points from surface mesh...'
```

```
    # create output file containing x y and z points
    outputfile='output/xyz_points/'+outputfile
    if os.path.exists(outputfile):
        os.remove(outputfile)
    f = open(outputfile, 'w')
    # extract x y z points from the generated mesh
    x_list = []
    y_list = []
    z_list = []

    for p in surface_mesh.points:
        # p contains (x, y, z) (https://numpy-
stl.readthedocs.io/en/latest/usage.html?highlight=x#initial-usage)
        x = p[stl.Dimension.X]
        y = p[stl.Dimension.Y]
        z = p[stl.Dimension.Z]
       # output=str(x)+', '+str(y)+', '+str(z)+'\n'
        x_list.append(x)
        y_list.append(y)
        z_list.append(z)

    # remove repeating points
    x=[]
    y=[]
    z=[]
    x.append(x_list[0])
    y.append(y_list[0])
    z.append(z_list[0])
    xtemp=x[0]
    ytemp=y[0]
    ztemp=z[0]
    output=str(xtemp)+', '+str(ytemp)+', '+str(ztemp)+'\n'
    f.write(output)
    for i in range(1,len(x_list)):
        xtemp = x_list[i]
        ytemp = y_list[i]
        ztemp = z_list[i]
        match = 0
        start=0
        if i>10:
            start=i-10
        for j in range(start,i):
            xcheck=x_list[j]
            ycheck=y_list[j]
            zcheck=z_list[j]
            if xtemp == xcheck and ytemp == ycheck and ztemp == zcheck:
                match = 1
        if match != 1:
           output=str(xtemp)+', '+str(ytemp)+', '+str(ztemp)+'\n'
           x.append(xtemp)
           y.append(ytemp)
           z.append(ztemp)
           f.write(output)

    f.close()
    return x, y, z


def get_max_min_dimensions(x, y, z):
    ''' Outputs max dimensions of stl file given xyz list of points '''
    max_x=max(x)
    max_y=max(y)
    max_z=max(z)

    min_z=min(z)
    return max_x, max_y, max_z, min_z
```

```
def plot_mesh_stl(x, y, z, surface_mesh,outputfile):
    '''
    Creates 3D plot of stl file and saves it as a .png

    Param[in] surface_mesh:     surface mesh created from input file
    Param[in] x:                list of x data
    Param[in] y:                list of y data
    Param[in] z:                list of z data
    Param[in] outputfile:      name of .png file to output
    '''
    print 'Plotting surface mesh...'

    figure = plt.figure()
    ax = mplot3d.Axes3D(figure)
    ax.add_collection3d(mplot3d.art3d.Poly3DCollection(surface_mesh.vectors))

    max_x, max_y, max_z, min_z = get_max_min_dimensions(x, y, z)

    if min_z>0:
        zlimit=0
    else:
        zlimit=min_z

    ax.set_xlim3d(0,max_x)
    ax.set_ylim3d(0,max_y)
    ax.set_zlim3d(zlimit,max_z)

    outputfile='output/plots/'+outputfile
    if os.path.exists(outputfile):
        os.remove(outputfile)
    plt.savefig(outputfile)
    return plt

def cut_extra_points(x,y,z,z_threshold,outputfile) :
    '''
    Removes all xyz points that correspond to the surfaces that label the
    lunar section in the .stl file

    Param[in] x:                list of x data
    Param[in] y:                list of y data
    Param[in] z:                list of z data
    Param[in] z_threshold:      below this value all xyz's are removed
    Param[in] outputfile:       name of .txt file to output
    '''
    print 'Trimming xyz points below z threshold...'
    x_trim=[]
    y_trim=[]
    z_trim=[]

    outputfile='output/xyz_points/'+outputfile
    if os.path.exists(outputfile):
        os.remove(outputfile)
    f = open(outputfile, 'w')
    # remove all points where z <z_threshold

    for i in range(1,len(x)):
        xtemp = x[i]
        ytemp = y[i]
        ztemp = z[i]
        if ztemp>=z_threshold:
            output=str(xtemp)+', '+str(ytemp)+', '+str(ztemp)+'\n'
            x_trim.append(xtemp)
            y_trim.append(ytemp)
            z_trim.append(ztemp)
            f.write(output)
    f.close()
    return x_trim, y_trim, z_trim

def plot_xyz_scatter(x,y,z,outputfile):
```

```
    ''' Creates 3D scatter plot with x y and z points from the .stl file'''
    print 'Plotting xyz points from surface mesh...'
    ax = plt.axes(projection='3d')
    ax.scatter3D(x,y,z,marker='.',alpha=0.1)

    outputfile='output/plots/'+outputfile
    if os.path.exists(outputfile):
        os.remove(outputfile)
    plt.savefig(outputfile)
    return

def cut_extra_vectors(s_mesh,z_threshold,newstlfilename):
    '''
    Recreates a surface mesh and .stl file with all the faces that label the
    lunar section removed

    Param[in] s_mesh            origional surface mesh
    Param[in] z_threshold:      below this value all xyz's are removed
    Param[in] outputfile:       name of .txt file to output
    Param[out] new_surf:        name of new .stl file created
    '''
    # Number of vectors
    print 'Number of surface mesh vectors', len(s_mesh.vectors)

    count=0
    idx_passed_threshold=[]
    idx_good=[]
    # count number of vectors with z below threshold
    for i in range(0,len(s_mesh.vectors)):
        threshold_exceeded=0
        for j in range(0,len(s_mesh.vectors[0])):
            # check and mark if any of the elements in vector j have a z value
            # below the threshold
            if s_mesh.vectors[i][j][2]<z_threshold:
                threshold_exceeded=1
        # mark if the vector had any z element below the threshold
        # build list of indicies marking which elements were below threshold
        if threshold_exceeded==1:
            count+=1
            idx_passed_threshold.append(i)
        else:
            idx_good.append(i)
    print 'Number of vectors failed z threshold', count
    print 'Number of good vectors', len(idx_good)
    # Create new mesh
    num_vectors=len(s_mesh.vectors)-count
    # initialize data vectors
    data = np.zeros(num_vectors, dtype=mesh.Mesh.dtype)
    # fill in vectors
    k=0
    for i in range(0,len(idx_good)):
        index_to_copy=idx_good[i]
        np.copyto(data['vectors'][k],s_mesh.vectors[index_to_copy])
        k+=1
    print 'Regenerate mesh with only good vectors...'
    new_surf= mesh.Mesh(data)

    newstlfilename='output/stl/'+newstlfilename
    if os.path.exists(newstlfilename):
        os.remove(newstlfilename)
    print 'Remakeing .stl file  ...'
    new_surf.save(newstlfilename)

    return new_surf

def grab_xyz_of_vectors(s_mesh,outputfile):
    '''
    Recreates a surface mesh and .stl file with all the faces that label the
    lunar section removed
```

```
    Param[in] s_mesh            surface mesh
    Param[in] outputfile:       name of .txt file to output
    '''
    print 'Outputting x y z for each point defining surface mesh vectors...'

    outputfile='output/vectors/'+outputfile
    if os.path.exists(outputfile):
        os.remove(outputfile)
    f = open(outputfile, 'w')

    # Iterate through vectors of .stl file
    for i in range(0,len(s_mesh.vectors)):
        # Iterate through 3 points of a vector
        for j in range(0,len(s_mesh.vectors[0])):
            # Iterate through x y z of each point
            outstr=''                                   # initialize output string
            for k in range (0,len(s_mesh.vectors[0][0])):
                outstr=outstr+str(s_mesh.vectors[i][j][k])
                if k<(len(s_mesh.vectors[0][0])-1):
                    outstr=outstr+' '
                else:
                    outstr=outstr +'\n'
            # Write to output file
            f.write(outstr)

    f.close()
    return

def process_stl(input_file,z_threshold):

    # Import .stl file
    surface_mesh = import_stl_mesh(input_file)

    # Extract x y z points from .stl file
    outputfile='lunar_surface_points.txt'
    x, y, z = grab_xyz_from_stl(surface_mesh,outputfile)

    # Plot .stl file
    outputfile='lunar_surface.png'
    plot = plot_mesh_stl(x, y, z, surface_mesh,outputfile)

    # Remove extra points from .xtl file used to label lunar section
    outputfile='lunar_surface_points_trimmed.txt'
    xtrimmed, ytrimmed, ztrimmed = cut_extra_points(x,y,z,z_threshold,outputfile)

    # Plot updated xyz list
    outputfile='new_scatter.png'
    plot_xyz_scatter(xtrimmed,ytrimmed,ztrimmed,outputfile)

    # Remove extra surfaces used to label lunar section
    newstlfilename='new_surf.stl'
    new_surf = cut_extra_vectors(surface_mesh,z_threshold,newstlfilename)

    # Extract x y z points from .stl file
    outputfile='lunar_surface_points_cut.txt'
    xcut, ycut, zcut = grab_xyz_from_stl(new_surf,outputfile)

    # Plot .stl file
    outputfile='new_lunar_surface.png'
    new_plot = plot_mesh_stl(xcut,ycut,zcut,new_surf,outputfile)

    # Uncomment if want to show plot
    #new_plot.show()
    return

def generate_xyz_for_autocad_import(inputfile):

    # Import .stl file
```

```
    surface_mesh = import_stl_mesh(inputfile)

    # Access and output mesh vectors
    outputfile='vector_points.txt'
    grab_xyz_of_vectors(surface_mesh,outputfile)


    # Extract x y z points from .stl file
    outputfile='lunar_surface_points_cut.txt'
    x, y, z = grab_xyz_from_stl(surface_mesh,outputfile)

    # Plot .stl file
    outputfile='meshlab_lunar_surface.png'
    new_plot = plot_mesh_stl(x,y,z,surface_mesh,outputfile)
    new_plot.show()

    return


if __name__ == '__main__': # run if called from command line

    # Process stl from LROC quickmap website
    # Step 1
    val = input("Perform Step 1, trim .stl (1=yes, 0=no)?: ")
    if val==1:
        # Select input file:
        input_file_name = input("Input file name as string (e.g. 'qm3d_1x1_1x.stl'):
")
        minimum_elevation = input("Input minimum desired elevation in meters (e.g.
1057 or -2168): ")
        process_stl(input_file_name,minimum_elevation)
        # Inputs for example files:
        #input_file_name=qm3d_1x1_1x_b_large.stl
        #minimum_elevation=1057#-2168
        exit()

    # Step 2
    # Generate vectors from .stl outputed from MeshLAB
    val = input("Perform Step 2, generate xzy for mesh vectors .stl (1=yes, 0=no)?: ")
    if val==1:
        # Select input file:
        input_file_name = input("Input file name as string (e.g.
'new_cut_surface.stl'): ")
        generate_xyz_for_autocad_import(input_file_name)
        # Inputs for example files:
        # input_file_name='new_surf_cut_more_in_python_first_reduce5.stl'
```

APPENDIX G
LIGHT SCATTERING OF LUNAR REGOLITH

Solar radiation incident upon lunar regolith may be characterized as a bi-directional reflection with the incident, emission and azimuthal angles noted in Figure G-1. The solar phase angle is the angle between the incident and reflected ray and may be determined from the expression below.

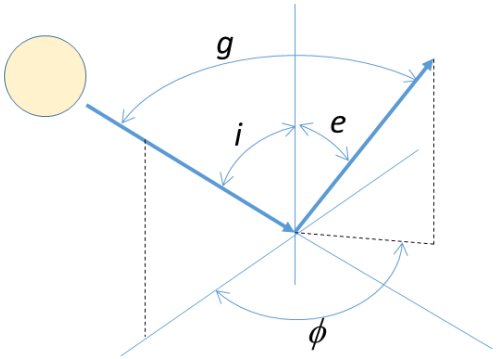

g	phase angle
i	incident angle
e	emission angle
ϕ	azimuth angle

FIGURE G-1: BIDIRECTIONAL REFLECTANCE

$$cos(g) = \cos(e)\cos(i) + \sin(e)\sin(i)\cos(\emptyset)$$

Hapke (1981) defined spectral radiance as a function of the solar phase angle and the incident/emission angles. Special functions were included to account for the phase angle, back scattering and multiple scattering as shown in Figure G-2.

$$I(i,e,g) = J\frac{w}{4\pi}\frac{\cos(i)}{\cos(i)+\cos(e)}\left(\underbrace{[1+B(g)]p(g)}_{Singularly\ Scattered} + \underbrace{H(\cos(i))H(\cos(e))-1}_{Multiply\ Scattered}\right)$$

$$H(\mu) = \frac{1+2\mu}{1+2\mu\sqrt{1-w}}$$

J	solar constant
w	single particle scattering albedo
B	back scattering function
p	phase function

FIGURE G-2: SPECTRAL RADIANCE

Sato, et al (2013) fitted parameter maps of the Moon based upon LRO data using the Henyey-Greenstein double-lobed single particle phase function and a modified back scatter function (Shadow Hiding Opposition Effect [SHOE]) introduced into Hapke's original equation as shown in Figure G-3. The parameters highlighted in red are mapped to LRO data.

$$I(i,e,g,w,b,c) = J\frac{w}{4\pi}\frac{\cos(i)}{\cos(i)+\cos(e)}([1+B_{so}B_s(g)]p(g,b,c)+H(\cos(i))H(\cos(e))-1)$$

$$p(g,b,c) = \frac{1+c}{2}\frac{1-b^2}{(1-2bcos(g)+b^2)^{\frac{3}{2}}}+\frac{1-c}{2}\frac{1-b^2}{(1+2bcos(g)+b^2)^{\frac{3}{2}}} \qquad B_s(g) = \frac{1}{1+\frac{tan\frac{g}{2}}{h_s}}$$

FIGURE G-3: HAPKE/SATO EQUATIONS

Sato, et al (2013) resolved parameter maps of the lunar surface between latitudes 70ºS and 70ºN for Hapke parameters w, b, c, B_{so} and h_s. The DSNE contains recommended values for phase function arguments b and c versus location where c controls back scatter (see "hockey stick" plot in Figure G-4). It may be possible to develop directional hemispherical albedo profiles for any spot on the lunar surface using the parameter maps in Figure G-5.

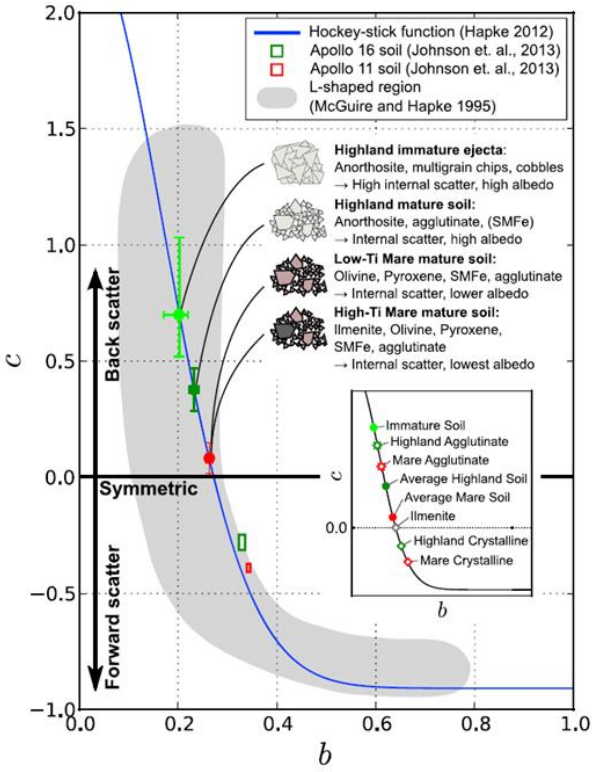

FIGURE G-4: PHASE FUNCTION PARAMETERS

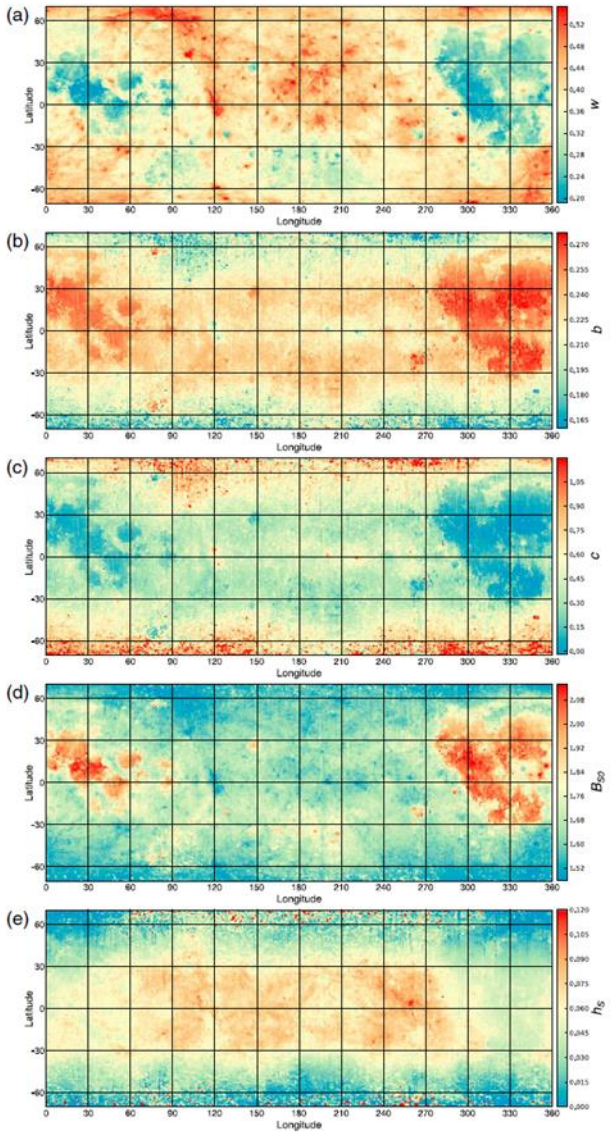

FIGURE G-5: HAPKE PARAMETER MAPS OF THE MOON

Computed lunar reflectance using the Hapke/Sato model is shown in Figure G-6 for different incidence angles. Notice the sharp return in the direction of incidence.

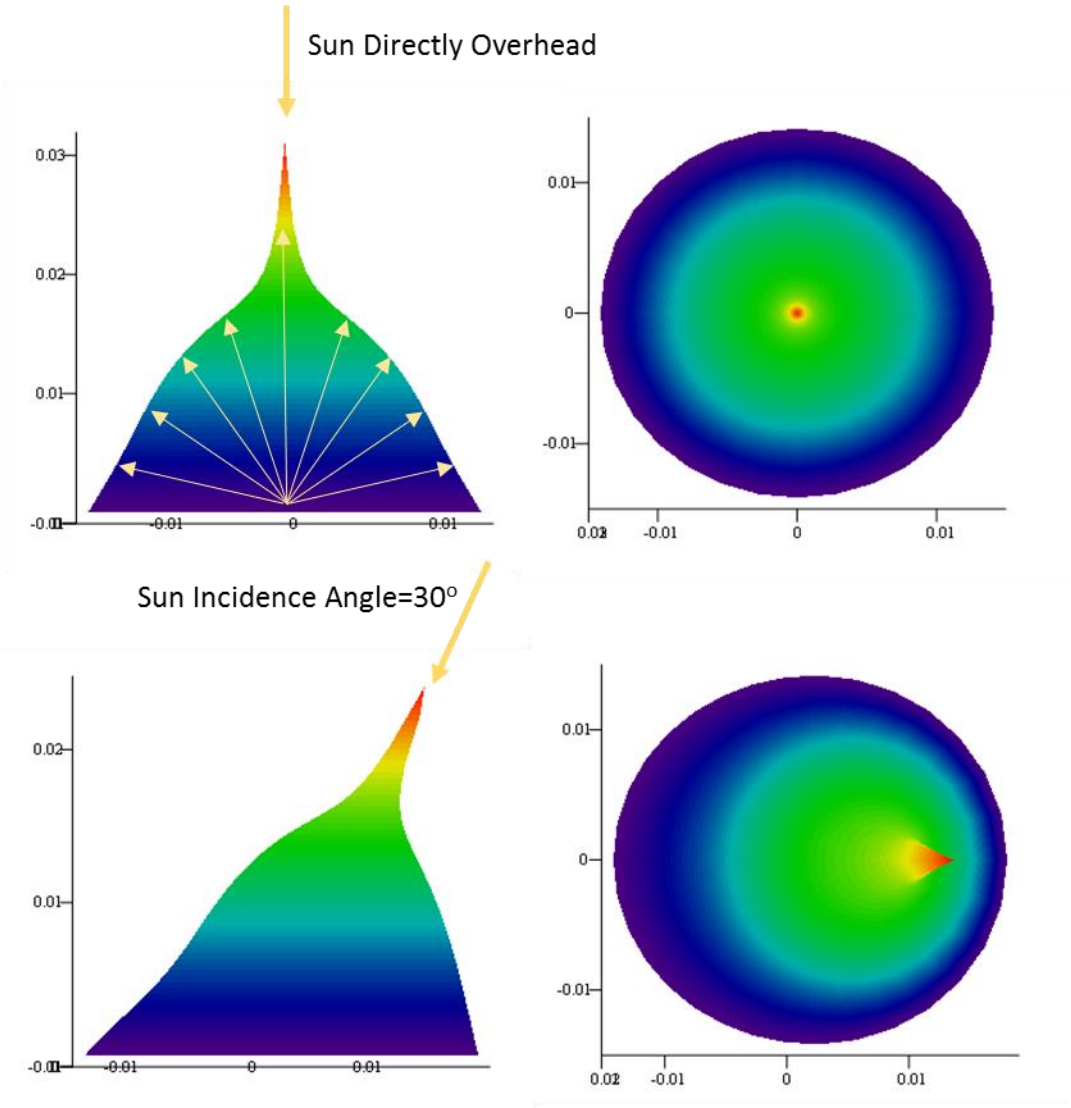

FIGURE G-6: DIRECTIONAL ALBEDO

It is possible to integrate the directional reflectance versus incidence angle to obtain a directional hemispherical albedo for the lunar surface as shown in Figure G-7. At extreme incidence angles (> 60°), the results don't agree well with previously provided empirical or derived results although the trend is similar. Two caveats are that Sato, et al (2013) didn't map the Hapke parameters above 70° latitude (North or South) and the results are only presented at a single wavelength.

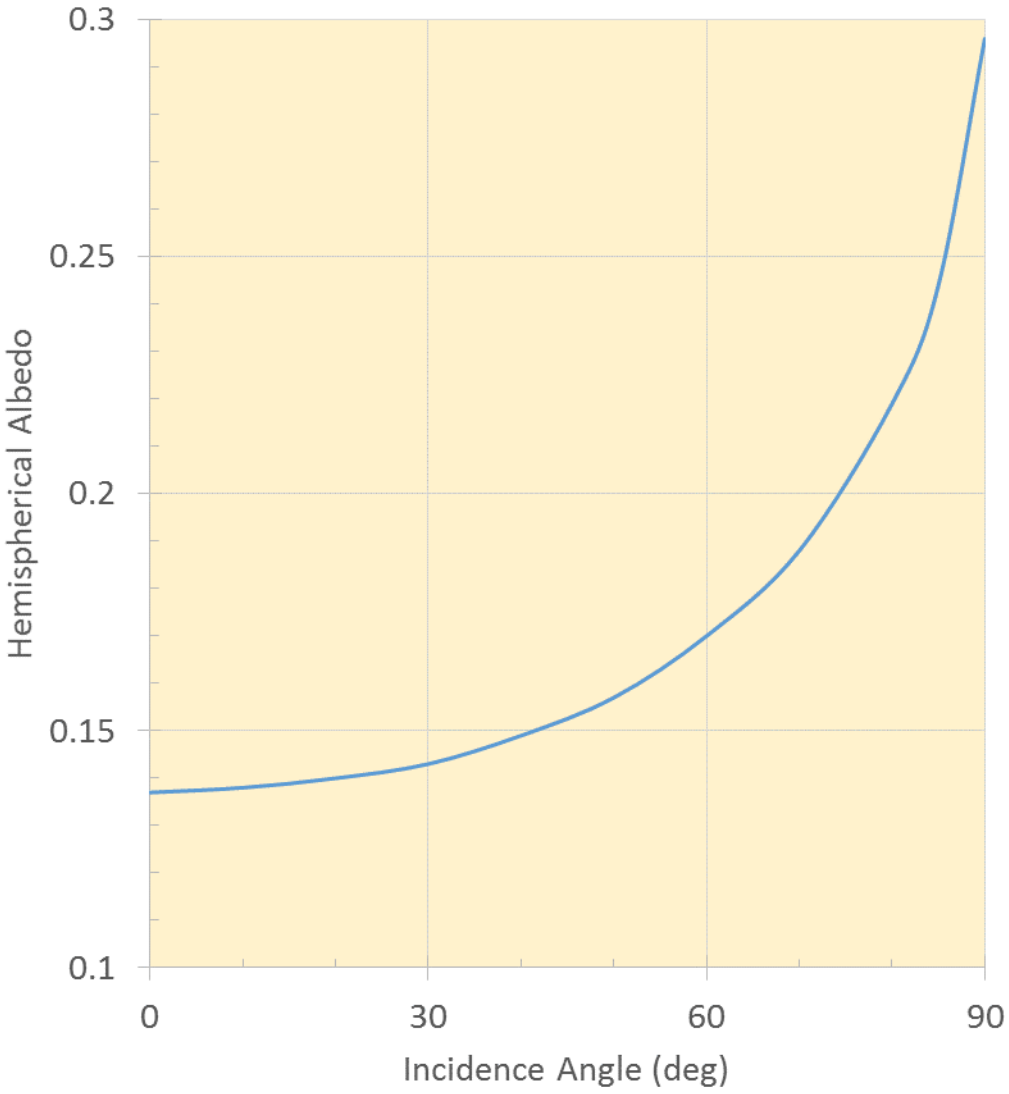

FIGURE G-7: DIRECTIONAL HEMISPHERICAL ALBEDO